

Non-invasive quantitative imaging of brain perfusion in hypocapnia by ASL MRI

Gonçalo Filipe Almeida Gomes

Thesis to obtain the Master of Science Degree in

Biomedical Engineering

Supervisors:

Prof. Patrícia Margarida Piedade Figueiredo

Pedro Ferro Vilela M.D.

Examination Committee:

Chairperson: Prof. João Pedro Estrela Rodrigues Conde

Supervisor: Prof. Patrícia Margarida Piedade Figueiredo

Members of the committee: Prof. João Miguel Raposo Sanches

October 2015

Acknowledgements

I would like to thank Prof. Patrícia Figueiredo for the opportunity of developing my master's thesis in an area so captivating and for her guidance and important feedback that improved the quality of this work. I would also like to thank all the people involved in the NeuroPhysim project that acquired and provided the data for this work and enabled me to use it.

To all my colleagues from rooms 6.13 and 6.14 who helped me with anything I needed.

A special thanks to Joana Pinto for all the shared knowledge, for the constant availability she showed during the entire work and for the algorithms that she kindly provided.

To all my friends who always supported me and made my life happier.

Finally I would like to thank my family for always being there and constantly encouraging me during the tough times, for giving me the opportunity to make my own choices and for all the unconditional support during my entire life.

Abstract

Arterial Spin Labelling (ASL) is a Magnetic Resonance imaging (MRI) technique developed for the non-invasive, quantitative mapping of brain perfusion. In this work, the main goal was to optimize a kinetic modelling approach for quantitatively mapping brain perfusion using multiple post-labelling delay (PLD) ASL MRI acquisitions, during baseline and hypocapnia conditions.

Multiple-PLD ASL data were collected on a 3T MRI system from twelve healthy volunteers. A pipeline for the analysis of the data was developed, including a number of pre-processing steps, followed by fitting of a General Kinetic Model for the estimation of CBF, BAT and aBV. Pre-processing included: motion correction and co-registration of the ASL images. Through the use of a saturation-recovery curve that was fitted to the control image it was possible to obtain a blood M_0 calibration value that was extracted from the estimated M_0 in CSF. For the model fitting, a Bayesian approach was employed.

A statistical analysis was then performed to test for differences in the perfusion parameters between baseline and hypocapnia. The results showed a significant decrease in the grey matter mean value of CBF and the vascular mean value of aBV and a significant increase in the grey matter mean value of BAT, from baseline to hypocapnia, which is in agreement with the literature.

In conclusion, the data analysis pipeline and kinetic modelling approach developed in this work were adequate. The use of ASL MRI to study perfusion changes in hypocapnia is very scarce in the literature, hence the importance of this study.

Keywords: Magnetic Resonance Imaging, Arterial Spin Labelling, Paced Deep Breathing, Brain Perfusion, Cerebral Blood Flow, Hypocapnia.

Resumo

Arterial Spin Labelling (ASL) é uma técnica de Ressonância Magnética a ser utilizada na investigação da quantificação da perfusão cerebral. Neste trabalho, o principal objetivo foi desenvolver um modelo cinético para mapear a perfusão cerebral usando, quantitativamente, aquisições *multiple post-labelling delay* (PLD) ASL MRI durante o descanso e hipocapnia.

Dados de *multiple*-PLD ASL foram adquiridos num sistema de MRI 3T a doze voluntários saudáveis. A análise dos dados foi desenvolvida segundo uma diretriz, que inclui o pré-processamento, seguido do modelo de cinética geral para a estimativa do CBF, BAT e aBV. O pré-processamento inclui: correção do movimento e co-registro das imagens. Através da utilização de uma curva de *saturation-recovery* que foi utilizada nas imagens controlo, foi possível obter um valor de M_0 sanguíneo, que foi extraído através do M_0 estimado em CSF. Para o modelo cinético foi usado uma abordagem bayesiana.

A análise estatística foi realizada para testar diferenças nos parâmetros de perfusão entre as condições de descanso e hipocapnia. Os resultados mostraram uma diminuição significativa nos valores de CBF na massa cinzenta e aBV vascular e um aumento significativo no valor de BAT na massa cinzenta, da condição de descanso para hipocapnia, o que está de acordo com a literatura.

Para concluir, o modelo cinético desenvolvido permitiu uma estimativa quantitativa adequada da perfusão cerebral. A utilização dos dados de ASL MRI para esta estimativa em hipocapnia é muito escassa na literatura, daí a importância deste estudo.

Palavras-chave: Ressonância Magnética, *Arterial Spin Labelling*, Tarefa de Respiração Profunda, Perfusion Cerebral, Fluxo Sanguíneo Cerebral, Hipocapnia.

Contents

Acknowledgements.....	ii
Abstract	iv
Resumo	vi
Contents.....	viii
List of Figures	xi
List of Tables	xiv
List of abbreviations.....	xv
1 Introduction	18
1.1 <i>Motivation</i>	18
1.2 <i>Physiological principles</i>	19
1.2.1 Brain perfusion parameters	19
1.2.2 Vasoactive behaviour (cerebrovascular reactivity).....	20
1.2.3 Measurement techniques	22
1.3 <i>ASL MRI perfusion imaging principles</i>	23
1.3.1 MRI basic principles.....	23
1.3.2 Arterial Spin Labelling MRI	25
1.3.2.1 Basic principles	25
1.3.2.2 Acquisition techniques	27
1.3.2.3 General kinetic model	29
1.3.2.4 Parameter estimation (Bayesian Inference).....	31
1.4 <i>State-of-the-art</i>	32
1.4.1 CBF assessment in baseline and hypoxia conditions.....	33
1.5 <i>Thesis aims and outline</i>	34

2 Materials & Methods	35
2.1 <i>Data acquisition</i>	35
2.1.1 Subjects and tasks	35
2.1.2 Imaging.....	35
2.1.3 $P_{ET}CO_2$ recording.....	36
2.2 <i>Data analysis.....</i>	37
2.2.1 Pre-processing.....	37
2.2.1.1 Preliminary corrections	37
2.2.1.2 Image registration	39
2.2.1.3 Tag-control differencing.....	40
2.2.1.4 Off-resonance correction	41
2.2.1.5 Calibration	42
2.2.2 Parameter estimation	44
2.2.2.1 Parameter priors	44
2.2.2.2 Model fitting.....	45
2.2.3 Definition of regions of interest	47
2.3 <i>Baseline vs hypocapnia comparison.....</i>	48
3 Results and Discussion	50
3.1 <i>End-tidal carbon dioxide pressure</i>	50
3.2 <i>Head movement.....</i>	53
3.3 <i>Parameters' prior distribution</i>	54
3.3.1 BAT prior	54
3.3.2 <i>Spatial prior.....</i>	57
3.4 <i>Baseline vs hypocapnia</i>	58
3.4.1 Number of bad fitting voxels.....	59
3.4.2 Parameter values and group analysis	61

3.4.2.1	Grey matter ROI mask	62
3.4.2.2	Tissue and vascular ROI masks	67
3.4.2.3	MNI Atlas ROIs.....	71
3.4.2.4	Voxelwise whole-brain comparison	73
3.4.3	Correlation with $P_{ET}CO_2$	77
4 Conclusions	80
5 References	82
Appendices	89

List of Figures

Figure 1.1 – Cerebrovascular auto-regulation and the effect of blood gases on CBF. A decrease the in arterial partial pressure of CO ₂ (PaCO ₂) induces a decrease in CBF. Adapted from Bor-Seng-Shu et al. (2012).....	21
Figure 1.2 - Behaviour of a sample when placed in a strong magnetic field; a) When no magnetic field is applied, the magnetic moments are randomly oriented, yielding zero net magnetization; b) Gradually the moments align either with the field or against it; c) An oscillating magnetic field B_1 changes the orientation of the nuclear moments until there is a measurable magnetization in the transversal xy plane; (d) During the application of RF pulse, where there is transversal magnetization. Adapted from Jezzard et al. (2001).....	24
Figure 1.3 – Acquisition scheme of tag and control images.....	26
Figure 1.4 – Longitudinal relaxation of magnetization. Adapted from Liu & Brown (2007).	26
Figure 1.5 – Scheme for imaging and labelling regions for CASL, PCASL and PASL. Adapted from Alsop et al. (2014).....	28
Figure 1.6 – Pulse sequence for Q2TIPS. Double in-plane pre-saturation pulse followed by sech inversion labelling pulses. The grey gradient is for alternately applying tag and control images. Periodic pulses from $TI1$ to $TI1S$ consist of a train of excitation pulses. EPI image acquisition at $TI2$. Adapted from Luh et al. (1999).....	29
Figure 1.7 – Theoretical pulsed ASL signal curves of the tissue and macro-vascular components as well as the total ASL signal curve.	31
Figure 2.1 – Basic unit of PDB period. Both “inspire” and “expire” are repeated 8 times, leaving 40 s of the PDB interval.	35
Figure 2.2 - Example of a subject’s structural (LEFT) and BOLD (RIGHT) images: (left to right: sagittal, coronal and axial) before (top) and after (bottom) brain extraction using BET.....	38
Figure 2.3 - Motion correction results for one example subject. The x axis represents the number of imaging volumes (TR=2.5s).....	39
Figure 2.4 – Image registration example.	40
Figure 2.5 – Example of the image registrations done with the additional BOLD image step.	40
Figure 2.6 – Tag-control differencing example. The Diffdata image corresponds to the tag-control differenced data.....	41
Figure 2.7 – An example of M_{0t} (left) and M_{0a} estimated in a mask of CSF (right).	43

Figure 2.8 – Example of CBF (left), BAT (middle) and aBV (right) maps for a representative subject.....	45
Figure 2.9 – Main effect of the spatial prior in a CBF image.....	46
Figure 2.10 – Example of the MNI structural atlas. The different colours represent the 9 regions (left to right: sagittal, coronal and axial).	47
Figure 3.1 – $P_{ET}CO_2$ time courses for the subjects S1, S2, S3 and S4.....	50
Figure 3.2 – $P_{ET}CO_2$ time courses for the subjects S5, S10, S11 and S12.	51
Figure 3.3 – $P_{ET}CO_2$ values bar charts for the subjects that performed hypocapnia and the mean value. Error bars represent the standard deviation of the mean and * denotes significant differences ($p<0.05$).	52
Figure 3.4 – Mean displacement in mm bar charts for the subjects analysed, with absolute values (left) and relative values (right). Error bars represent the standard deviation of the mean.....	53
Figure 3.5 – The mean displacement time courses for subjects S4, S5, S8 and S9, in the respective problematic condition.	54
Figure 3.6 – Bar charts for CBF (top), BAT (middle) and aBV (bottom) values for each combination of BAT prior. Error bars represent the standard deviation of the mean values.....	55
Figure 3.7 – Example slice of the estimated parameters' maps for subject S2 with BAT prior mean equal to 0.7 s and for each <i>batsd</i>.....	56
Figure 3.8 – Number of bad fitting voxels averaged for all subjects in each combination of BAT prior.	56
Figure 3.9 – Bar charts for CBF (top), BAT (middle) and aBV (bottom) estimated in all subjects, with and without the <i>spatial</i> prior, also with subjects' mean. Error bars represent the standard deviation of the mean values.	57
Figure 3.10 – CBF, BAT and aBV maps for subject S2 with and without <i>spatial</i> prior.....	58
Figure 3.11 – Bar charts of number of bad fitting voxels for all subjects in REST and PDB, with and without the <i>spatial</i> prior, and the subjects' mean values. Error bars represent the standard deviation of the mean values.	59
Figure 3.12 – CBF, BAT and aBV maps for subjects S2, in whole brain.	61
Figure 3.13 – Bar charts of CBF (top), BAT (middle) and aBV (bottom) maps for all subjects and in REST and PDB, using GM ROI mask. Error bars represent the standard deviation of the mean values and * denotes significant differences ($p<0.05$).	63
Figure 3.14 – CBF, BAT and aBV maps for subjects S2, in GM ROI mask.	65

Figure 3.15 – Bar charts of CBF, BAT and aBV maps for all subjects and in REST and PDB, using Tissue and Vascular ROI masks. Error bars represent the standard deviation of the mean values and * denotes significant differences ($p<0.05$)	68
Figure 3.16 – CBF, BAT and aBV maps for subjects S2, in Tissue and Vascular ROI masks.	70
Figure 3.17 – Bar charts of mean values obtained for each anatomical region in both REST and PDB, after averaging all subjects in each region and condition. Error bars represent the standard deviation of the mean values and * denotes significant differences ($p<0.05$)	72
Figure 3.18 – CBF uncorrected results using TFCE. (Top) CBF with GM ROI mask and (bottom) with Tissue ROI mask.	74
Figure 3.19 – aBV uncorrected results using TFCE. (Top) aBV with GM ROI mask and (bottom) with Vascular ROI mask.	75
Figure 3.20 – CBF uncorrected results using Voxel-wise. (Top) CBF with GM ROI mask and (bottom) with Tissue ROI mask.	76
Figure 3.21 – aBV uncorrected results using Voxel-wise. (Top) aBV with GM ROI mask and (bottom) with Vascular ROI mask.	77
Figure 3.22 – Correlation results for CBF, BAT and aBV with GM ROI mask.	78
Figure 3.23 – Correlation results for CBF, BAT and aBV with Tissue and Vascular ROI mask.	79

List of Tables

Table 2.1 – Prior distribution mean and standard deviation values for the parameters of the General Kinetic Model.....	44
Table 3.1 – $P_{ET}CO_2$ values in mmHg acquired in REST and PDB conditions, for every subject, also with the difference values. * denotes significant differences ($p<0.05$)	51
Table 3.2 – Number of bad fitting voxels for all subjects with and without the spatial prior and in REST and PDB condition. The difference value (PDB – REST) is also depicted.	59
Table 3.3 – Parameters' maps mean values obtained for every subject in both REST and PDB, using GM ROI mask. The subjects mean for each parameter is also present.....	62
Table 3.4 – Parameters' maps mean values obtained for every subject in both REST and PDB using Tissue and Vascular ROI masks. The subjects mean for each parameter is also present.....	67
Table 3.5 – Correlation coefficients and p-values for each parameter and in both GM mask and Tissue/Vascular masks.	78

List of abbreviations

aBV	Arterial Blood Volume
ARD	Automatic Relevance Determination
ASL	Arterial Spin Labelling
BASIL	Bayesian Inference for Arterial Spin Labelling MRI
BAT	Bolus Arrival Time
BET	Brain Extraction Tool
BH	Breath Hold
BOLD	Blood Oxygenation Level Dependent
CASL	Continuous Arterial Spin Labelling
CBF	Cerebral Blood Flow
CBV	Cerebral Blood Volume
CPP	Cerebral Perfusion Pressure
CSF	Cerebrospinal Fluid
CVR	Cerebrovascular Reactivity
CVRe	Cerebrovascular Resistance
EPI	Echo-Planar Imaging
FAST	FMRIB's Automated Segmentation Tool
fMRI	Functional Magnetic Resonance Imaging
GLM	General Linear Model
GM	Grey Matter
MCA	Middle Cerebral Artery
MNI	Montreal Neurological Institute
MPRAGE	Magnetization-Prepared Rapid Acquisition with Gradient Echo
MRI	Magnetic Resonance Imaging
PASL	Pulsed Arterial Spin Labelling
PCASL	Pseudo-Continuous Arterial Spin Labelling
PDF	Probability Density Function
PET	Positron Emission Tomography
P_{ET}CO₂	End-Tidal CO ₂ pressure
PLD	Post-Labelling Delay
ROI	Region of Interest
SD	Standard Deviation
SNR	Signal-to-Noise Ratio
SPECT	Single Photon Emission Tomography
TCID	Transcerebral Double-Indicator Dilution

TDU	Transcranial Doppler Ultrasound
TE	Echo-Time
TFCE	Threshold-Free Cluster Enhancement
TI	Inversion Time
WM	White Matter
Xe-CT	Xenon Computed Tomography

1 Introduction

This work addresses the comparison of the brain perfusion as characterized by the cerebral blood flow (CBF), bolus arrival time (BAT) and arterial blood volume (aBV) responses to two different conditions, baseline and hypocapnia, using Arterial Spin Labelling Magnetic Resonance Imaging (ASL MRI). A General Kinetic Model approach is used, which applies Bayesian Inference to estimate the parameters. The values of the parameters of both conditions are then compared.

This section presents a brief contextualization of the problem addressed in this work. It consists of explaining the motivation, introducing the physiological principles related to the parameters of interest and the techniques used to assess them. Then, essential concepts about the basic principles of Magnetic Resonance Imaging (MRI) are introduced with a focus on the Arterial Spin Labelling (ASL) technique, followed by the state of the art and the thesis aims and outline.

1.1 Motivation

The brain is a crucial organ of the human body. Therefore, everything related to it is also important and worth studying. Brain perfusion, or CBF, is the process of delivering blood to the capillary beds and, from these, nutrients to the brain tissues, and it is always adjusting to the necessities of brain function and metabolism. Too much brain perfusion could cause an accumulation of blood (hyperemia) that would result in brain tissue damage. Less blood flow could cause ischemia, which could lead to tissue death. Furthermore, brain perfusion is also responsible for draining waste products from the tissue cells, like CO₂ and other metabolites. Hence, very important diagnostic information on status and functionality of brain tissues could be extracted from brain perfusion, allowing medical professionals to control patients with cerebral edema, traumatic brain injuries or stroke through the analysis of CBF (Haddad & Arabi, 2012; Kelly et al., 1997; Rubin et al., 2000).

Thus, given the importance of brain perfusion, it became clear that research of this brain characteristic was necessary and could be a great help for medical professionals. Cognitive tasks were developed to induce brain stimulation so that variations in CBF could be studied. These variations could be caused by neurotransmitter release (Attwell & Iadecola, 2002), changes in oxygen at local levels or by manipulating the vascular reactivity through pharmacological drugs or respiratory tasks (Ho et al., 2011). However, brain perfusion is a complex phenomenon, since there are several disparities on the vascular responses between and within subjects, like variability in oxidative demand and vascular tone (Hutchinson et al., 2006; Leontiev & Buxton, 2007).

So, in order to control and study the variations of brain perfusion to different stimuli, imaging techniques had to be devised to assess them, particularly Arterial Spin Labelling (ASL) Magnetic Resonance Imaging.

1.2 Physiological principles

The following sections describe the brain perfusion parameters, the behaviour of vasoactive blood vessels and the techniques used to assess them.

1.2.1 Brain perfusion parameters

In physiology, perfusion means the process of delivery of oxygen and nutrients to organs, tissues or a capillary bed through arterial blood vessels flow to ensure the proper function. Therefore, it is a very important feature since it provides information on status and functionality of organs and tissue (Günther, 2013).

Brain perfusion is also known as CBF and is usually measured in units of millilitres of blood per 100 grams of tissue per minute (ml/100g/min) (Buxton, 2002; Tofts, 2003). The CBF varies plenty within the human brain, depending on the type of tissue, where the average value of the grey matter is three times higher than white matter (Ito et al., 2004; Rostrup et al., 2005). However, it is established that the typical average value of CBF in the human brain is around 50-60 ml/100g/min (Buxton et al., 1998; Buxton, 2005).

CBF is directly dependent on the cerebral perfusion pressure (CPP), which is the difference between mean arterial and intracranial pressures, and is inversely dependent to the cerebrovascular resistance (CVRe) (Equation 1.1) (AnaesthesiaUK., 2007; Pinto, 2012).

$$CBF = \frac{CPP}{CVRe} \quad (1.1)$$

Another physiological parameter relevant for the understanding of this work is the cerebrovascular reactivity (CVR), which is the intrinsic auto-regulatory capacity of the brain to modify its vasculature to compensate for systemic perturbations, in order to keep the supply of oxygen and nutrients to the tissues at a constant level (Pinto, 2012). These auto-regulatory changes have two main mechanisms, vasoconstriction and vasodilatation. The first one is the increase of cerebrovascular resistance, when the CPP is increased. The latter is the decrease of cerebrovascular resistance, when the CPP is reduced (Cipolla, 2009). So, essentially, CVR corresponds to the CBF auto-regulation, which is typically in the form of mean blood pressures of the order of 60 to 150 mmHg (Paulson et al., 1990). Although, these limits are not fixed and blood pressures may produce changes beyond them.

The natural assumption arising from this CBF auto-regulation is that in cases of disease where the CVR is impaired, the auto-regulation is also impaired. Therefore, CVR is a very important diagnosis tool to assess if someone has a higher risk of having a stroke and would gain in doing an artery bypass or stenting (King et al., 2011).

1.2.2 Vasoactive behaviour (cerebrovascular reactivity)

One way to assess the CVR is to experimentally/externally induce vasodilatation or vasoconstriction, which in turn will increase or decrease CBF, respectively. This CBF change should be measurable in a reproducible way when using an appropriate imaging method (Pinto, 2012).

Most studies employ carbon dioxide (CO_2) inhalation to induce hypercapnia, to which follows vasodilation, combined with an appropriate technique to measure the resulting increases in CBF. However, inducing vasoconstriction may be important since there are conditions where further vasodilation is not possible, like in chronic stroke patients (Zhao et al., 2009). To induce global cerebral vasoconstriction it is necessary to either inject an intravenous vasoconstrictor drug, such as Vasopressin (Henderson & Byron, 2007), to administrate oxygen. Alternatively, hypocapnia can also be induced non-invasively through hyperventilation. In order to minimize head motion associated with uncontrolled hyperventilation, mild hypocapnia can be achieved through the performance of paced deep breathing tasks (Bright et al., 2009; Sousa et al., 2014).

The drug Vasopressin is a nine-amino acid peptide hormone that is present in the posterior pituitary gland. The increase of plasma osmolarity or reduction in blood pressure induces a release of Vasopressin into the systemic circulation. This release causes the Vasopressin to bind to a specific receptor (V_{1a} receptors) on vascular smooth muscles cells that induces vasoconstriction (Henderson & Byron, 2007). In spite of Vasopressin being a more robust method than hypocapnia methods for inducing vasoconstriction, in these types of studies the drug itself is not widely available, hence the use of hypocapnia methods.

Hypocapnia is the decrease in arterial CO_2 partial pressure (PaCO_2) achieved by hyperventilation. With hyperventilation, the alveolar CO_2 concentration reduces which causes a decrease of the intravascular PaCO_2 and results in the increase of the perivascular and intra-neuronal pH, which causes vasoconstriction and, therefore, CBF reduction (Posse et al., 1997). Hyperventilation also results in a mild increase in the oxygen arterial partial pressure (PaO_2), since the transport of oxygen to the lungs and arterial blood will be bigger (Bor-Seng-Shu et al., 2012). The relationships between CBF and PaCO_2 are depicted in Figure 1.1, with the behaviour previously shown.

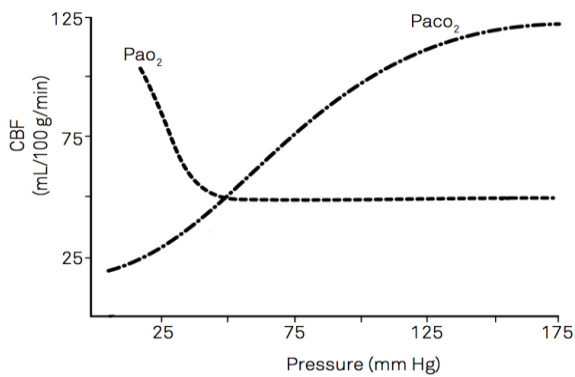


Figure 1.1 – Cerebrovascular auto-regulation and the effect of blood gases on CBF. A decrease in arterial partial pressure of CO₂ (PaCO₂) induces a decrease in CBF. Adapted from Bor-Seng-Shu et al. (2012).

Paced deep breathing is a recent method developed to induce a mild hypocapnia and consequently vasoconstriction. It consists of intervals of self-paced breathing alternated with intervals of paced deep breathing. In the self-paced breathing the subjects breathe normally at their own pace and in the paced deep breathing they are asked to breathe more deeply following timed cues for inspiration and expiration, which may be visual or auditory (Sousa et al., 2014). This cycle is repeated several times depending on the type of study. With this task, the PaCO₂ will decrease, during paced deep breathing, which leads to hypocapnia and consequently CBF decrease.

When comparing what is the better way to induce vasoconstriction it is important to take into account that paced deep breathing is a simple and completely non-invasive approach that does not require a source of CO₂ or O₂. The elderly subjects or subjects with certain diseases like pulmonary diseases may not support this inhalation of CO₂ or O₂. However, when using the paced deep breathing task it is important that the subjects understand and perform the task correctly. Therefore, this may not be adequate for subjects with cognitive deficits. Furthermore, the simple fact of doing the task may be too complex, which could trigger unwanted local CBF and oxygenation changes due to neuronal activation (Thomason & Glover, 2008). Consequently, it is not possible to control shifts in the PaCO₂, which in turn leads to inter-subject variability. So, to avoid this problem, measurements of end-tidal CO₂ pressure (P_{ET}CO₂) are used to correlate with the CBF values (Thomason & Glover, 2008).

All CBF alteration induced by vasodilation or vasoconstriction can be measured using several methods that are going to be explained in the next section.

1.2.3 Measurement techniques

In this section, the main imaging methods used to assess brain perfusion are now described.

Most of CBF imaging techniques are based on the usage of a CBF tracer that is administered in the circulation and diluted in the blood. Upon the measurement of its concentration and application of an appropriate tracer kinetic theory, it is then possible to estimate the CBF, based on the concentration time curves of the tracer. One of the most common diffusible CBF tracer is Xenon 133 gas, which is inhaled and is used in Xenon computed tomography (Xe-CT). This technique allows for the measurement of CBF, however, it requires the inhalation of this tracer that is a very expensive radioactive gas and thus turns this technique into an invasive and expensive one (Pindzola et al., 2001; Yonas et al., 1991).

With the same kinetic principles, it is also possible to measure CBF using Positron Emission Tomography (PET). This technique uses the administration of ^{15}O -labelled water and oxygen as CBF tracer, though, it is necessary an onsite cyclotron which is very expensive. It also uses ionizing radiation which limits the applicability of this technique (Chen et al., 2008; Ibaraki et al., 2004).

The most widely used nuclear medicine technique for assessment of cerebral hemodynamic is the Single-photon emission computed tomography (SPECT). It is able to measure CBF using tracer kinetic theory and also the administration of a radioactive tracer, but it has a poor spatial resolution besides having the same disadvantages as PET (Shiino et al., 2003).

Another current technique for measuring CBF is Transcranial Doppler Ultrasound (TDU), which is based on the Doppler effect and uses ultrasound waves to measure the blood flow velocity through cerebral vessels with a large calibre (Topcuoglu, 2012). This flow velocity is used as an indirect way of estimating CBF. Since the acoustic impedance of the bone is much higher than that of the brain, the ultrasound transmission across the skull is limited to a few windows (Pinto, 2012). This characteristic allows the temporal window to measure the flow velocity of the middle cerebral arteries (MCA). This technique is inexpensive and widely available, which makes it very attractive. However, it can only measure the flow velocity in middle size arteries and is very dependent of the acoustic window (Pindzola et al., 2001; Topcuoglu, 2012). Therefore, it cannot estimate the regional CBF across the brain.

With MRI, it is possible to use perfusion-weighted signal acquisition techniques, which may allow the truly quantitative measurement of CBF across the whole brain. Dynamic susceptibility contrast (DSC) imaging may be used to measure perfusion based on the passage of an injected bolus of paramagnetic contrast agent, typically based on Gadolinium. More recently, a completely non-invasive technique has been proposed, where by arterial blood water is magnetically labelled and used as an endogenous CBF tracer: Arterial Spin Labelling (ASL). The main focus of ASL studies is to determine the baseline values of CBF and its changes during

brain activation (Buxton, 2005; Golay & Petersen, 2007). In the following sections, this technique will be described, since it is the technique used in this work.

1.3 ASL MRI perfusion imaging principles

In 1946, two physics groups led by Felix Bloch and Edward Purcell discovered what later was called Nuclear Magnetic Resonance (NMR) (Bloch, 1946; Purcell et al., 1946). All MRI techniques are based on these NMR physical principles. Functional Magnetic Resonance Imaging (fMRI) is one of these MRI techniques and, overall, it is used to refer to all imaging techniques that reproduce some functional aspect of the brain, like its hemodynamic (CBF). In this work, the focus is the ASL signal from fMRI, which allows the assessment of changes in hemodynamics in response to vascular challenges. In the following sections, the basic principles of MRI and ASL are going to be briefly described.

1.3.1 MRI basic principles

Bloch et al. (1946) and Purcell et al. (1946) showed that certain nuclei have an intrinsic magnetic moment that, when placed in a magnetic field B_0 , rotate at a frequency proportional to the field strength, which results in an angular momentum (Buxton, 2002). This rotation gives the charged particle a magnetic moment μ with a magnetic field associated. This notion comes from the fact that protons possess a quantum property called spin, which is related with magnetic moment. Therefore, if a nucleus contains an odd number of protons, it displays non-zero nuclear spin, like hydrogen. This atom is usually used to study biological tissues with MRI since hydrogen is a constituent of water, which is the most abundant substance in the human body (Pinto, 2012).

When at rest, where there is no magnetic field, the non-zero magnetic moment nuclei are randomly oriented and the resulting magnetization vector M is equal to zero (Fig. 1.2, a). However, when the body is exposed to a strong static magnetic field B_0 these nuclei tend to orientate with respect to the direction of B_0 . Each nucleus has one of the $2I + 1$ energy levels, where I is the nuclear spin quantum number. Since the nuclei at hand is ^1H , where $I = \frac{1}{2}$, the spins will be distributed into two energy levels, one parallel to B_0 with lower energy and another anti-parallel to B_0 with higher energy (Fig. 1.2, b). The majority of the spins tend to align in the parallel state, due to tissue's temperature and typical field strength, which results in a magnetization vector M parallel to B_0 (Fig. 1.2, b). To create an MRI signal, transitions between these two levels must be induced (Nunes, 2014; Webb, 2003)

A second magnetic field, B_1 which is transverse to B_0 and in the radiofrequency band (RF) is applied resulting in the excitement of the nuclei that changes to the higher level, creating a magnetization component in the transverse plane. This RF pulse carries the energy correspondent to the gap between the two levels at the resonance frequency, that is called Larmor frequency (ω) (Webb, 2003). This frequency is proportional to the gyromagnetic constant γ and

the B_0 (Equation 1.2). Each nucleus has a specific gyromagnetic constant and is, therefore, excited by a unique frequency.

$$\omega = \gamma B_0 \quad (1.2)$$

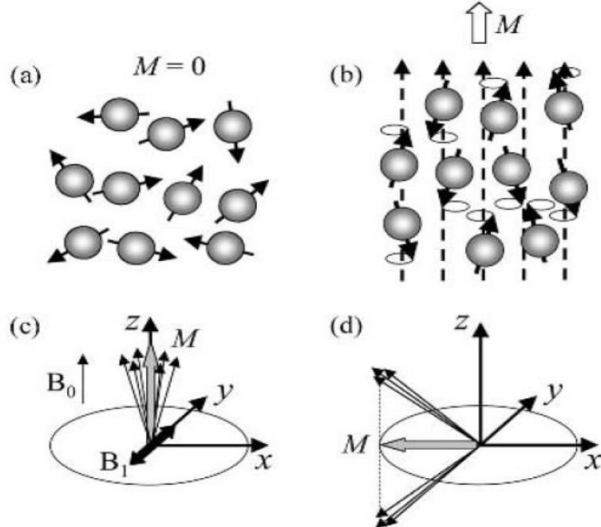


Figure 1.2 - Behaviour of a sample when placed in a strong magnetic field; a) When no magnetic field is applied, the magnetic moments are randomly oriented, yielding zero net magnetization; b) Gradually the moments align either with the field or against it; c) An oscillating magnetic field B_1 changes the orientation of the nuclear moments until there is a measurable magnetization in the transversal xy plane; d) During the application of RF pulse, where there is transversal magnetization. Adapted from Jezzard et al. (2001).

Therefore, at rest, there is no transversal magnetization and the net magnetization vector M only has the z component. In the presence of the RF pulse, the z component diminishes from its equilibrium value M_0 and the transversal xy component gains a non-zero value (Fig 1.2, c and d). Considering a RF pulse of 90° , the longitudinal component $M_z(0)$ equals zero and there is an arbitrary magnetization vector with transversal component $M_{xy}(0)$. The behaviour of the magnetization at later times is given by the Bloch equations (Equations 1.3 and 1.4) (Smith & Webb, 2011):

$$M_z = M_0(1 - e^{-\frac{t}{T_1}}) \quad (1.3)$$

$$M_{xy} = M_{xy}(0)e^{-\frac{t}{T_2}} \quad (1.4)$$

where T_1 and T_2 are the longitudinal relaxation time constant and transversal time constant, respectively. T_1 is the relaxation along the direction of B_0 and corresponds to the re-establishment of the thermal equilibrium in the local environment. T_2 is the relaxation along plane perpendicular to B_0 and comes from the loss of phase coherence caused by interactions with neighbouring nuclei. Another important factor in the transversal relaxation is the spatial variations in the strength of the magnetic field, instigated by the magnet design and different magnetic

susceptibilities of different tissues. These effects are defined as T_2^+ and are seen as an additive process to the T_2 relaxation. Which results in T_2^* (Equation 1.5) (Webb, 2003).

$$\frac{1}{T_2^*} = \frac{1}{T_2} + \frac{1}{T_2^+} \quad (1.5)$$

There are coils that are placed within the MR scanner to measure the changes in the local magnetic field and through different acquisition sequences it is possible to obtain images dependent on the parameters T_1 , T_2 and T_2^* .

1.3.2 Arterial Spin Labelling MRI

In the following sections the basic principles of Arterial Spin Labelling will be described, as well as the most common acquisition techniques, the general kinetic model and perfusion parameter estimation.

1.3.2.1 Basic principles

Nowadays, there is a relatively new and extremely interesting MRI technique for the measurement of blood perfusion, which is the Arterial Spin Labelling (ASL) (Alsop et al., 2014). This technique benefits from the high abundance of water molecules in the human body and uses endogenous diffusible tracer, which in this case are the magnetically labelled blood water protons. This means that this technique is non-invasive and, therefore, can be repeated as long as needed per session. One other important characteristic is that ASL allows for the direct and quantitative mapping of CBF changes, contrary to, for example, Blood Oxygenation Level Dependent (BOLD) methods (Pinto, 2012).

The ASL technique has two main stages. The first stage is the labelling of arterial blood water molecules that end up in the imaging region, or region of interest (ROI), through the inversion or saturation of the longitudinal component of magnetization. This labelling is achieved using an RF pulse that is responsible for the inversion or saturation. The labelled blood, with time, flows into the imaging slices and eventually relaxes towards the equilibrium with the longitudinal relaxation time constant T_1 of the blood. Then, after a certain interval, known as inversion time (TI), the magnetization is measured through the acquisition of an image with the slices of interest, that is called tag image or label image. This time delay allows for the labelled blood to reach the slices of the imaging region (Luh et al., 1999).

The second stage is the acquisition of a second image, the control image, in the same slices of interest, with everything the same except for the labelling process, i.e., there is no RF pulse. Here the blood is already fully relaxed and the image is known as the control image.

For the ASL technique to work, both the tag/label and control images have to be acquired (Figure 1.3). Ideally, they would be acquired at the same time in order to have the exact same conditions in both images, but that cannot be done, so typically the control image is acquired with a certain time interval from the tag image. This interval is called the repetition time, TR .

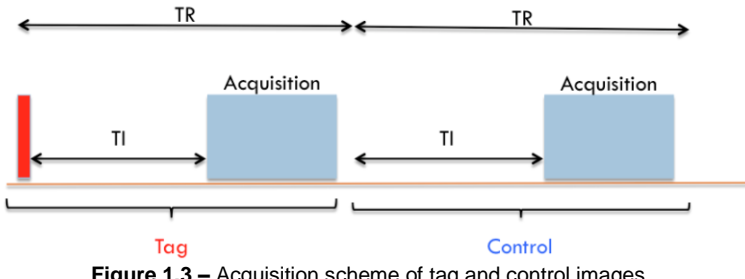


Figure 1.3 – Acquisition scheme of tag and control images.

After the acquisition of both tag and control images, a subtraction of these two images is done in order to remove the contribution of the static tissue to the tag image, from which results a magnetization difference image (Equation 1.6). This image is roughly proportional to CBF at long acquisition times.

$$CBF \propto \Delta M = M_{control} - M_{tag} \quad (1.6)$$

As a result, the greater the flow of labelled arterial blood water molecules into the imaging region, the greater the ΔM (Figure 1.4), which provides a perfusion-weighted signal.

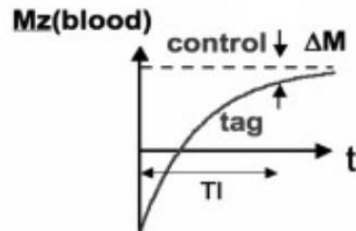


Figure 1.4 – Longitudinal relaxation of magnetization. Adapted from Liu & Brown (2007).

One clear limitation of the ASL technique is the low Signal-to-Noise ratio (SNR), since the subtraction between the control and tag images leaves a magnetization difference around 1% of the total signal (for the adult human brain, at 3 Tesla), which is less than the noise (Alsop et al., 2014). Therefore, one way of trying to get a better SNR is through averaging. Since the ASL is non-invasive and non-ionizing it is possible to repeat several times both the control and tag images, with a minimum TR between repetitions, and then it is a simple question of averaging the control and tag images in order to obtain a better SNR (Liu & Brown, 2007).

At this point, it is relevant to introduce the other two parameters of interest for this work besides CBF, which are the BAT and the aBV. BAT is defined as the time it takes for the first molecule of labelled blood water to reach the imaging region. This time is relative, depending on where the labelling is done, and the blood transit time through the vasculature. There are certain cerebrovascular diseases in which BAT may be so great that by the time the blood reaches the tissue being imaged, the blood is fully relaxed and there is no signal. One other problem that may arise is the possibility of the ASL signal being contaminated by the presence of labelled blood in large arterial vessels that are intended to perfuse tissues in a more distal capillary bed and not the imaging region itself (Chappell et al., 2010). This problem leads to the other parameter of interest, aBV, that is the arterial blood volume fraction, i.e., it is the percentage of intravascular arterial labelled water that is present in a certain voxel (Sousa et al., 2013). Another aspect worth mention is the fact that, as water molecules leave the capillary bed into the extra-vascular space, the decay of the magnetization, which is initially controlled by the T_1 of the blood, starts to be governed by the T_1 of the tissue (Günther, 2013).

In a further section, the exact relationship between the three parameters of interest (CBF, BAT, aBV) and the magnetization difference, ΔM , will be described using an appropriate kinetic model.

1.3.2.2 Acquisition techniques

Labelling is very important in this technique, and it is essential to explain with some detail how this is done and the different types of approaches.

One way of labelling is the continuous labelling method (CASL) (Williams et al., 1992). Inside this method there are two distinct forms, the normal continuous ASL and the pseudo-continuous ASL (PCASL) (Dai et al., 2008). In the first one, it is applied one single, long label, typically 1 to 3s, in which an effective continuous RF pulse causes the inversion of the blood flowing through a single labelling plane (Figure 1.5). In the PCASL, a long train of slice-selective RF pulses (around 1000 at a rate of one per millisecond) replaces the continuous RF pulse applied at the labelling plane (Figure 1.5). Nowadays PCASL is the desired implementation because it is compatible with state of the art body coil RF transmission hardware, that are required on clinical MRI scanners and it delivers superior labelling efficiency (Alsop et al., 2014).

The other way of labelling is the pulsed labelling method (PASL) (Wong et al., 1997). This method requires the use of a single short RF pulse, normally with a duration of 10 to 20 ms that inverts a thick slab of tissue, including arterial blood water molecules (Figure 1.5). This slab, which constitutes the labelling bolus, is 10 to 20 cm thick because of the spatial coverage of the transmit RF coil. The duration of the pulse has to be very short, since the arterial blood water molecules, that are in the bolus, have high velocity flow (Alsop et al., 2014). In this work, the labelling method employed was the PASL.

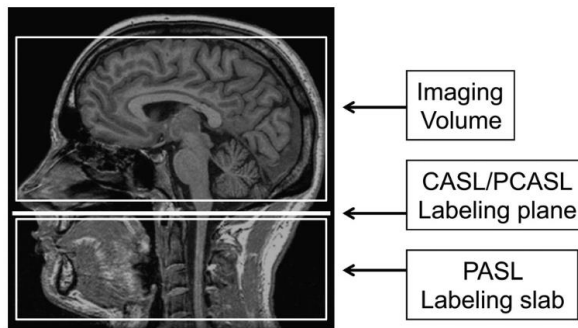


Figure 1.5 – Scheme for imaging and labelling regions for CASL, PCASL and PASL.

Adapted from Alsop et al. (2014).

There are several different aspects to be mentioned about the acquisition sequence, like the PASL scheme used, the slab saturation scheme used and the image acquisition method.

Various types of PASL schemes exist, but the one employed in this work was the proximal inversion with a control for off-resonance effects (PICORE) (Çavuşoğlu et al., 2009; Wong et al., 1997). In this method, the labelling is applied using a slab selective inversion proximal to the imaging slice and the control is an off resonance inversion pulse that is applied at the same offset frequency relative to the imaging slice but with no slab selective gradient, unlike the labelling. This method is the natural choice when the arterial blood is entering the slice from a known direction, since the tagging occurs only from one side (Wong et al., 1997).

About the slab saturation scheme, the one used was the quantitative imaging of brain perfusion using a single subtraction, second version with thin-slice TI_1 periodic saturation, known as Q2TIPS. This scheme is an improved version of the QUIPSS II scheme (Luh et al., 1999; Wong et al., 1998). The QUIPSS II introduced a saturation pulse between the inversion RF pulse and the image acquisition that enhanced the quantification of perfusion imaging through the minimization of two systematic errors. One of them was the previously mentioned contamination by labelled blood in large arterial vessels. The other was the variable BAT from the distal edge of the bolus region to the beginning of the imaging region. However this scheme still had residual errors and therefore one thought was to replace this saturation pulse with a train of thin-slice periodic saturation pulses applied at the distal edge of the labelled region from TI_1 to TI_{1S} (Figure 1.6), which is the Q2TIPS scheme (Luh et al., 1999). This change improved the accuracy of brain perfusion quantification (Günther, 2013). The main advantage of Q2TIPS is that it fixes the temporal duration of the labelling bolus. The scheme itself is present in the Figure 1.6.

About the image acquisition, the method employed was the Echo Planar Imaging (EPI) acquired at TI_2 (Figure 1.6), which is the most used acquisition sequence for ASL data.

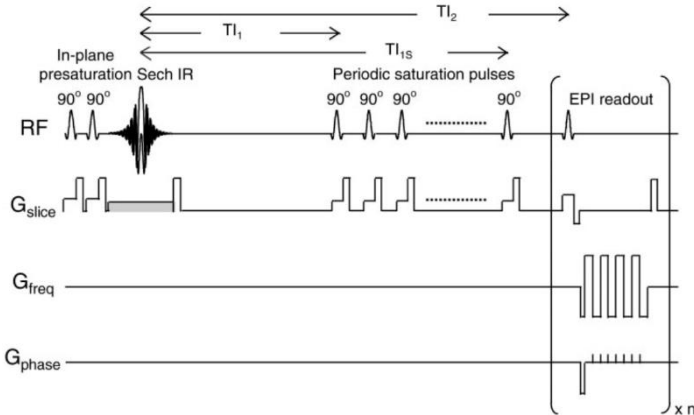


Figure 1.6 – Pulse sequence for Q2TIPS. Double in-plane pre-saturation pulse followed by sech inversion labelling pulses. The grey gradient is for alternately applying tag and control images. Periodic pulses from TI_1 to TI_{1s} consist of a train of excitation pulses. EPI image acquisition at TI_2 . Adapted from Luh et al. (1999).

With all this, all that is left is the actual method of estimation of the parameters of interest and the kinetic model used to achieve this. In the following section, the kinetic model will be introduced.

1.3.2.3 General kinetic model

Having in mind the previous section, it is clear that the amount of magnetization difference, ΔM , at a certain time t depends on several aspects like, the efficiency of delivery of magnetization present in arterial blood, the clearance of the magnetization by venous outflow and the normal longitudinal relaxation.

In the section 1.3.2.1, it was shown that the magnetization difference, ΔM , is somewhat proportional to CBF. However, the exact relationship between CBF and ΔM signal can be derived if this magnetization difference is treated as the concentration of a diffusible tracer (CBF tracer) and in this condition, it is possible to apply appropriate tracer kinetic principles to estimate accurately the CBF, as well as BAT and aBV. This method is called General Kinetic Model (Buxton et al., 1998) and will be described in detail now.

This method varies according to the type of labelling used (PASL, CASL/PASL). Since in this work the labelling method employed was the PASL, the pulsed ASL signal of the tissue component can be described by the General Kinetic Model taking the form of Equation 1.7 (Buxton et al., 1998; Chappell et al., 2010):

$$\Delta M_{tiss}(t) = \begin{cases} 0, & t < \Delta t \\ \frac{2\alpha M_{0a} f e^{-\frac{t}{T_{1app}}}}{R} (e^{Rt} - e^{R\Delta t}), & \Delta t \leq t \leq \Delta t + \tau \\ \frac{2\alpha M_{0a} f e^{-\frac{t}{T_{1app}}}}{R} (e^{R(\Delta t + \tau)} - e^{R\Delta t}), & \Delta t + \tau < t \end{cases} \quad (1.7)$$

where $R = \frac{1}{T_{1app}} - \frac{1}{T_{1a}}$ and $T_{1app} = \frac{1}{T_1} + \frac{f}{\lambda}$, f is the CBF, Δt is the BAT, M_{0a} is the equilibrium magnetization of the arterial blood, the τ is the bolus duration of the labelled blood bolus and α is the inversion efficiency, defined as the fraction of inversion of the arterial magnetization at the time of labelling (equal to 0.9). T_1 and T_{1a} are the tissue and arterial longitudinal relaxation time constants and the λ is the blood/tissue partition coefficient, which is 0.9 on average for the whole brain (Herscovitch & Raichle, 1985).

As mentioned several times before, the ASL signal may be contaminated by the labelled arterial blood in regions of larger vessels that are destined to regions that are more distal. Consequently, in some voxels that have a large arterial vessel, an extra component to the signal may appear from intravascular labelled water (macro-vascular signal). With this in mind, an extra macro-vascular component of the General Kinetic Model arises, that can be described by Equation 1.8 (Chappell et al., 2010):

$$\Delta M_{art}(t) = \begin{cases} 0, & t < \Delta t_a \\ 2\alpha M_{0a} e^{-\frac{t}{T_{1a}}} aBV, & \Delta t_a \leq t \leq \Delta t_a + \tau_a \\ 0, & \Delta t_a + \tau_a < t \end{cases} \quad (1.8)$$

where aBV is the arterial blood volume fraction, Δt_a and τ_a are the BAT and bolus duration of the arterial bolus. Theoretically, the BAT of the macro-vascular component should be shorter than the tissue component since the water molecules in the large vessels have greater velocity than that of the capillary beds.

Therefore, the total ASL signal from any voxel is the sum of the tissue and macro-vascular components (Equation 1.9):

$$\Delta M(t) = \Delta M_{tiss}(t) + \Delta M_{art}(t) \quad (1.9)$$

With this kinetic model, a very characteristic curve of the pulsed ASL signal over time arises. In the Figure 1.7 it is possible to see the tissue and vascular component curves as well as the correspondent sum. With time ΔM tends to zero as the relaxation continues.

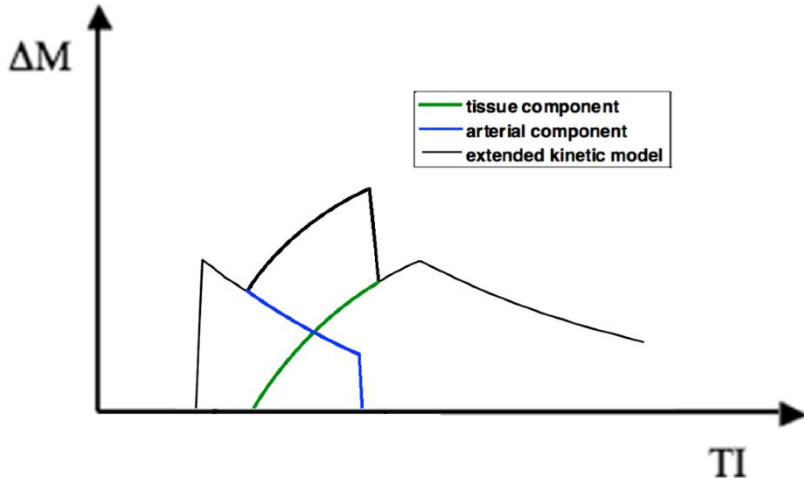


Figure 1.7 – Theoretical pulsed ASL signal curves of the tissue and macro-vascular components as well as the total ASL signal curve.

One of the goals of this work is the estimation of the parameters CBF, BAT and aBV. Therefore, through the General Kinetic Model (Equation 1.7 and 1.8) it is possible to estimate them, but it is necessary to sample the ASL signal across multiple post-labelling delays (PLDs), i.e., use several inversion times (TI) so that the fitting of the kinetic model allows for the estimation not only of CBF (for this, only one relatively long TI would be required), but also of the other parameters of interest (Chappell et al., 2010). So, in the ASL curve in Figure 1.7, some time-points are chosen (TIs) and used in the Equations 1.7 and 1.8 in order to estimate the parameters of interest. This estimation is going to be described in the following section.

1.3.2.4 Parameter estimation (Bayesian Inference)

As mentioned before, the next step is the estimation of the parameters of interest (CBF, BAT, aBV). The parameter estimation is achieved by the kinetic model inversion. In this work, we use the probabilistic inference approach for nonlinear model fitting proposed by (Chappell et al., 2009) and implemented in FSL (FSL 5.0.8 version, <http://fsl.fmrib.ox.ac.uk/fsl/fslwiki/FSL>).

This Bayesian approach is based on the Bayes' theorem, which given the data y (in this case ASL signal, or ΔM) and the model \mathcal{M} (General Kinetic Model), defines a posterior probability distribution function (PDF) for the model parameters w (Equation 1.10).

$$P(w|y, \mathcal{M}) = \frac{P(y, w|\mathcal{M})}{P(y|\mathcal{M})} = \frac{P(y|w, \mathcal{M}) P(w|\mathcal{M})}{P(y|\mathcal{M})} \quad (1.10)$$

where $P(w|y, \mathcal{M})$ is the posterior probability of the parameters given the data and the model, $P(y|w, \mathcal{M})$ is the likelihood of the data given the model with parameters, $P(w|\mathcal{M})$ is the

prior probability of the parameters for this model and the $P(y|\mathcal{M})$ is the evidence for the data given the model (Chappell et al., 2009). It is common to ignore the normalization of the posterior probability distribution, therefore the evidence can be neglected and for a certain model the Equation 1.11 is then obtained,

$$P(w|y) \propto P(y|w) P(w) \quad (1.11)$$

The model includes both the description of the kinetic curve (Figure 1.7) and the description of the noise, in this case white noise. It is important mentioning that Equation 1.11 gives the posterior PDF on all parameters, when most of the times the attention is only on an interesting subset of parameters. To obtain these optimal posterior PDFs marginalization is done, in which integrations are done over all the other parameters to obtain the posterior PDF of interest (Equation 1.12) (Woolrich et al., 2006).

$$P(w_I|y, \mathcal{M}) = \int_{w_{I-}} P(w|y, \mathcal{M}) dw_{I-} \quad (1.12)$$

where w_I are the parameters of interest and w_{I-} are all the other parameters.

For the General Kinetic Model, the posterior PDF is not analytically tractable. So a variational Bayes approach is used (Attias, 1999) where a product of a number of known distributions is used to approximate the posterior distribution. This technique is less computationally expensive, hence being used. Chappell et al. (2009) showed that these approximations are reasonable for the ASL estimation. For some parameters there is no prior information available, but even then the results from Chappell et al. (2009) show that this method is reduced to the techniques that use nonlinear least squares estimators, which is a good sign for the estimation method.

The main advantage of this approach is that the prior knowledge about a certain parameter based on its physiological information can be used. When speaking of ASL data, this aspect is very important due to the poor SNR and this way the prior information can be used to normalize the problem. The prior value itself is the range of values that the parameter might take (Chappell et al., 2010).

1.4 State-of-the-art

In this section, the state of the art relevant to the goals of this work are described, by reviewing the literature on CBF assessment in both baseline and hypoxia conditions using ASL MRI.

1.4.1 CBF assessment in baseline and hypocapnia conditions

CBF assessment has been successfully performed using several different methods, like ASL MRI, both during baseline conditions as well as during hypercapnia and hypocapnia challenges.

Sousa et al. (2014) investigated the reproducibility of the CBF, BAT and aBV from arterial spin labelling data. One of the goals was also to test different estimation methods, like Bayesian inference methods, least squares fitting and a model-free approach. The average range of CBF was 45-59 ml/100g/min, 0.7-1.0 seconds for BAT and 0.35-1.17 % for aBV. In the conclusion, reproducible estimates of all three parameters was found using the Bayesian and least squares methods (Sousa et al., 2014).

Kastrup et al. (1999) made a study to assess the regional CBF changes in response to a breath-holding (BH) technique using ASL MRI. Here, a repeated BH challenge induced an overall increase of the CBF. These changes depended on the duration of the BH, but in general the results showed small inter-individual variability (Kastrup et al., 1999).

Other studies focused instead on the CBF response to hypercapnia. Donahue et al. (2014) performed the investigation with ASL MRI and showed that when in hypercapnia, the CBF increases as expected and the BAT tends to bias the functional ASL data (Donahue et al., 2014). Ho et al. (2011) performed a similar study, where they concluded that there are different vascular mechanisms for large and small segments, which may be condition specific.

As for the comparison of baseline versus hypocapnia, some studies address this issue, but not always to estimate the CBF. Like Sousa et al. (2014) that tested the reproducibility of the cerebrovascular reactivity using BOLD fMRI (functional MRI) when in hypocapnia caused by paced deep breathing. The results showed a good reproducibility of the hypocapnic CVR maps using PDB techniques (Sousa et al., 2014). Previously, another study revealed that PDB and consequently, hypocapnia, offers an alternative method for mapping the cerebrovascular reactivity, also using BOLD fMRI (Bright et al., 2009).

CBF changes during hypocapnia have been measured with other techniques. Ito et al. (2003) that used positron emission tomography and concluded that there was a decrease of the vascular blood velocity, since the degree of decrease of CBF in hypocapnia was greater than that of the CBV (Ito et al., 2003). Another study aimed to compare the Kety-Schmidt inert gas technique with argon and the transcerebral double-indicator dilution technique (TCID) (Mielck et al., 2001) in the assessment of CBF in hypocapnia conditions. The conclusion was that the TCID is less time-consuming and an alternative way to measure global CBF (Wietasch et al., 2000).

Chen et al. (2010) studied the CBF and CBV (cerebral blood volume) changes in response to both hypocapnia and hypercapnia, using ASL sequence. The results exhibited a robust increase of CBF, venous CBV in hypercapnia and a reduction of both in hypocapnia, which confirmed that the BOLD-specific flow volume relationship was similar to the characterizing

neuronal activation, during CO₂ challenges (Chen & Pike, 2010). Because only this study assessed CBF during hypocapnia using ASL MRI, we wished to further investigate the perfusion parameters BAT and aBV during hypocapnia, by using a multi-PLD ASL technique.

1.5 Thesis aims and outline

As shown in the previous section, the set of measuring the CBF, and the other parameters of interest, in baseline and hypocapnia and using the ASL MRI technique is something that is not quite explored.

Therefore, the main goal of this thesis is to develop an appropriate kinetic modelling approach for the quantitative mapping of brain perfusion, bolus arrival time and arterial blood volume, based on multiple post-labelling delays (PLDs) ASL MRI acquisitions, during both baseline and hypocapnia conditions. Another important goal is to explore the parameters' priors in order to determine the optimal values, so that the model estimation can be efficient. In specific, the BAT prior is of highest interest due to the critical importance that this parameter has on the whole analysis and the high constraint that exists in this prior.

The first chapter introduced the theoretical concepts related with this work. The rest of the dissertation is organized in the Chapter 2 that presents the methods used in the data acquisition. Chapter 3 shows the results and discussion of the parameters' estimation mean values and the comparison of the two conditions used, baseline and hypocapnia. Finally, the Chapter 4 is where the conclusions are presented.

2 Materials & Methods

This chapter provides a detailed description of the materials and methods used in this work with the goal of estimating the parameters of interest and compare the two conditions. Two types of data were acquired, ASL and $P_{ET}CO_2$ data. It also includes the data analysis where several pre-processing stages were done, the model fitting used to estimate the parameters, with all its variants, in both conditions and the statistical analysis employed to assess the significance of the values obtained.

2.1 Data acquisition

The data used in this work was acquired previously by colleagues from the NeuroPhysLM project. The details of this data acquisition are going to be described in the next section.

2.1.1 Subjects and tasks

An initial group of 12 healthy subjects (6 males, age: 24.7 ± 2.5 years) was studied at Hospital da Luz. Subjects underwent two multi-PLD PASL acquisitions, one during REST and one during PDB. The total scan duration was approximately 15 minutes. In the REST acquisition the subjects did not receive any instruction. In the PDB periods the subjects were asked to breathe more intensely so as to increase the tidal volume while maintaining a steady head position.

This was done by displaying visual instructions using stimulus presentation software, NORDIC NEURO LAB's Nordic fMRI solution (www.nordicneruolab.com). The whole task involves an alternating "inspire" and "expire", during PDB, with "breathe normally" instructions (Figure 2.1). The PDB period consists of 2 s of inspiration and 3 s expiration, which results in a breathing rate of 12 breaths/min (Sousa et al., 2014).

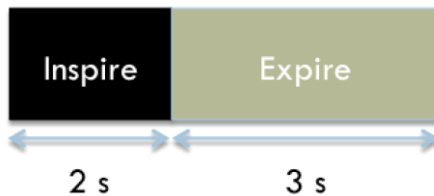


Figure 2.1 – Basic unit of PDB period. Both “inspire” and “expire” are repeated 8 times, leaving 40 s of the PDB interval.

2.1.2 Imaging

All the imaging acquisition was performed on a 3T Siemens Verio scanner using a 12-channel radio frequency coil.

As previously mentioned, the pulsed ASL data was acquired using a PICORE-Q2TIPS sequence, with Gradient-Echo EPI readout, repetition time (TR) of 2500 ms and echo time (TE) of 19 ms (one subject used $TE = 11$ ms). The inversion times used (TI_2) varied from 400 – 2400 ms in steps of 200 ms with each control-tag pair repeated eight times, for averaging issues,

yielding to 176 brain volumes. Another inversion time was acquired, $TI_2 = 50\text{ ms}$, to be used in the off-resonance correction step. As mentioned in previous sections, the Q2TIPS technique allowed the limitation of the bolus duration to 750 ms . The RF pulse was applied to a 10 cm thick labelling region, which was positioned 18.8 mm below the initial slice from the imaging region. The voxel resolution used was $3.5 \times 3.5 \times 7.0\text{ mm}^3$. For 7 of the subjects, 9 contiguous slices were acquired, yielding an image size of $64 \times 64 \times 9$. For the rest of the subjects 28 contiguous slices were used, leaving the image size to be $64 \times 64 \times 28$.

These 7 subjects also had BOLD images acquired using a Gradient-Echo EPI sequence with $TR/TE = 2500/50\text{ ms}$ and 110 brain volumes from 18 contiguous slices, yielding an image of $64 \times 64 \times 18$ with a voxel resolution of $3.5 \times 3.5 \times 7.0\text{ mm}^3$. These images were acquired in order to help in a specific step of the data analysis that will be explained later.

A T_1 -weighted structural image was obtained using an MPRAGE sequence, with $TR/TE = 2250/2.26\text{ ms}$, 144 slices and voxel resolution of $1 \times 1 \times 1\text{ mm}^3$, with the goal of providing a high-resolution structural image for every subject.

During the entire acquisition, the subjects were restrained with head system of lateral padding in order to prevent head motion that is harmful for the image acquisition.

2.1.3 $P_{ET}CO_2$ recording

During the entire experiment, the end-tidal carbon dioxide pressure ($P_{ET}CO_2$) of each exhalation was monitored using a capnograph (Cap10 Capnograph, Medlab GmbH) for eight of all subjects. The other four subjects had the end-tidal carbon dioxide pressure monitored through a CO_2 monitor (PN 8050. Dräger, Lübeck, Germany). Both methods used a nasal cannula connected to the capnograph and CO_2 monitor. This $P_{ET}CO_2$ recording allowed the registration of the values for further analysis. For the baseline condition no additional task was performed, just the normal ASL acquisition sequence, also with the registration of the $P_{ET}CO_2$ values. REST and PDB data acquisitions were randomly chosen across subjects. However, when the first condition acquired was the PDB, an additional break was necessary to ensure that the subject was fully recovered from the task so that the REST acquisition had no traces of the PDB condition present.

After the acquisition, the data saved consisted of the $P_{ET}CO_2$ values across time to which the mean value for both REST and PDB condition were calculated. For further analysis, it was necessary to obtain the mean difference of the $P_{ET}CO_2$ from both conditions, $\Delta P_{ET}CO_2$, for each subject. This value was obtained by subtracting the mean $P_{ET}CO_2$ value during REST from the mean $P_{ET}CO_2$ value during PDB. Since the PDB task is designed to cause hypocapnia, in theory the PDB $P_{ET}CO_2$ value should be smaller than the REST value, yielding a positive $\Delta P_{ET}CO_2$.

The subjects that were monitored using the capnograph had the time courses of the respiratory activity acquired, i.e. the $P_{ET}CO_2$ values across time. Then, the mean $P_{ET}CO_2$ value of

each condition was calculated. For the subjects where the acquisition was performed with the CO₂ monitor only the difference values, ΔP_{ET}CO₂, were available.

Besides this, a statistical analysis (unpaired t-test assuming equal variances, $p < 0.05$) was performed between the mean P_{ET}CO₂ values of both conditions and their time courses, from each subject.

2.2 Data analysis

For the analysis of the ASL data the tools available in FMRIB Software Library (FSL 5.0.8 version, <http://fsl.fmrib.ox.ac.uk/fsl/fslwiki/FSL>) (Jenkinson et al., 2012; Smith et al., 2004; Woolrich et al., 2009) were used, as well as in-house routines written in Matlab (version 2014b, <http://mathworks.com>). The essential analysis of this work was performed using FSL Bayesian Inference for Arterial Spin Labelling MRI (BASIL), among other tools used for all the pre-processing stages, image visualization and statistical analysis.

In the next sections, the several steps and tools used in the data analysis will be carefully described.

2.2.1 Pre-processing

The pre-processing of the ASL data collected for this work consisted on motion correction, image registration, tag-control differencing, off-resonance correction and calibration of the data. These steps will be described in the following sections.

2.2.1.1 Preliminary corrections

First, it was necessary to re-orient the structural images to the same orientation as the functional (ASL) images, as they did not have the same orientation when acquired. This was done using the FSL tool `fslreorient2std` from the Fslutils toolbox. Then, the structural and BOLD images (for the subjects where it was acquired) were brain-extracted using the FSL brain extraction tool (BET) (Smith, 2002). This tool removes the non-brain structures, like the skull, from an image of the whole head. Naturally, after the extraction, all images were analysed to see if it was done correctly, since the algorithm sets default coordinates for the centre of the brain. For some images, the coordinates had to be set manually after careful visual analysis. In Figure 2.2 it is possible to see an example of this extraction performed by BET.

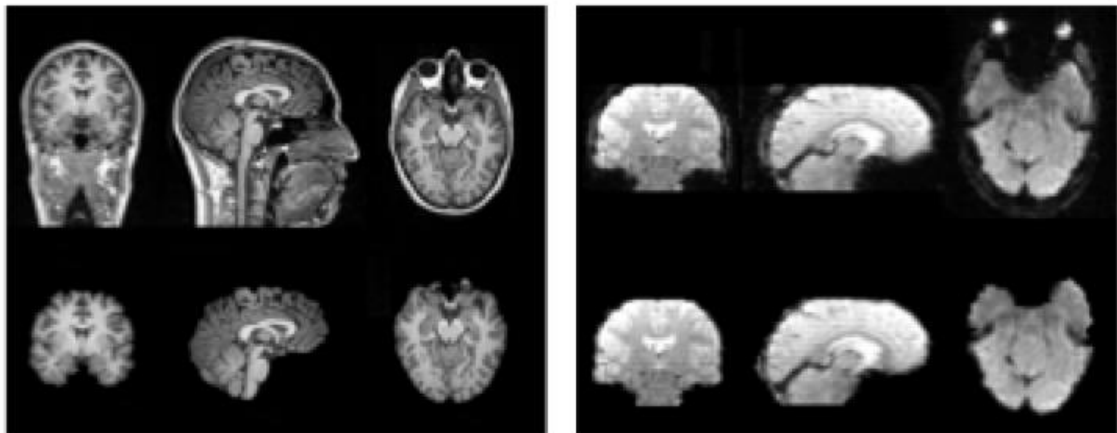


Figure 2.2 - Example of a subject's structural (LEFT) and BOLD (RIGHT) images: (left to right: sagittal, coronal and axial) before (top) and after (bottom) brain extraction using BET.

As mentioned before, some precautions were taken in the image acquisition to ensure there was no head movement of the subject, since this is a relevant issue in any fMRI study. However, there is no guarantee that there was no movement, especially during the PDB task, which is more challenging for the subject. Therefore, a motion correction step was applied to the 4D ASL data, where the tool used for this purpose was the MCFLIRT tool (FMRIB's Motion Correction) (Jenkinson et al., 2002). The 4D ASL data consisted of the ASL time course from the REST condition concatenated with the ASL time course from the PDB condition. The MCFLIRT tool, applied to the 4D ASL data, removed the effect of head motion during the experiment by realigning the imaging volumes over time, through registration techniques implemented in FMRIB's Linear Registration Tool (FLIRT) (Greve & Fischl, 2009; Jenkinson et al., 2002; Jenkinson & Smith, 2001), which is an automated and robust tool for linear affine brain image registration. This way, the ASL data from REST and PDB conditions was also aligned to each other, which is very useful in further steps.

Besides this, the 4D ASL data was again separated in the original REST and PDB condition to assess the head movement present in each data time courses separately. In the Figure 2.3 an example of the motion correction report is presented, where the relative displacement is calculated relative to the previous time point and the absolute displacement corresponds to the head position at each time point relative to the volume in the middle of the series. The motion correction reports for all subjects in the two conditions were then analyzed to see if there was a pattern that could be identified across conditions.

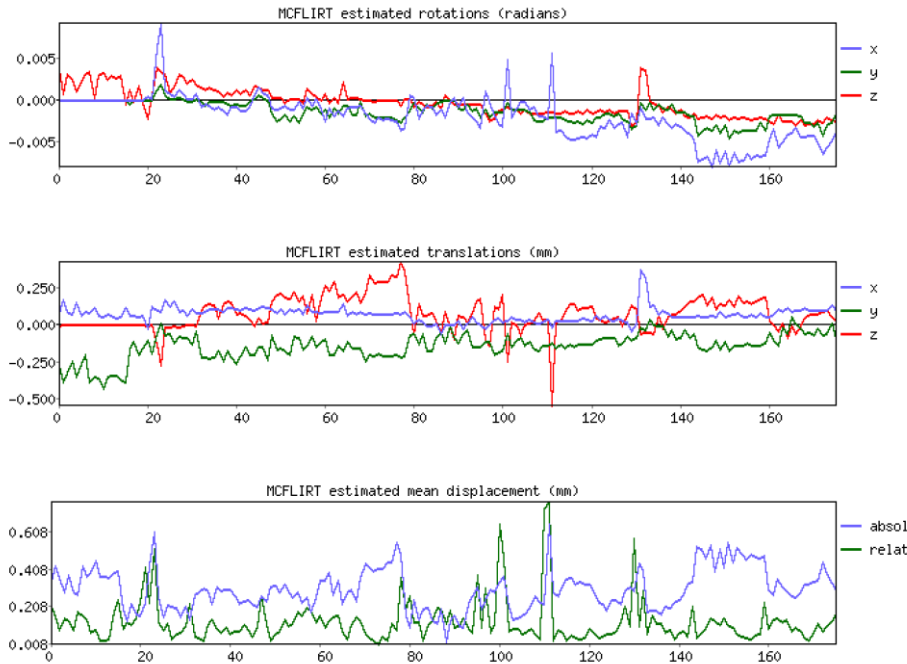


Figure 2.3 - Motion correction results for one example subject. The x axis represents the number of imaging volumes (TR=2.5s).

2.2.1.2 Image registration

When performing fMRI studies, it is often useful to register the functional images to the structural space of the individual and to a standard space, in order to enable comparisons between conditions within each subject and also across subjects. The structural space enables comparisons within a subject's brain between different conditions and the standard space allows comparisons of different subject's brains. Therefore, it is obvious that registration is an essential step for multi-subject analysis. This image registration involves transformation matrices that allow passing from the functional space to the structural and from this to the standard space.

In this work, the registration was done using the FLIRT tool, previously mentioned, that determines the transformation matrix from one space to another if the images from the two spaces involved are given, assuming a linear transformation in a number of degrees of freedom. Then it is possible to apply that transformation matrix to any image from the origin space so as to have that image in the space wanted. For example, to have a functional image in the structural space, it is necessary to create the transformation matrix from the functional to structural space and then apply it to the functional image.

For the ASL data, one example volume of the low-resolution functional images, i.e. the 4D ASL data, was registered to the subject's high-resolution structural image (the subject's T_1 -weighted structural image after brain extraction). Then, this high-resolution image was registered to the standard space, using the MNI152 T_1 -weighted image. Lastly, the two transformation matrices were concatenated into a third, which enabled the functional image to be transformed into the standard space. An example of the registration process is shown in Figure 2.4.

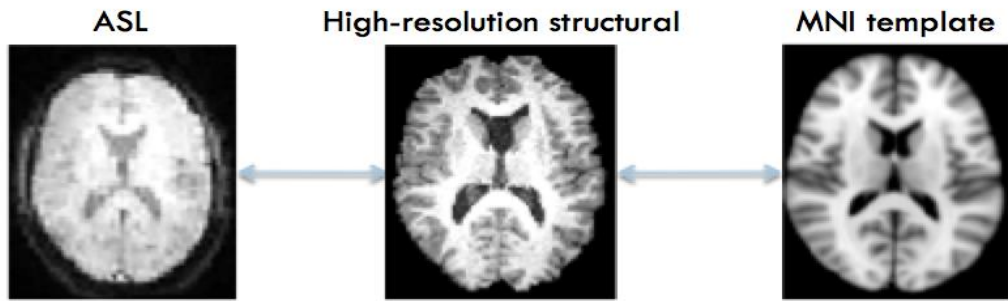


Figure 2.4 – Image registration example.

For those seven subjects where only 9 contiguous slices were acquired, an extra step was necessary since this ASL data had limited brain coverage and the structural image had full brain coverage. So, this extra step was performed in the beginning, where the low-resolution functional image (4D ASL data) was registered to a full brain BOLD image (middle volume) and then this image was registered to the high-resolution structural image. In Figure 2.5, this small change to the image registration is presented, where all images were registered to the standard space. All transformation matrices, in both cases, were saved for posterior analysis where they are needed. As it is possible to see from Figures 2.4 and 2.5, the registration process is adequate.

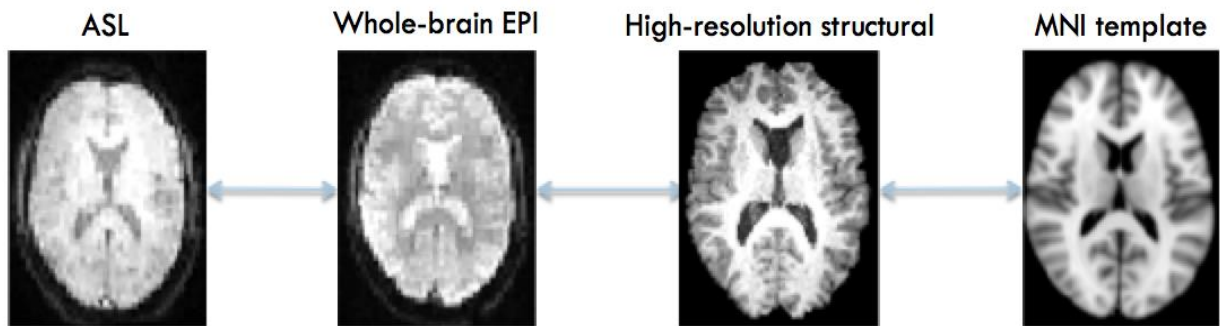


Figure 2.5 – Example of the image registrations done with the additional BOLD image step.

2.2.1.3 Tag-control differencing

As mentioned in the Introduction chapter, the ASL raw data consists of control and tag images that are acquired for later tag-control differencing pre-processing. In this section it is explained what this pre-processing stage actually is and how it is done.

First, after the acquisition of the raw data for both conditions (REST and PDB), the control and tag images of each inversion time (TI) were merged together, yielding a 4D raw image with 176 volumes (for each of the 11 TI 's, 16 volumes were acquired, 8 for tag and 8 for control), yielding a total of n images). There are several methods that can be used to obtain the ΔM images, such as pair-wise subtraction, surround subtraction and *sinc* subtraction (Liu & Brown, 2007).

Since we were interested only in the average ΔM images for each TI , the simplest methods of pair-wise subtraction was used in this work (Liu & Wong, 2005), which consist of the simple subtraction of adjacent images (Equation 2.1):

$$\left[D_1, D_2, \dots, D_{\frac{n}{2}} \right] = \left[C_1 - T_1, C_2 - T_2, \dots, C_{\frac{n}{2}} - T_{\frac{n}{2}} \right] \quad (2.1)$$

where C_i and T_i are the control and tag images, respectively, with $i = 1, 2, \dots, \frac{n}{2}$. This pairwise subtraction was performed using the *asl_file* command line tool of the FSL BASIL toolbox (Chappell et al., 2009). The averaging needed for better SNR was also done using this function, yielding the mean magnetization difference maps for each inversion time. An example of the tag-control differencing is presented in Figure 2.6.

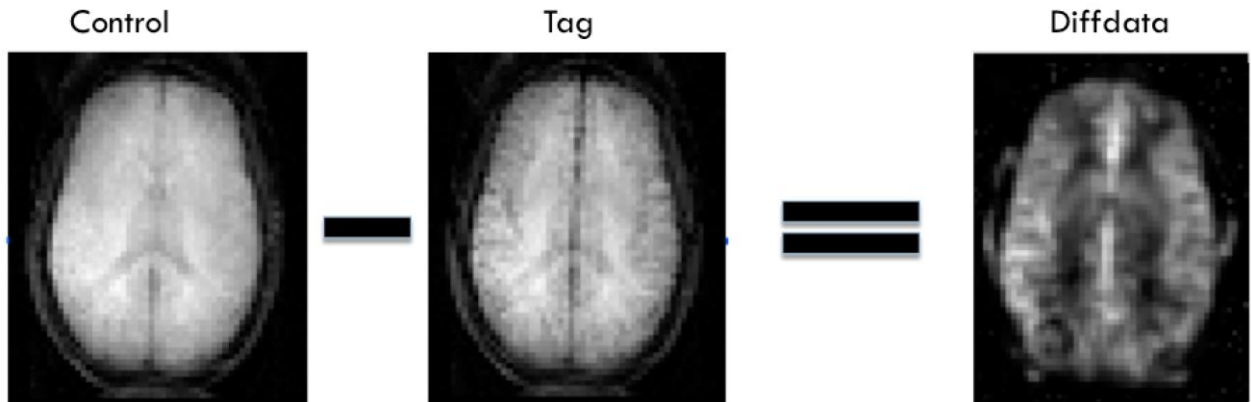


Figure 2.6 – Tag-control differencing example. The Diffdata image corresponds to the tag-control differenced data.

Then, the control volumes time series was extracted from the 4D raw image, as they will be necessary for a further step in the analysis.

2.2.1.4 Off-resonance correction

Now that magnetization difference maps have been created and averaged, the next step was to perform off-resonance correction. This effect is caused by an imperfect inversion slice profile, which happens due to a direct excitation of the labelling pulse in the imaging region. To estimate this effect, the magnetization difference map of the inversion time $TI_2 = 50\text{ ms}$ is calculated and used as a reference, since at this early time in the acquisition it is not expected

that the imaging region already has labelled blood water molecules; hence, any non-zero magnetization difference will be a signal offset due to the off-resonance effect.

The signal offset δM could then be determined at each TI_2 acquired and at each slice, based on the longitudinal relaxation with the tissue time constant T_{1t} (Figueiredo et al., 2005):

$$\delta M(TI_2(z), z) = \delta M(TI_0, z) e^{-\frac{TI_2(z)+TI_0}{T_{1t}}} \quad (2.2)$$

where TI_0 is the $TI_2 = 50\text{ ms}$ and $\delta M(TI_0, z)$ is the magnetization difference at TI_0 and specific z . Then it is only a matter of subtracting this signal offset, δM , from the acquired magnetization difference, ΔM_{acq} , in order to obtain the corrected magnetization difference image, ΔM_{corr} :

$$\Delta M_{corr}(TI_2(z), z) = \Delta M_{acq}(TI_2(z), z) - \delta M(TI_2(z), z) \quad (2.3)$$

This correction step was performed using a Matlab routine that by receiving the averaged magnetization difference map of all inversion times and the raw ASL data of the $TI_2 = 50\text{ ms}$, outputted the corrected magnetization difference maps of each inversion time used for the posterior fitting.

2.2.1.5 Calibration

In the section 1.3.2.3, it was shown that M_{0a} is the equilibrium magnetization of the arterial blood. Knowing the value of this term is essential for the parameter's estimations because otherwise, only relative values of the parameters would be obtained and for the goals of this work, absolute values have to be estimated in order to enable the quantitative comparison. To find this M_{0a} value, magnetization from voxels only filled with blood would have to be measured. However this is not possible as the standard ASL spatial resolution is $\sim 3\text{-}4\text{ mm}^3$ and this is not enough to image an artery without any partial volume effect, where other tissue of no interest would be present (Çavuşoğlu et al., 2009). There are two methods of calculating M_{0a} from a measurement of M_0 in tissue. The first one, and the one used in this work, uses the average CSF M_0 . The second one uses the voxelwise M_0 values from each tissue. In order to convert the tissue M_0 values into M_{0a} , the respective water partition coefficient of tissue-to-blood is used.

Because the PASL sequence used here employs double in-plane pre-saturation pulses to saturate all the molecules before the labelling takes place, an M_0 image can be estimated from the saturation-recovery curve of the ASL control images. Otherwise, we would need to acquire an additional M_0 image.

Using Saturation Recovery, the signal from the calibration image (ASL control image) can be expressed by the Equation 2.4 where $M(t)$ is the signal measured of the calibration image in the tissue of reference, in this case CSF, and M_{0t} is the equilibrium magnetization of that tissue. By inverting the following equation it was possible to recover M_{0t} . The tissue used in this analysis was the CSF because it is the tissue of the brain with the closest resemblance to blood in terms of number of water molecules:

$$M(t) = M_{0t}(1 - Ae^{\frac{-t}{T_{1t}}}) \quad (2.4)$$

where T_{1t} is the tissue time constant and A is a constant describing the pre-saturation efficiency, assumed to be 0.9. Then, M_{0a} can be estimated using the Equation 2.5:

$$M_{0a} = \lambda M_{0t} e^{TE(\frac{1}{T_{2t}^*} - \frac{1}{T_{2a}^*})} \quad (2.5)$$

where λ is the water partition coefficient of tissue-to-blood, where for the CSF is 0.87 (Herscovitch & Raichle, 1985), TE is the echo time of the sequence, T_{2t}^* and T_{2a}^* are the tissue of reference and arterial T_2^* , respectively. With M_{0a} calculated, it is then possible to obtain the absolute values of the parameters of interest. An example of the M_{0t} and M_{0a} is presented in Figure 2.7.

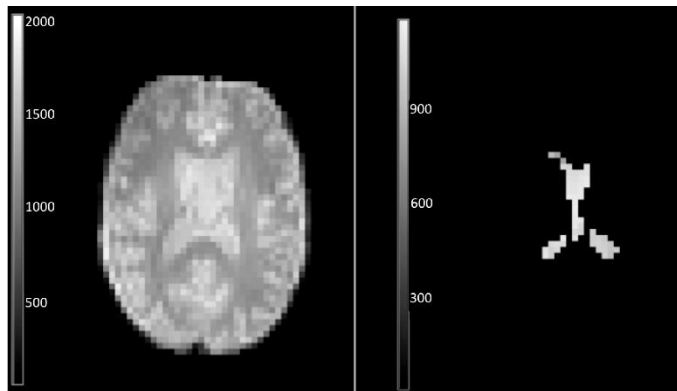


Figure 2.7 – An example of M_{0t} (left) and M_{0a} estimated in a mask of CSF (right).

In this work, this calibration process was done using the following tools. Initially it was necessary to obtain a CSF mask so that it could be used in the calibration image, which was done using several tools like FSL FAST tool, FLIRT tool, among other FSL command line tools. Then FSL FABBER tool (Chappell et al., 2009; Groves et al., 2009; Woolrich et al., 2006) was used to estimate the mean M_{0t} of CSF tissue, so that, through the FSL *fslmaths* command line tool, the M_{0a} could be estimated for further use in the analysis.

2.2.2 Parameter estimation

Now that all the pre-processing steps have been taken, the next stage is the actual model fitting to estimate the parameter maps, using a set of parameter priors. These aspects will be presented in the following sections as well as some additional options that were taken into the model fitting and the definition of the regions of interest used in this work.

2.2.2.1 Parameter priors

Before estimating the parameter values, it was important to define what priors would be used. These priors were chosen according to the prior knowledge about the range of values that the parameters might be likely to take. A list of the free parameters in the model, and the respective prior distribution mean and standard deviation (SD) values used in this work (see below), are presented in Table 2.1, following (Chappell et al., 2010; Chappell et al. , 2013) .

Table 2.1 – Prior distribution mean and standard deviation values for the parameters of the General Kinetic Model.

Parameter		Mean	Standard deviation
f	(ml/g/s)	0	10^3
Δt	(s)	0.7	0.3
aBV	(%)	0	ARD
τ	(s)	0.75	0.3
T_1	(s)	1.3	0.1
T_{1a}	(s)	1.6	0.1
Δt_a	(s)	0.5	0.3
τ_a	(s)	0.75	0.3

For CBF, a non-informative prior value was chosen, not having any prior assumptions about its value. More restrictive priors were chosen for the parameters, T_1 and T_{1a} , due to the certainty in the knowledge of their physiological values (Chappell et al., 2010).

Since the acquisition sequence used was Q2TIPS, the prior of the tissue and arterial bolus duration were also quite restrictive, and their means fixed at this value. This was very useful as the actual time needed for the bolus to reach the imaging region and the velocity of the labelled molecules was not known.

The Δt_a prior mean value was set to 70% of the BAT (Δt) value, because this way there was some flexibility on the value while avoiding that it was introduced as an additional free parameter (Ho et al., 2011).

In most of the voxels there is no macro-vascular component in the signal, thus the fitting of three more parameters in tissue-only voxels might cause overfitting and consequently originating noise from artificial macro-vascular signal. So what was done was to use an automatic relevance determination (ARD) prior (Chappell et al., 2009) for the macro-vascular parameter

(aBV). The mean of this parameter was set to zero but the variance was specified as a further parameter to be determined from the data (Chappell et al., 2010). This allows for a compensation task, i.e., in the case of the variance having a large value estimated, then the aBV prior is considered non-informative, as it is free to take a wide range of values. On the other hand, if the variance shrinks, the prior becomes more informative until it reaches the mean of the ARD prior, zero. This method is very useful as it removes the macro-vascular component when not needed leaving only those voxels that really have this component. This allows the reduction of the model complexity from the data.

According to one of the goals of this work, different prior distributions were tested, particularly for the BAT parameter (Δt) since we wished to allow sufficient flexibility to permit the estimation of BAT changes during hypocapnia. For this purpose, the following BAT distribution mean and SD values were tested: 0.6, 0.7 and 0.8 s and 0.1, 0.3 (default), 0.5, 1 and 10^4 s, respectively.

2.2.2.2 Model fitting

With the priors defined, the model fitting could, finally, be done. This step was performed using the FSL command line tool *oxford_asl* from the BASIL toolbox. Besides the values of the priors wanted, this function also received the M_{0a} value from calibration, the magnetization difference corrected and some additional features that are going to be explored in the next section. In the end of this stage, the parameter maps were estimated and the transformation matrices previously saved were used to obtain these maps in both the structural and standard spaces. In Figure 2.8, it is showed an example of how the estimated parameter maps look like.

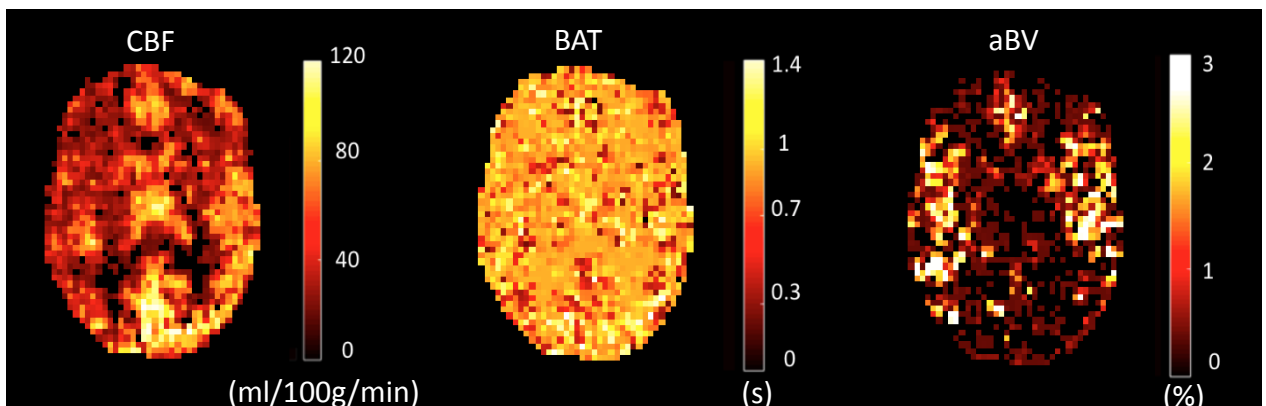


Figure 2.8 – Example of CBF (left), BAT (middle) and aBV (right) maps for a representative subject.

Additional features were used in the model fitting in order to have a better estimation of the parameters. Some were acquisition specific features, whereas others were analysis options.

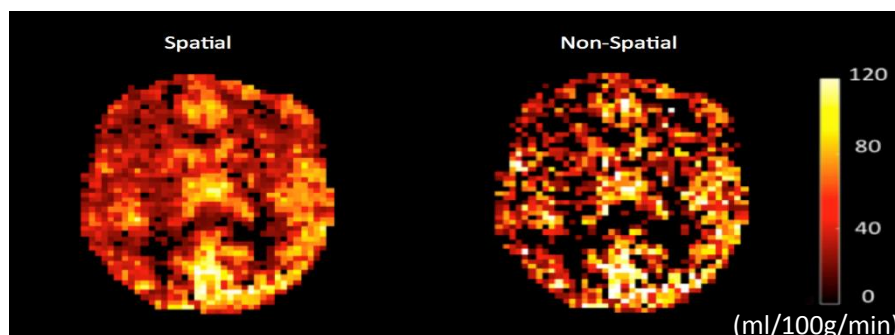
One acquisition specific feature used was the called *fixbolus*. This feature disabled the automatic estimation of the bolus duration, as this was well defined by the acquisition sequence

Q2TIPS, and this way it was one parameter less to estimate (two if considering the arterial bolus duration).

Another feature was the enabling of the correction of the macro-vascular component, for signal arising from arterial blood destined to further regions (Chappell et al., 2010).

The other acquisition specific feature used was the *slicedit*, which was very useful for multi-slice acquisitions where a superior slice is acquired later than those below since it accounts for the increase in time after labelling for a superior slice when compared to the one below. The value used was 0.045 s.

The final feature used was the *spatial*/prior (Groves et al., 2009) that uses adaptive spatial smoothness priors with a Gaussian kernel. It is directed only to the CBF image and is more or less similar to spatial smoothing the raw data. However, it is adaptive and it does not interact negatively with the model fitting. This feature is an exciting alternative to using standard generalized linear model (GLM) on pre-smoothed data, as well as allowing the introduction of biophysical prior information in a principled manner. It applies adaptive spatial regularization and ensures that the fixation of biophysical prior is properly applied to each voxel, i.e., in each voxel the CBF value is defined considering the neighbouring values, with a prior distribution. This way, there is a reduction of the spatially correlated noise which means that the data in a single voxel is more reliable when using voxel-wise methods. The main drawback of this approach is the blurring of the signal of interest, i.e., fine detail of a determined signal may be lost when applying the spatial prior. This is particularly relevant when the goal of the study is to analyse specific changes in certain anatomical regions and due to the spatial regularization, these changes may be lost. In Figure 2.9 a comparison of a CBF image with and without the spatial prior.



Therefore, this *spatial* prior was itself subjected to study in this work, where results with and without the spatial prior were saved for further comparison.

2.2.3 Definition of regions of interest

With the parameter maps estimated, the next step was the definition of some regions of interest (ROIs) so that the mean values of the parameters could be assessed for further comparison between the two main conditions, REST and PDB.

Whenever model fitting was not successful and hence unable to estimate the parameters correctly, the voxels were labelled as bad fitting voxels. These were identified based on the values of $CBF = 0$ and $BAT = 0.7$, which were the default (prior mean) values for these parameters. In order to avoid biasing the results towards the priors in the case of bad fitting, a mask of these bad fitting voxels was created in order to remove them from the parameter maps.

Then, three different regions of interest (ROI's) were created for the analysis of the parameters' values. The first one was a grey matter (GM) mask as the main focus of normal studies involving ASL MRI is this tissue. This mask was created from a MNI structural atlas (Collins et al., 1995; Mazziotta et al., 2001) where 9 different anatomical cortical structural regions are present (Figure 2.10). This mask was also divided in 9 separate masks of each structural region in order to analyse the 9 regions separately further in the results.

The second ROI created was the *Tissue mask*. This mask was based on the previous one with an extra threshold. The 40th percentile of the REST CBF map of each subject was calculated and this value was used to threshold this same map within the GM mask in order to create the tissue mask. This mask was later used on both CBF and BAT maps of REST and PDB conditions.

The *Vascular mask* was the third ROI created. This mask was also based on the GM mask with an extra threshold. It was obtained by thresholding the REST aBV map above 10% of the mean for each subject, within the GM mask. This mask was then applied to the aBV maps of REST and PDB conditions.

The aBV maps had a particular characteristic. This parameter is the fraction of arterial blood present in a specific voxel and in theory in PDB there is a vasoconstriction that reduces the volume occupied by these vessels. Therefore, some voxels that in REST condition had aBV values different from zero, in PDB could now lead to $aBV = 0$, due to vasoconstriction, which is relevant when considering average values. Consequently, in order to avoid this biasing of the

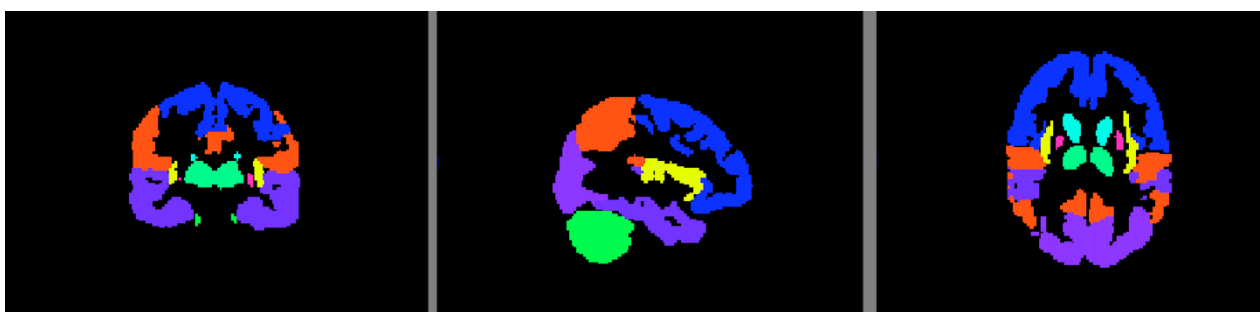


Figure 2.10 – Example of the MNI structural atlas. The different colours represent the 9 regions (left to right: sagittal, coronal and axial).

mean values, only voxels in REST condition with $aBV \neq 0$ would be taken into account in the PDB condition, in order to have a direct comparison between the two conditions. This means that in REST the mean aBV was estimated without voxels with zero values, while in PDB the mean aBV was calculated with voxels with zero values but in the mask where the aBV voxels from REST were different from zero.

All these masks were created with several tools, but mainly the FSL *fslmaths* command line tool and FLIRT tool. The parameters' mean values were then estimated within these three masks and used for comparisons between the two conditions of this work.

2.3 Baseline vs hypcapnia comparison

With the parameters' maps estimated and the mean values calculated, it was then possible to compare the baseline (REST) and hypcapnia (PDB) conditions. In the following sections, some approaches of group statistical analysis that were used for this matter are going to be described.

The parameters' mean values of all subjects analysed were grouped together according to the parameter at question and the condition. This was done so that a group analysis could be done in order to compare the behaviour of the parameters from one condition to another.

The parameters' mean values of all subjects were averaged in order to produce a group mean CBF, BAT and aBV . This was done for both REST and PDB condition. The mean displacement results of the motion correction analysis and the number of bad fitting voxels were also subjected to the same group analysis procedures.

First, a group analysis was performed to study the importance of the BAT prior. Then, another group analysis was done in order to study the relevance of the *spatial* prior.

After this, it was possible to do a group analysis with optimal characteristics to compare the REST and PDB conditions. This was done at different levels: 1) voxelwise across the whole brain (using randomise, a FSL tool for nonparametric permutation inference on neuroimaging data); 2) for each of the three ROI's defined in this work; and 3) in the 9 anatomical regions of the MNI atlas. Simple paired t-tests with equal variances ($p < 0.05$) that were applied to determine if the two conditions had a significant difference. This was used for the parameters' mean values, as well as the mean displacement and the number of bad fitting voxels.

Moreover, for the parameters' mean values a correlation test with $P_{ET}CO_2$ data was performed. More specifically, the correlation was done between parameters' mean values difference of the two conditions with the difference $P_{ET}CO_2$ of also the two conditions ($\Delta P_{ET}CO_2$), i.e., $Parameter_{REST} - Parameter_{PDB}$ with $P_{ET}CO_{2REST} - P_{ET}CO_{2PDB}$. This correlation is particularly interesting as the amount of hypcapnia that each subject reaches, quantified by $\Delta P_{ET}CO_2$, might

not be the same. Thus, with this correlation it is possible to see if the parameters behave accordingly with the amount of hypocapnia reached.

For the voxelwise analysis, intended to see if the maps of both conditions were significantly different, the FSL Randomise tool (Nichols & Holmes, 2002; Winkler et al., 2014) was used with the help of the FSL GLM general advice tool. In this approach two techniques were used to obtain the results. The first one is the voxel-wise technique that compares both conditions maps voxel to voxel. The second technique was the Threshold-Free Cluster Enhancement (TFCE) (Smith & Nichols, 2009). This is a new method for finding clusters in the data without having to define the clusters. It takes the image at hand and outputs an image in which the voxel values represent the amount of cluster-like local spatial support. Basically, the image remains fundamentally voxel-wise but the cluster structures enhance. The normal cluster based techniques are more sensitive than the voxel-wise techniques but require the definition of the initial cluster-forming threshold, which has a large impact on the results, especially when using low cluster-forming thresholds, however this is arbitrary. TFCE keeps the sensitivity and minimizes these problems, so, theoretically this technique is the best one. With both techniques, corrected and uncorrected results were saved for further analysis, in the three ROI's used in this work.

3 Results and Discussion

The following chapter describes the main results obtained in this work using the materials and methods presented in the previous chapter. This chapter is organized in four main sections. In the first two sections, the partial pressure of end-tidal carbon dioxide ($P_{ET}CO_2$) and the head movement results are presented. In Section 3.3 the results of the perfusion parameters estimation are described. Then, the results of the group analysis of the two conditions, baseline and hypocapnia, are presented in the Section 3.4, as well as an analysis of the number of bad fitting voxels and the statistical analysis made. In order to avoid increasing the length of this chapter, some results are shown in the Appendix section.

3.1 End-tidal carbon dioxide pressure

The first results to be analysed were the end-tidal carbon dioxide pressure ($P_{ET}CO_2$). In Figure 3.1 and 3.2, the time courses obtained for the subjects that were monitored with the capnograph are presented, in both conditions REST and PDB. The mean $P_{ET}CO_2$ values obtained for each condition are presented in Table 3.1, along with the values for the $P_{ET}CO_2$ difference, $\Delta P_{ET}CO_2$ (REST – PDB). The subjects where the acquisition was performed with the CO₂ monitor (S6, S7, S8 and S9) are also presented in Table 3.1.

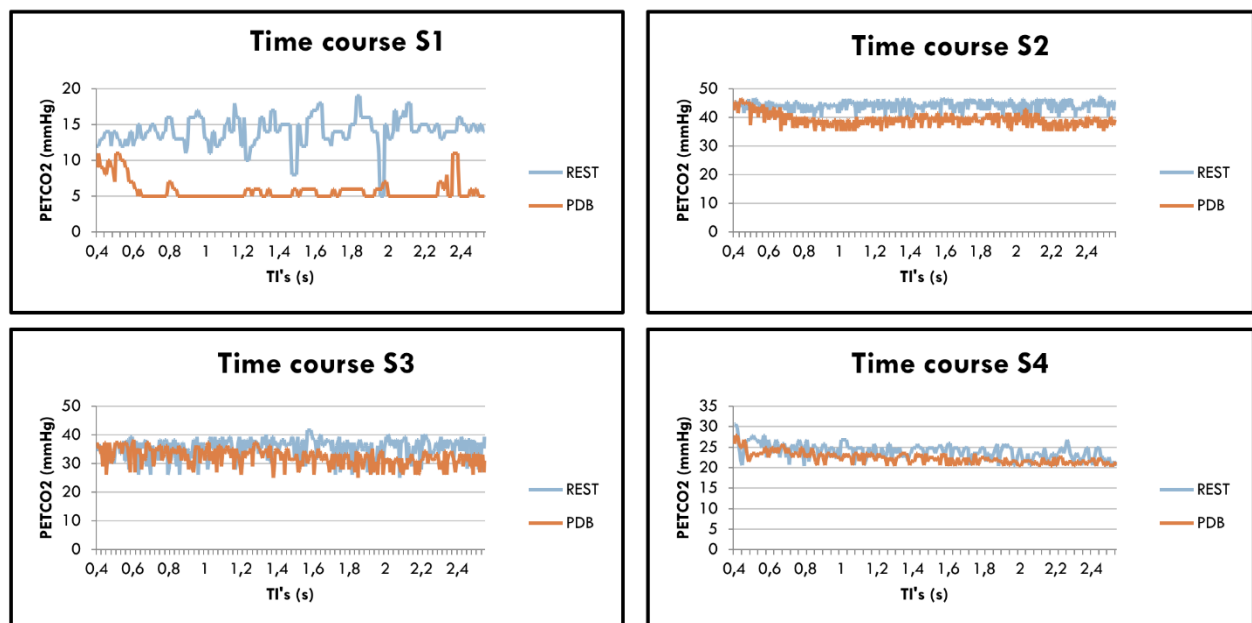


Figure 3.1 – $P_{ET}CO_2$ time courses for the subjects S1, S2, S3 and S4.

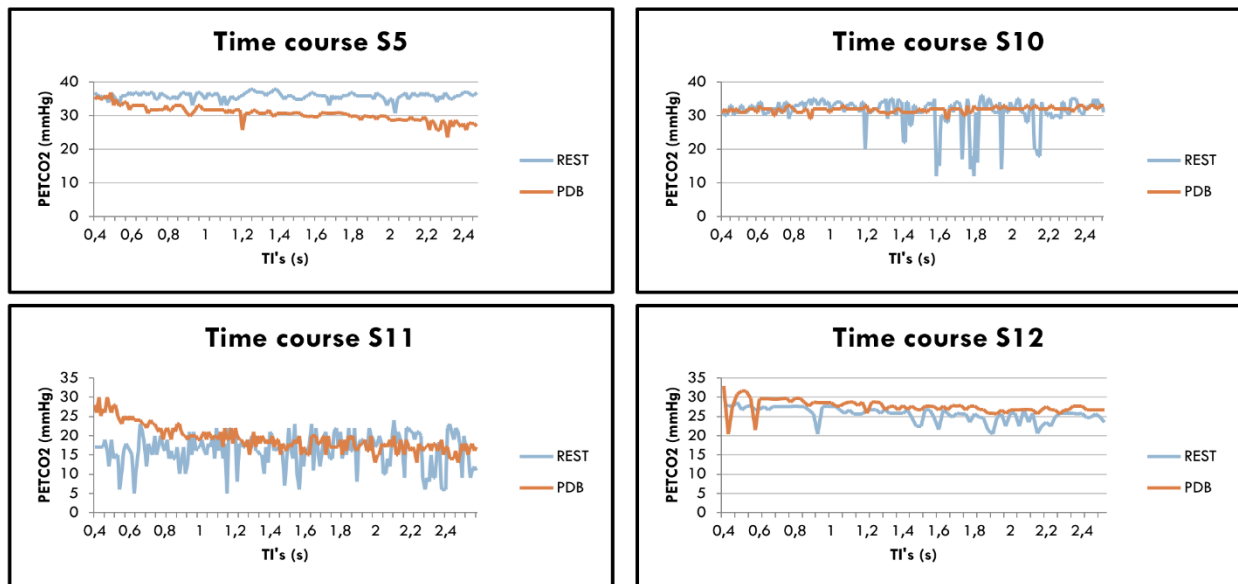


Figure 3.2 – $P_{ET}CO_2$ time courses for the subjects S5, S10, S11 and S12.

It is interesting to see that in some subjects (S1, S2 and S5) there is a delay in the $P_{ET}CO_2$ reduction during the PDB condition, i.e., hypocapnia takes a while to develop. Significant differences between the $P_{ET}CO_2$ time courses during REST and PDB were observed in subjects S1, S2, S3, S4 and S5.

Table 3.1 – $P_{ET}CO_2$ values in mmHg acquired in REST and PDB conditions, for every subject, also with the difference values. * denotes significant differences ($p<0.05$)

Subjects	$P_{ET}CO_2$ (mmHg)		Difference
	REST	PDB	
S1	14.05	6.08	7.97 *
S2	22.28	20.64	1.64 *
S3	21.53	16.95	4.58 *
S4	13.59	11.73	1.86 *
S5	18.20	15.47	2.73 *
S6			8.00
S7			3.80
S8			3.00
S9			2.70
S10	31.42	31.81	-0.40
S11	16.31	19.20	-2.88
S12	12.67	13.12	-0.45
Mean \pm standard deviation	18.76 ± 6.2	16.88 ± 7.6	2.71 ± 3.2

The results show that, in general, there is a decrease of $P_{ET}CO_2$ from the REST condition to PDB, as expected. However, in subjects S10, S11 and S12 this decrease is not present (there is actually an increase in $P_{ET}CO_2$), which indicates that these subjects did not achieve hypocapnia when executing the task. Therefore, these subjects were discarded from this work, since the ASL MRI data from the PDB condition did not correspond to a subject performing hypocapnia. Figure 3.3 shows the bar charts of the $P_{ET}CO_2$ values in REST and PDB for the subjects that had the $P_{ET}CO_2$ values from the REST and PDB recorded and actually performed hypocapnia.

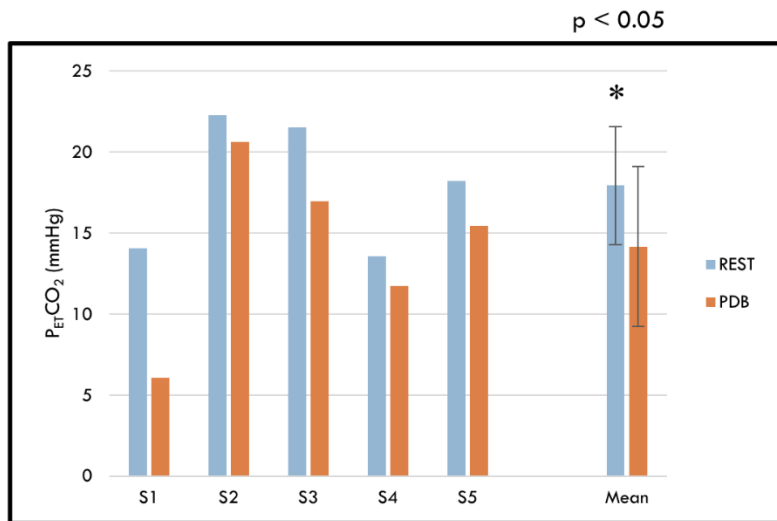


Figure 3.3 – $P_{ET}CO_2$ values bar charts for the subjects that performed hypocapnia and the mean value. Error bars represent the standard deviation of the mean and * denotes significant differences ($p<0.05$).

For the subjects presented in Figure 3.3 it is possible to see that significant differences (paired t-test with equal variances, $p < 0.05$) were found between REST and PDB condition. Another aspect worth mentioning is that $P_{ET}CO_2$ values vary across subjects, as seen in Figure 3.3, which may be due to different respiratory activity across subjects and/or to differences in the calibration of the CO₂ measurement setup. In any case, in this work, as long as a decrease from REST to PDB is present, this should not make a difference. The subjects used for the rest of the analysis of this work were S1, S2, S3, S4, S5, S6, S7, S8 and S9.

3.2 Head movement

In this section, the results of mean displacement of head movement in subjects, in both conditions, are presented. The volumes of each ASL acquisition time series were re-aligned yielding the mean displacement values for each subject, both absolute and relative (Figure 3.4).

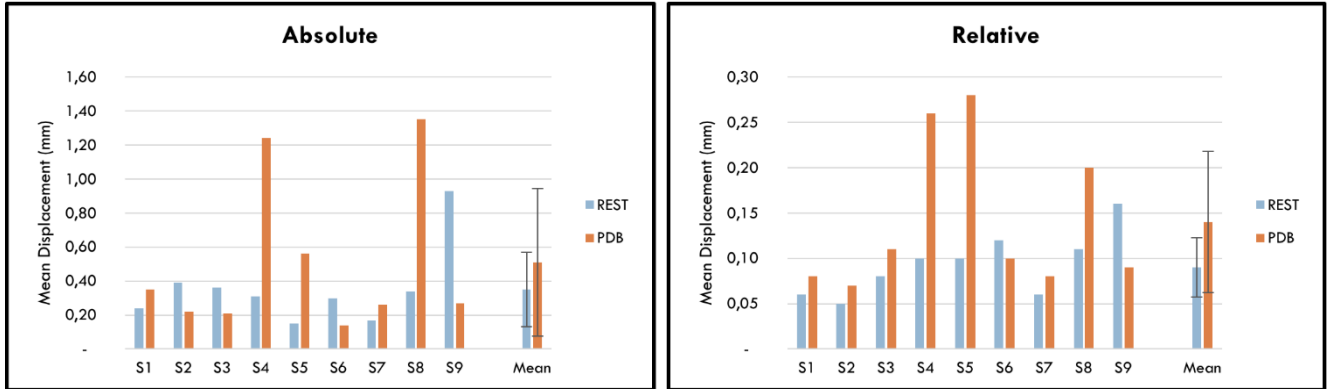


Figure 3.4 – Mean displacement in mm bar charts for the subjects analysed, with absolute values (left) and relative values (right). Error bars represent the standard deviation of the mean.

From these results, it is clear that, in general, the acquisitions made in PDB condition have more head movement than the acquisitions in REST condition. This is interesting as it shows that maybe there is some effort made by the subject when performing the PDB task, which causes the subject to move more than normally. Nevertheless, no significant differences were found (paired t-test with equal variances, $p < 0.05$) between REST and PDB conditions, both in absolute and relative displacement. However, for the relative case a p-value of 0.078 was reached which is not that far from significant difference.

Another important aspect is that there are some subjects that have very high mean displacement in a determined condition even when compared with other subjects, like S4, S5 and S8, that have much higher movement in the PDB condition and subject S9 that has this increase in the REST condition. The mean displacement time courses for these subjects is presented in Figure 3.5 and there it is possible to see that, for these subjects, this increase in the mean displacement in a specific condition is localised, i.e., it is not a general head movement along the entire acquisition. Therefore, one option was to remove the volumes that corresponded to this local movement, however, it required many volumes to which without them the model fitting would be ruined. Another option was to remove these subjects from the analysis but since there were already few subjects that would lead to a less significant group analysis. The time courses for the rest of the subjects are presented in the Appendix section. Therefore, we opted to keep all subjects in the analysis regardless of substantial head motion.

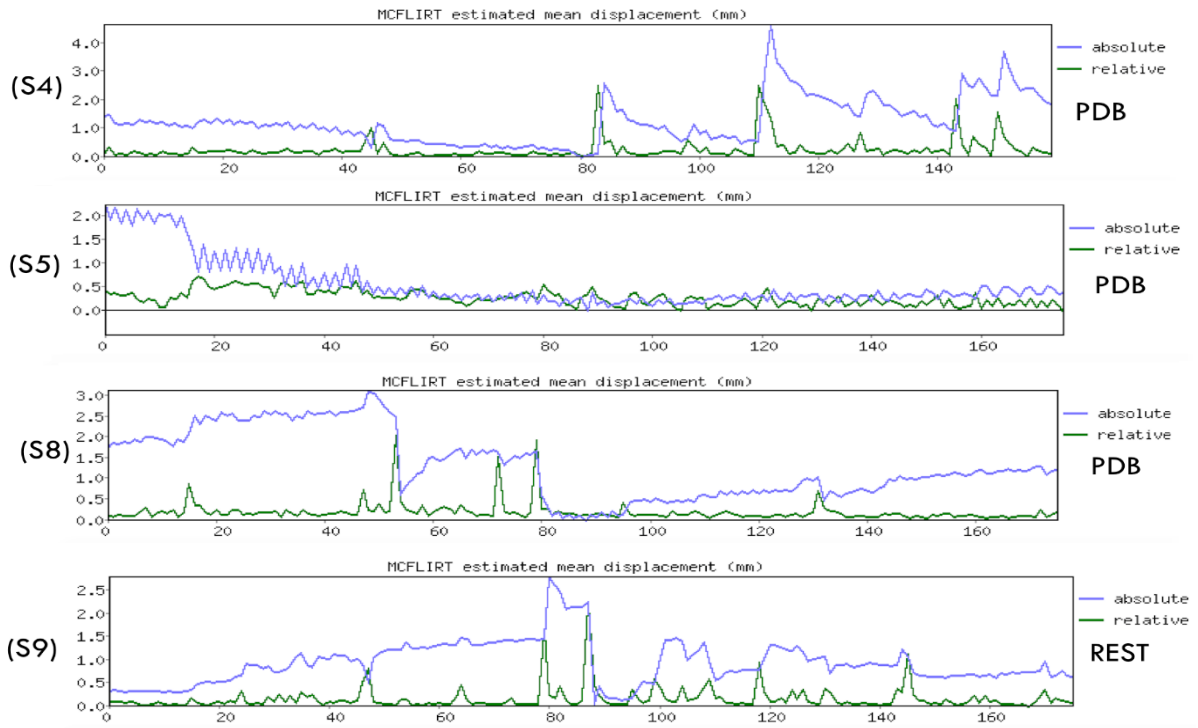


Figure 3.5 – The mean displacement time courses for subjects S4, S5, S8 and S9, in the respective problematic condition.

3.3 Parameters' prior distribution

In the following sections, the results for the changes made in the parameters' priors are presented. As mentioned in the previous chapter the BAT prior was altered from the default values in order to see the importance of this prior and the optimized values for it. Then some analyses in the model fitting were made by obtaining the parameters' estimation with and without *spatial* prior to see the main differences and whether or not this option should be used in this work.

3.3.1 BAT prior

As mentioned in Section 2.3.1 the main modifications to the BAT prior were in the mean where 0.6 s, 0.7 s (default) and 0.8 s were tested and in the standard deviation of the mean where 0.1 s, 0.3 s (default), 0.5 s, 1 s and 10^4 s were examined. Since the goal of this analysis was to check what the optimized values were for the BAT prior, only the acquisitions from REST condition were analysed, for simplicity reasons. In Figure 3.6 the three parameters' estimations for each combination of mean and standard deviation of BAT prior used are presented. The values presented in that table represent the parameters values averaged for all subject in REST condition within each combination of BAT prior, where the average was performed in the GM ROI mask without the *spatial* prior and in the functional (native) space.

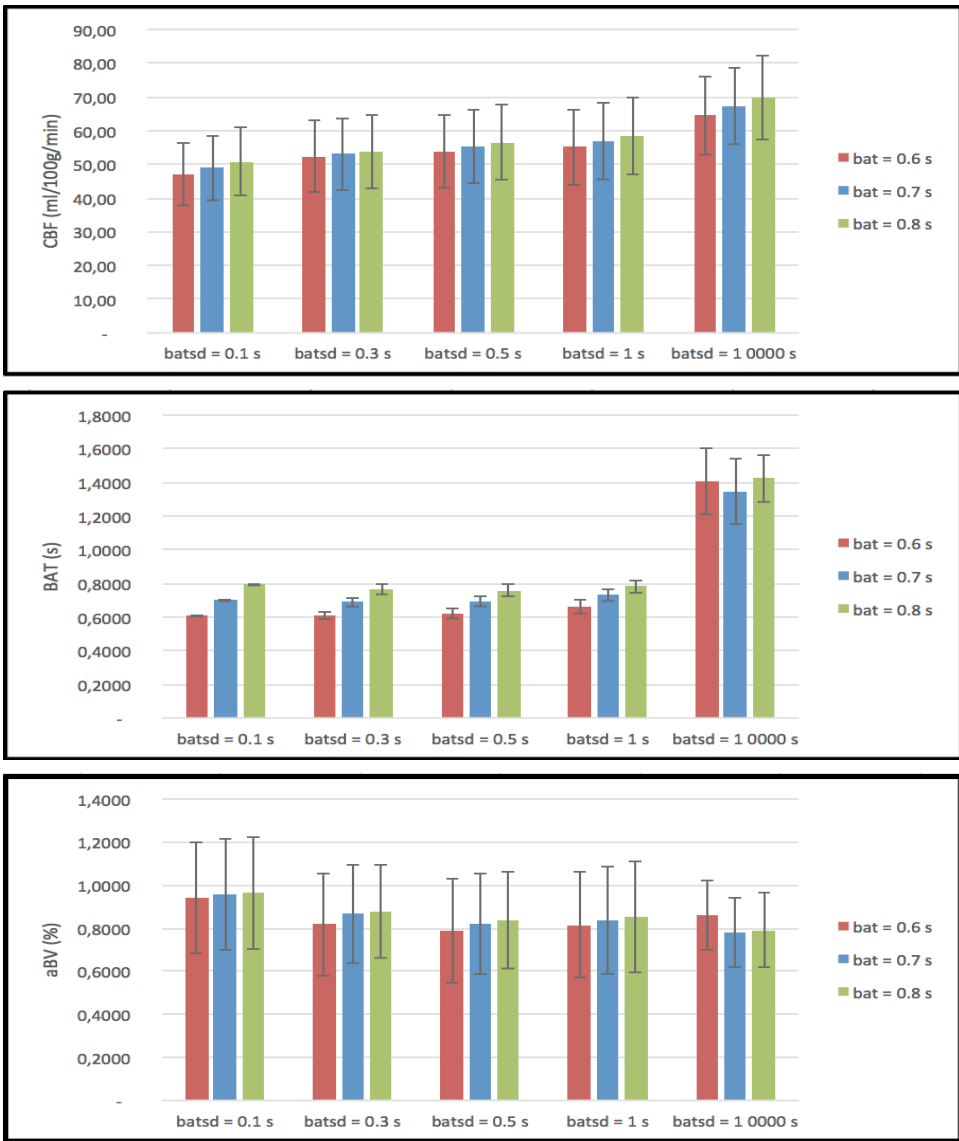


Figure 3.6 – Bar charts for CBF (top), BAT (middle) and aBV (bottom) values for each combination of BAT prior. Error bars represent the standard deviation of the mean values.

Several aspects can be concluded from Figure 3.6. The increase in the standard deviation of the BAT prior (*batsd*) causes an increase in CBF possibly due to a growth of deceiving fitting voxels that have wrong estimates. For the aBV parameter the opposite effect is verified. With this *batsd* increase, the BAT parameter suffers a general increase caused by the direct expansion of the standard deviation of the prior, which allows a greater range of estimate values. However, the same effect of wrong fitting voxels is also observed more intensively in this parameter as it is perceived when *batsd* = 10⁴ s, i.e., by removing the BAT prior information. In Figure 3.7 an example slice of subject S2 for the three parameters and for bat = 0.7 s is presented. Figure 3.8 shows the number of bad fitting voxels averaged for all subjects in each combination of BAT prior mean and standard deviation.

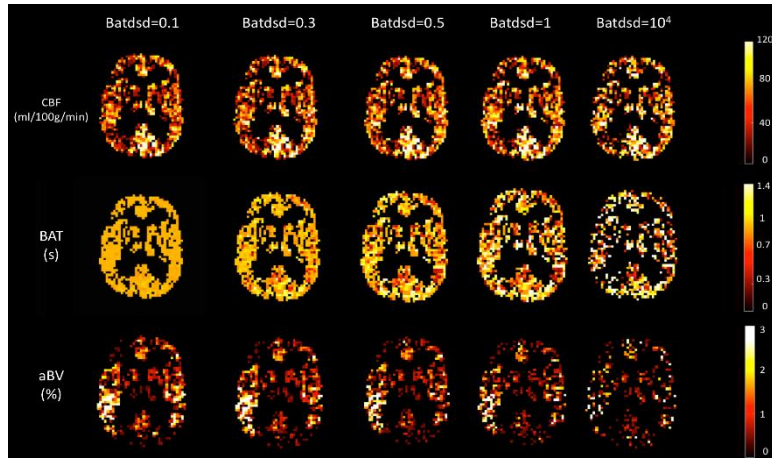


Figure 3.7 – Example slice of the estimated parameters' maps for subject S2 with BAT prior mean equal to 0.7 s and for each *batsd*.

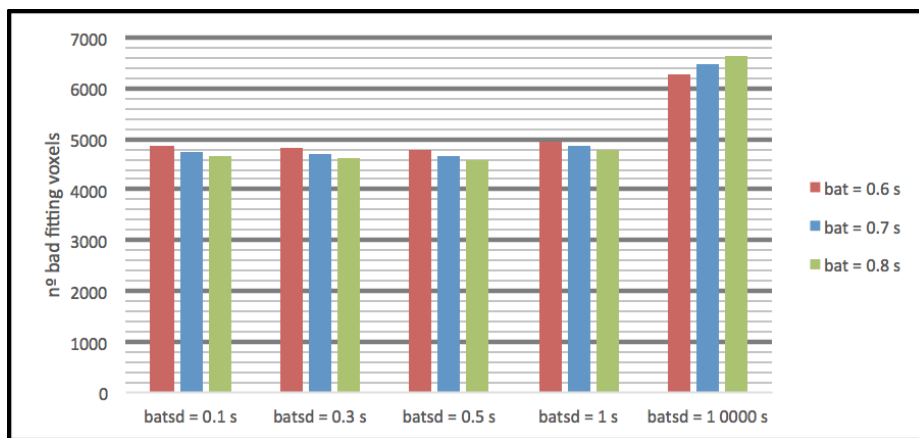


Figure 3.8 – Number of bad fitting voxels averaged for all subjects in each combination of BAT prior.

From Figure 3.7 it is possible to see those effects mentioned before. With the increase of *batsd* there is an increase of wrong fitting voxels in CBF and BAT, therefore an increase in the mean values and a decrease of intensity in aBV map is observed. The greater the *batsd* the greater the number of bad fitting voxels, as it is clear from Figure 3.8, which could also explain the increase in the mean values of CBF and BAT since these voxels were removed from the averaging.

With these results it was decided, for the next analyses, to use *bat* = 0.7 s and *batsd* = 0.5 s. The mean of BAT prior (*bat*) values of 0.6 s and 0.8 s were only tested to see if the behaviour of the parameters was the same, as it is more or less clear from the literature that the default value should remain 0.7 s. The *batsd* = 0.5 s was decided because it allows a greater range of estimation values for BAT while maintaining a less number of bad fitting voxels compared with greater *batsd* values.

3.3.2 Spatial prior

The next step in this work was to decide whether or not, to use the *spatial* prior for the model fitting. Then, for the subjects analysed two estimations were made for each parameter of interest with and without the *spatial* prior. In Figure 3.9 these results are shown, where the values are presented in the form of bar charts. In addition, for simplicity reasons, only the REST condition data for each subject was used in this analysis, since the goal was to compare the results with and without the *spatial* prior. These estimated values shown were calculated for the GM ROI mask and in the functional space.

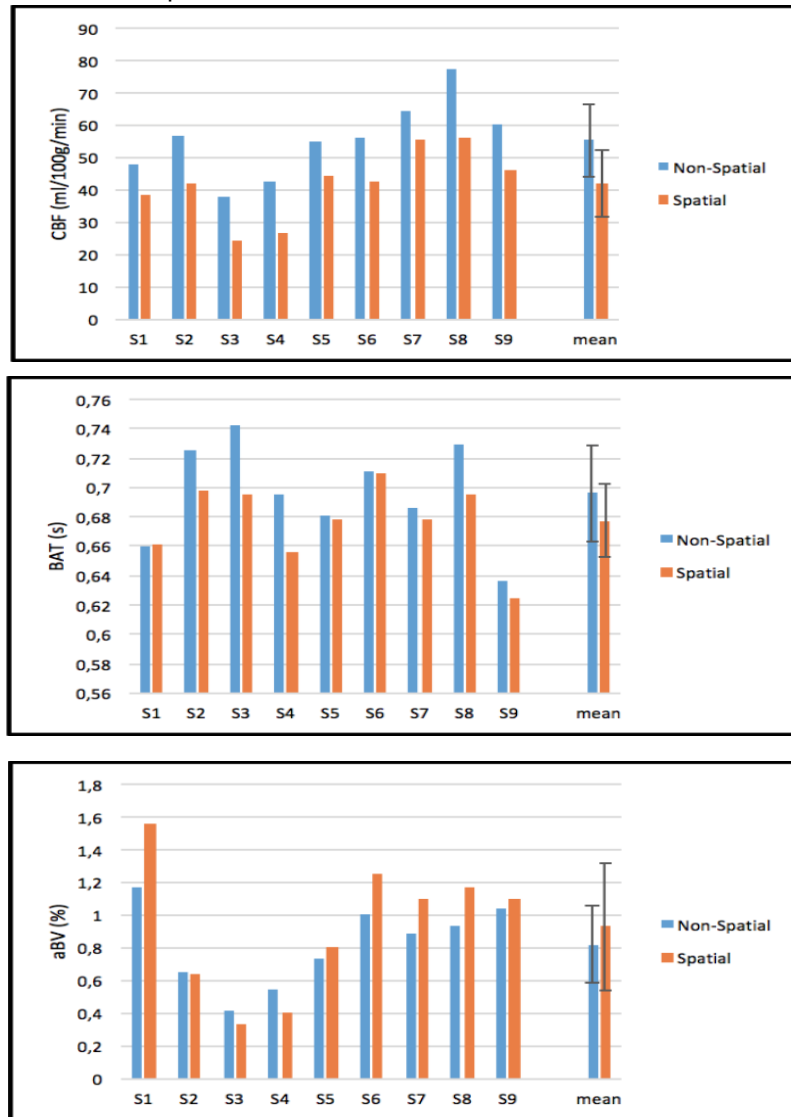


Figure 3.9 – Bar charts for CBF (top), BAT (middle) and aBV (bottom) estimated in all subjects, with and without the *spatial* prior, also with subjects' mean. Error bars represent the standard deviation of the mean values.

The main conclusion for the CBF parameter is that using *spatial* prior decreases the mean value estimated as expected considering that through the spatial prior neighbouring voxels are contemplated, which reduces the value of certain voxels. Theoretically, the *spatial* prior should only affect the CBF parameter, however, from Figure 3.9 it is possible to see that there is a decrease in BAT and an increase in aBV when using the *spatial* prior. The behaviour of these two

parameters is mainly due to a decrease in the number of bad fitting voxels, which are excluded from the averaging process, when using the *spatial* prior. This happens because, in this case, the CBF map has less voxels with zero intensity, which result in less bad fitting voxels. Therefore, the actual GM ROI mask used is different in the two options, but it would not be correct to consider only the bad fitting voxels in some cases. In the next section, these differences in the number of bad fitting voxels will be explored. In Figure 3.10 the maps for the three parameters with and without *spatial* prior is shown for subject S2 in a specific slice.

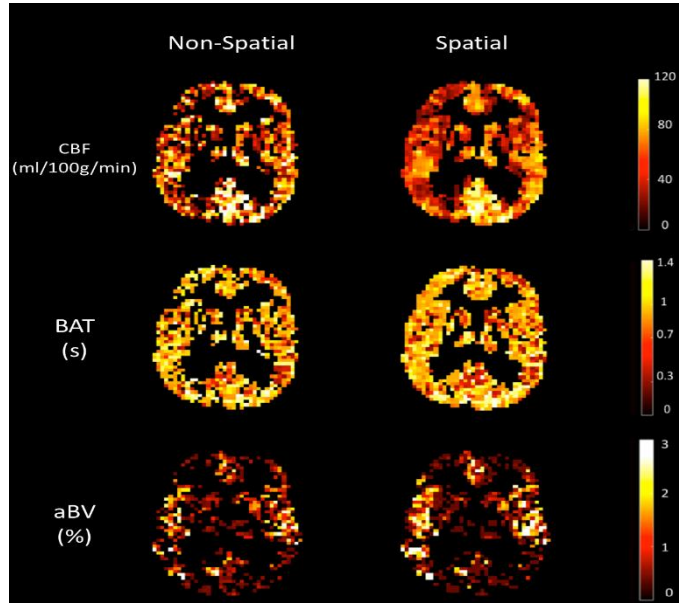


Figure 3.10 – CBF, BAT and aBV maps for subject S2 with and without *spatial* prior.

In the Figure above, it is clear the difference in the CBF map from the two options. In the BAT and aBV maps, this difference is less obvious but there is also a significant difference in terms of quantity of voxels with intensity. The benefits of using the *spatial* prior are that the model fitting produces more accurate estimation overall, however some local resolution is lost, which could be a problem when searching for a specific region in the brain. With the help of the results from the next section, a decision will be made on whether or not to use the *spatial* prior for the rest of this work.

3.4 Baseline vs hypcapnia

To perform the comparison between the two conditions of interest, baseline (REST) and hypcapnia (PDB), the three parameters CBF, BAT and aBV estimated continue to serve as reference through the quantification of changes between these two conditions. In the following sections, the results of an analysis on the number of bad fitting voxels in the two conditions will be presented as well as the group analysis comparing the two conditions with all the regions of

interest used in this work. In the end, the results of the statistical analysis performed will be displayed.

3.4.1 Number of bad fitting voxels

For all subjects and each condition, REST and PDB, the number of bad fitting voxels was assessed as well as the difference from PDB to REST. This was done both with and without the *spatial* prior. These results are shown in Table 3.2 and in Figure 3.11 in the form of bar charts.

Table 3.2 – Number of bad fitting voxels for all subjects with and without the spatial prior and in REST and PDB condition. The difference value (PDB – REST) is also depicted.

Subjects	Non-Spatial			Spatial		
	Nº Bad Fitting voxels		Difference	Nº Bad Fitting voxels		Difference
	REST	PDB		REST	PDB	
S1	2727	3625	898	88	40	-48
S2	6354	9229	2875	44	289	245
S3	6931	7266	335	24	144	120
S4	8064	6136	-1928	109	347	238
S5	8090	7219	-871	574	101	-473
S6	2396	3990	1594	12	387	375
S7	1738	4152	2414	6	294	288
S8	2779	2548	-231	190	47	-143
S9	2919	3317	398	280	625	345
Mean ± standard deviation	4666 ± 2480	5276 ± 2135	609 ± 1449	147 ± 173	253 ± 180	105 ± 262

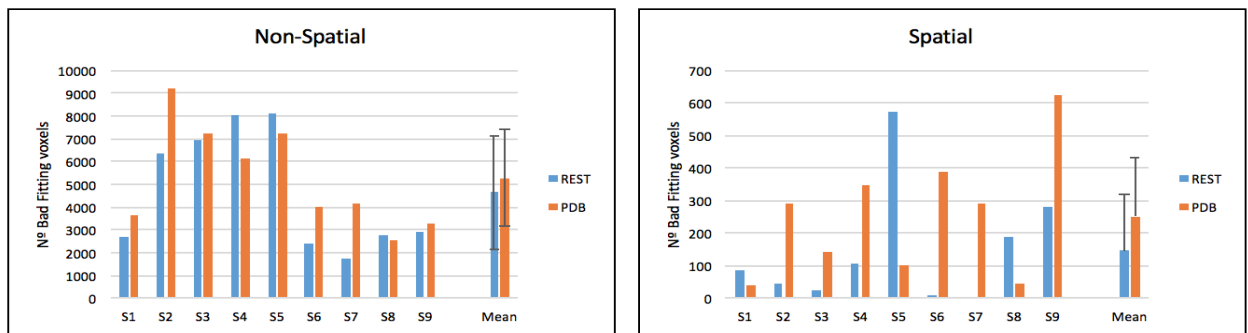


Figure 3.11 – Bar charts of number of bad fitting voxels for all subjects in REST and PDB, with and without the *spatial* prior, and the subjects' mean values. Error bars represent the standard deviation of the mean values.

First aspect to notice is that, as mentioned in the previous section, using the *spatial* prior reduces considerably the number of bad fitting voxels, which is a good thing since this way it is possible to account for almost all the voxels. As this work is not intended to study a specific region of the brain but to see the general behaviour of the brain perfusion to changes of CO₂ for all the analyses remaining in this work the *spatial* prior was used in the model fitting.

For both non-spatial and spatial options, a simple paired t-test with equal variances ($p < 0.05$) was performed to see if there were significant differences between REST and PDB in the matter of number of bad fitting voxels. However, no significant differences were found in both options.

In the non-spatial case, the reason for subjects S2, S3, S4 and S5 having such an increase in bad fitting voxels is because these subjects were the ones for which the acquisition data had 28 slices which consequently had more voxels and therefore led to this increase.

When comparing REST and PDB conditions, in Table 3.2 and Figure 3.11, it is possible to see that for both spatial and non-spatial prior only three subjects have more bad fitting voxels in REST than in PDB (non-spatial: S4, S5 and S8; spatial: S1, S5 and S8). Nevertheless, in general there are more bad fitting voxels in the PDB condition than in REST. This aspect is very interesting as theoretically there is no reason for this to happen. However, one possible answer could be that the FSL BASIL toolbox, used in this work for the model fitting, may have some difficulty when estimating the parameters in PDB condition. Another possible reason for this higher number of bad fitting voxels in PDB is the head movement (mean displacement) that, as seen in section 3.2, is higher in PDB when compared with REST and could cause a higher difficulty in the parameters' estimation.

Despite this interesting result, for each subject only the bad fitting voxels from each condition were considered, as it would not be correct to join the voxels of the two conditions or add in one condition the voxels from the other.

3.4.2 Parameter values and group analysis

In the following sections, the results of the group analyses will be displayed. First, the estimated parameter mean values and maps for the GM ROI mask, then for the Tissue and Vascular ROI masks and finally the results from the Atlas ROI's will be presented. Figure 3.12 presents all the slices for CBF, BAT and aBV for subject S2, in both REST and PDB condition without using any specific mask. In the following sections these maps will be presented for each mask used. The maps for the other subjects are presented in the Appendix section for simplicity reasons.

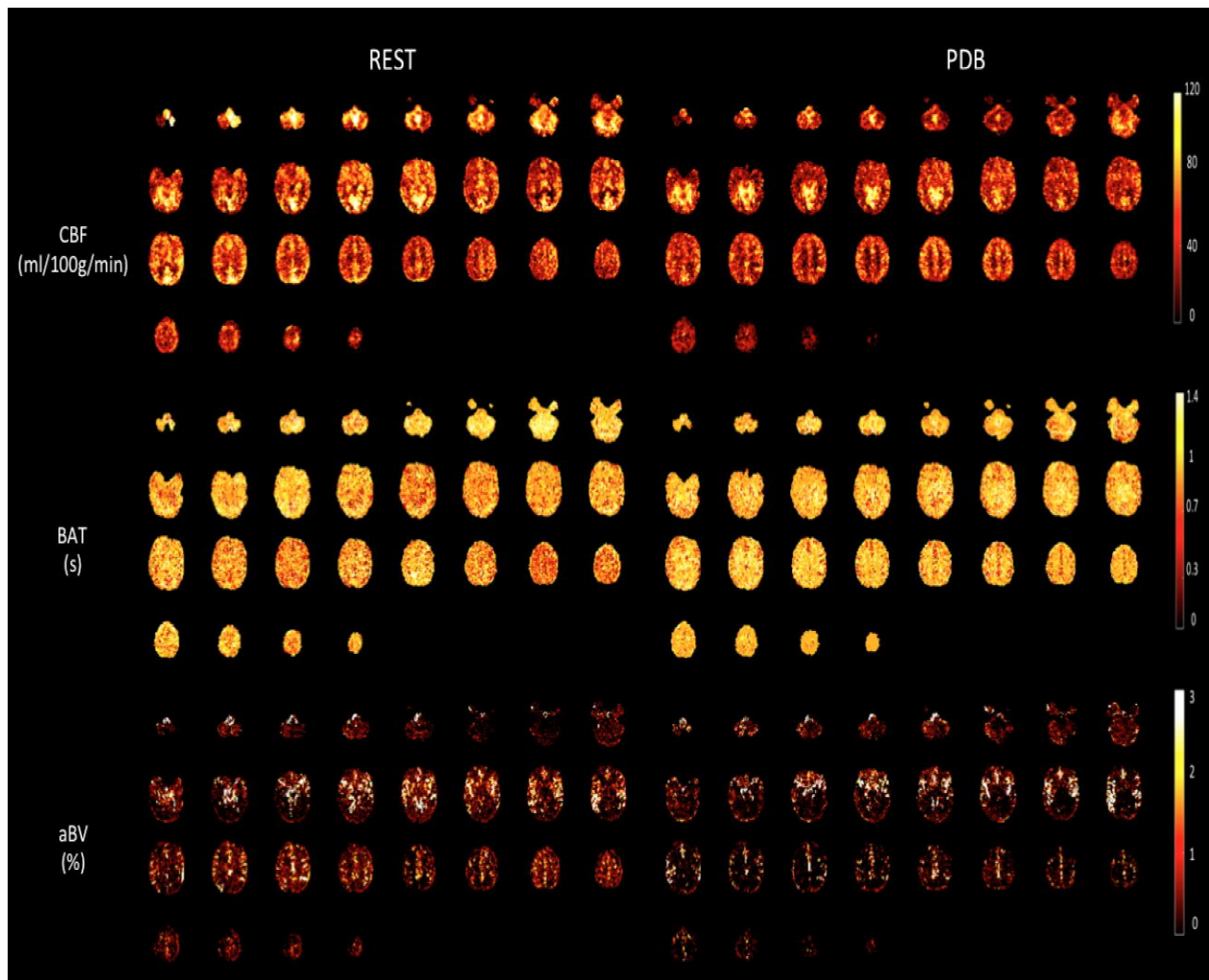


Figure 3.12 – CBF, BAT and aBV maps for subjects S2, in whole brain.

3.4.2.1 Grey matter ROI mask

The comparison between the baseline and hypocapnia condition was done through the study of the three parameters of interest, CBF, BAT and aBV. The model fitting performed estimated these parameters maps for each condition. Therefore, it was possible to obtain the mean values of these maps. These were calculated in the functional space and, in this section, in the Grey Matter ROI mask. Table 3.3 presents these mean values obtained for each subject and each condition as well as Figure 3.13 that plots these results in the form of bar charts. A simple paired t-test with equal variances ($p < 0.05$) was also done between the two conditions.

Table 3.3 – Parameters' maps mean values obtained for every subject in both REST and PDB, using GM ROI mask.

The subjects mean for each parameter is also present.

Subjects	CBF (ml/100g/min)		BAT (s)		aBV (%)	
	REST	PDB	REST	PDB	REST	PDB
S1	38.47	41.74	0.6615	0.7731	1.56	1.24
S2	42.15	32.27	0.6978	0.7321	0.64	0.50
S3	24.57	30.09	0.6957	0.6582	0.33	0.34
S4	26.84	35.68	0.6555	0.6687	0.41	0.24
S5	44.65	51.14	0.6788	0.7164	0.80	0.70
S6	42.86	37.77	0.7098	0.7323	1.25	0.95
S7	55.34	40.95	0.6782	0.7514	1.10	1.33
S8	55.96	54.32	0.6956	0.7451	1.17	1.22
S9	45.88	47.21	0.6251	0.6487	1.10	1.25
Mean \pm standard deviation	41.86 \pm 10.2	41.24 \pm 7.8	0.6776 \pm 0.02	0.7140 \pm 0.04	0.93 \pm 0.4	0.86 \pm 0.4

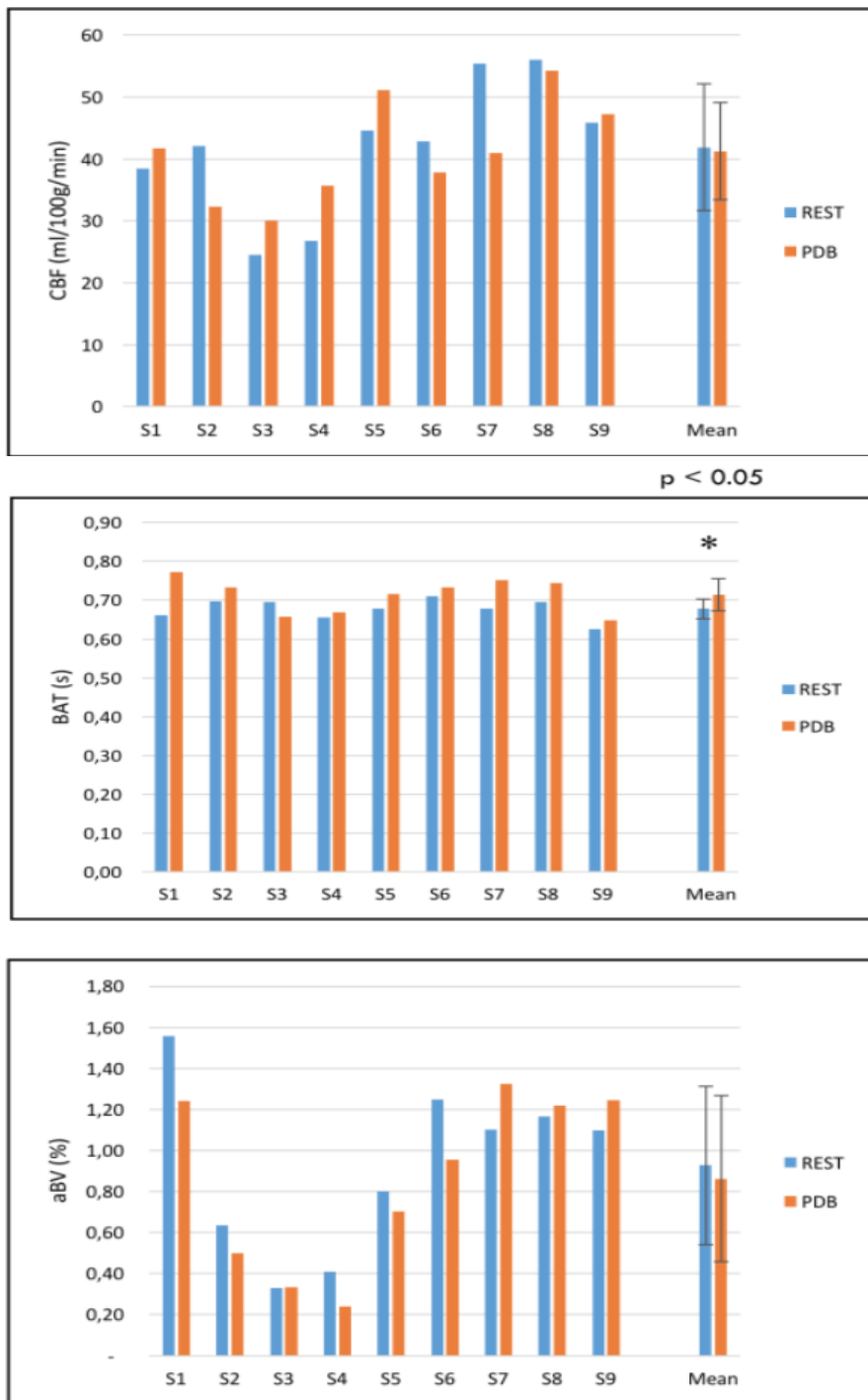


Figure 3.13 – Bar charts of CBF (top), BAT (middle) and aBV (bottom) maps for all subjects and in REST and PDB, using GM ROI mask. Error bars represent the standard deviation of the mean values and * denotes significant differences ($p < 0.05$).

The results above show that for CBF, in general, there is a small decrease in the subjects' mean from REST to PDB. However, this is not significantly different as five of the subjects actually suffer an increase in the mean value. In theory, when performing hypoxia there should be a decrease in brain perfusion due to the vasoconstriction that takes place, so overall the results are in agreement with this.

For BAT, it is observed that, in general, there is an increase in the subject's mean values from REST to PDB (only subject S3 showed a decrease). This is also in agreement with the theory and literature as with vasoconstriction and decrease in brain perfusion the labelled blood takes more time to reach the imaging region and consequently increasing the BAT. For this parameter, significant differences were found between REST and PDB, which supports its behaviour.

In hypocapnia, theoretically, the blood vessels should have smaller sizes due to the vasoconstriction that occurs. Therefore, the aBV should decrease in PDB when compared with REST, which is exactly what happens for almost all subjects (only S3, S7, S8 and S9 showed the opposite). Therefore, in general the model fitting is again in agreement with the literature and theory. However, in this case and similar to CBF, no significant differences were found between REST and PDB.

From Table 3.3 it is possible to see that the CBF, BAT and aBV values themselves are in agreement with the literature where CBF is in the range of 40 – 60 ml/100g/min, BAT is around 0.7 s and aBV is approximately 0.5 to 1.5 % (Chappell et al., 2010; Sousa et al., 2013).

It is worth mentioning that in all three parameters the subjects S2, S3, S4 and S5 show, overall, lower mean values, which is interesting as these are the subjects for which the data acquired had 28 slices instead of 9 like for the other subjects. Hence, this could mean that the more superior and inferior regions of the brain (present in the subjects with 28 slices) cause for the mean values to decrease. In order to investigate what really causes these changes, the following Figure 3.14 presents all the slices for CBF, BAT and aBV for subject S2, in both REST and PDB condition, using the GM ROI mask.

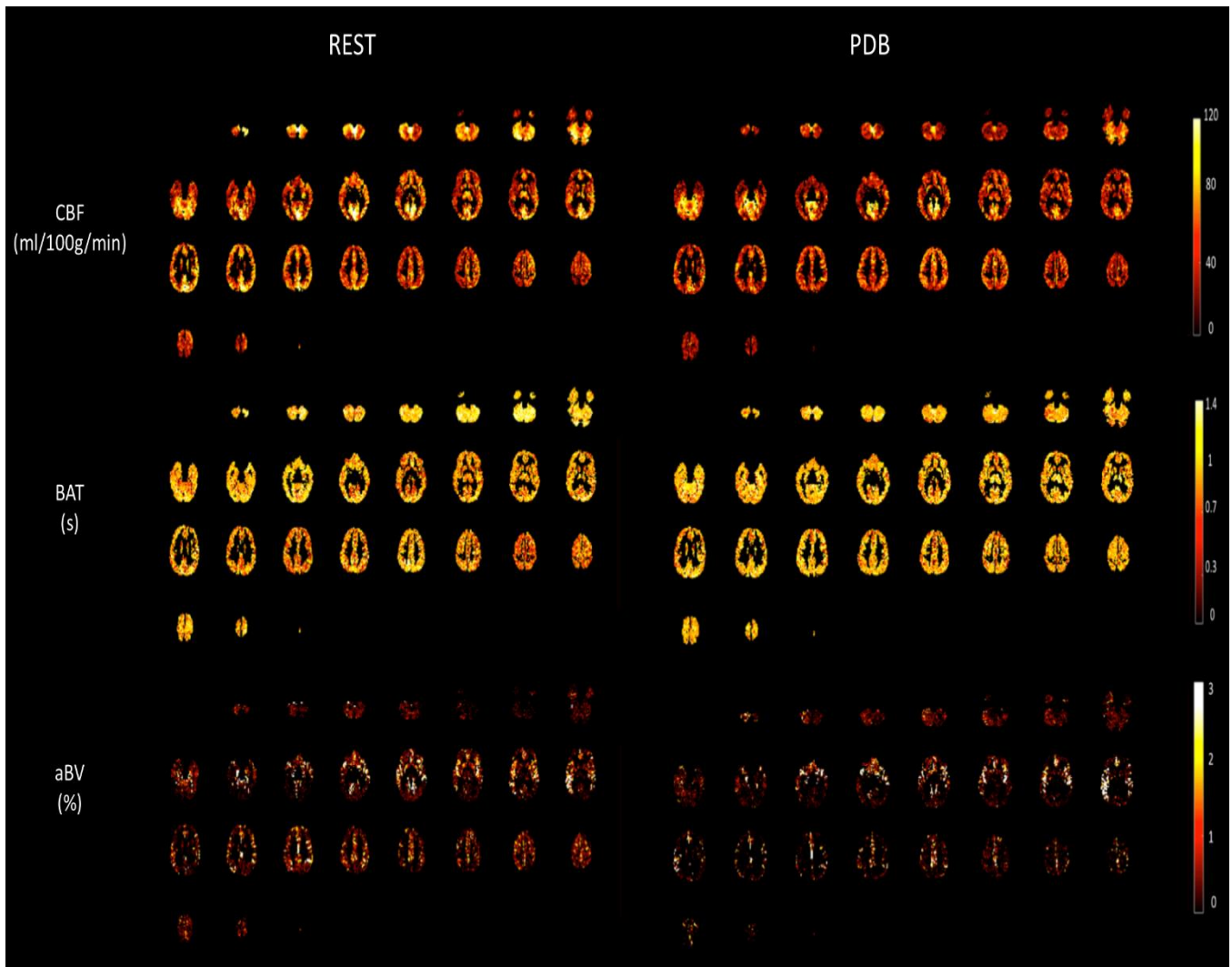


Figure 3.14 – CBF, BAT and aBV maps for subjects S2, in GM ROI mask.

The parameters' maps for all the other subjects are presented in the Appendix section, as well as the histograms of these maps, i.e., a graphic showing the values the voxels in each parameter's map take. Hence, helping to better understand the changes in the parameters' maps.

There is no apparent reason for the subjects with 28 slices to show, overall, lower mean values, as seen from the above figure and the ones on the Appendix section (Appendix 10-13). The only possible explanation is that the average process for these subjects' maps includes more voxels, in which there are inevitably more zero voxels that decrease the mean value.

It is possible to see from the above figure that, in general, there is greater brain perfusion in voxels from the inferior and posterior region. This area corresponds to the occipital lobe that is responsible for visual processing. A possible reason for this relatively greater brain perfusion is that the subject's eyes were open during REST, and in the case of PDB they had to follow the presentation of visual cues of the task, therefore activating this area. It is possible that the results from this area are misleading since there is no guarantee that the subject had his/her eyes open.

Therefore, there could be more brain perfusion in PDB when compared with REST in this area only because the subject's eyes were closed in REST and not in PDB.

In some subjects, differences in brain perfusion between the left and right hemispheres are detected. This is probably due to the head movement present in the data. The aBV parameter maps are very different from the CBF and BAT maps since almost all aBV signal is present in either the middle of the brain or in the lateral cerebral cortex. The Circle of Willis is located at the basis of the brain and is where the internal carotid arteries end and from where the anterior and posterior cerebral arteries begin, which explains the signal from the middle of the brain. The signal from the lateral cerebral cortex is explained with both left and right middle cerebral arteries (MCA) that supply blood to this area.

Despite the mean values obtained, it is possible to see from the figure above and the ones on the Appendix section (Appendix 10-13) that the subjects S2, S6, S7 and S8 have a clear decrease of brain perfusion from REST to PDB, i.e., there is a decrease of CBF and aBV and an increase of BAT, which was the expected. For subject S1, the increase of BAT and decrease of aBV is observed but for CBF it is clearly possible to see a decrease in some slices, as desired, but also an increase in others. As for the other subjects, either these effects are not possible to distinguish (subject S9) or the opposite effects are verified (subjects S3, S4 and S5). This shows that maybe these subjects did not perform real hypocapnia or there were too many problems with the acquisition, like head motion that corrupted the signal. Nonetheless, the results with the other masks are presented in the next section in order to compare with this mask and see if the maps results for these subjects improved.

3.4.2.2 Tissue and vascular ROI masks

In this section, similar results with the previous one will be displayed. However, in this case all the parameters' maps mean values were calculated in the Tissue and Vascular ROI masks (described in section 2.2.3) and also in the functional space. Table 3.4 shows these results obtained for each subject and each condition as well as Figure 3.15 that plots these results in the form of bar charts. As in the previous section a simple paired t-test with equal variances ($p < 0.05$) was also done between the two conditions.

Table 3.4 – Parameters' maps mean values obtained for every subject in both REST and PDB using Tissue and Vascular ROI masks. The subjects mean for each parameter is also present.

Subjects	CBF (ml/100g/min)		BAT (s)		aBV (%)	
	REST	PDB	REST	PDB	REST	PDB
S1	53.75	52.76	0.6141	0.7725	2.70	2.05
S2	57.81	38.70	0.6915	0.7198	1.19	0.87
S3	34.43	36.72	0.6855	0.6482	0.59	0.47
S4	38.63	37.32	0.6293	0.6676	0.68	0.35
S5	64.92	64.07	0.6579	0.7329	1.47	0.90
S6	59.05	52.57	0.6774	0.7112	2.89	2.05
S7	72.22	52.67	0.6392	0.7249	2.31	2.57
S8	81.33	67.68	0.6845	0.6739	2.45	2.26
S9	70.08	67.29	0.5915	0.6335	1.86	1.98
Mean ± standard deviation	59.14 ± 14.45	52.20 ± 11.80	0.6523 ± 0.03	0.6983 ± 0.04	1.79 ± 0.81	1.50 ± 0.80

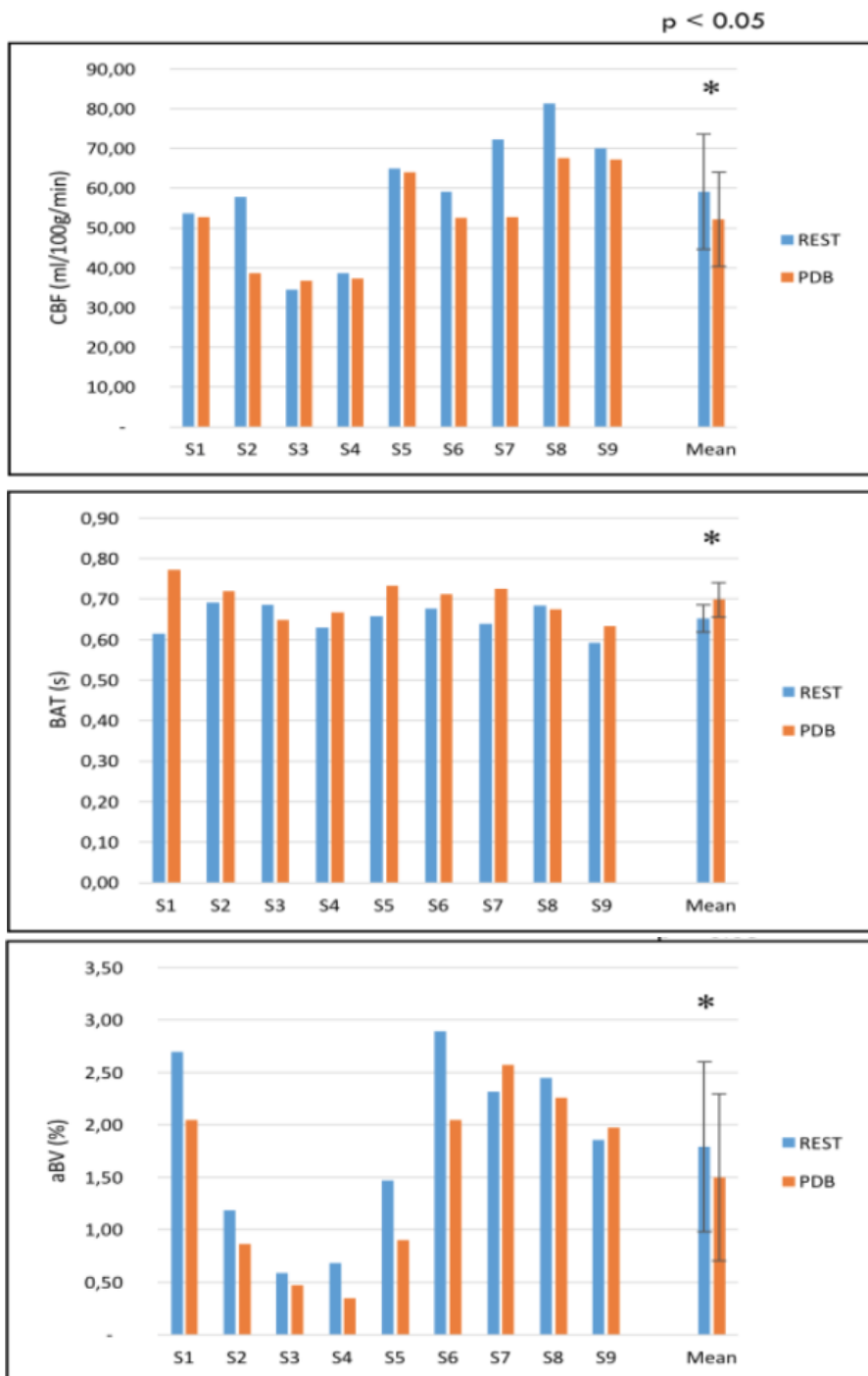


Figure 3.15 – Bar charts of CBF, BAT and aBV maps for all subjects and in REST and PDB, using Tissue and Vascular ROI masks. Error bars represent the standard deviation of the mean values and * denotes significant differences ($p < 0.05$).

For CBF all the mean values have increased when compared with the results from the previous section, which is expected since only the 40% percentile is considered in this mask. Besides, only one subject (S3) did not have the decrease from REST to PDB, which is a clear improvement from the previous section.

The Tissue mask does not have any threshold on the BAT parameter, however this mask is also used when obtaining the mean values of this parameter maps, so it is possible that some changes could be verified when comparing to the results from GM mask. This is actually the case as, overall, there is a decrease in these values using the Tissue mask. Subjects S3 and S8 showed a decrease from REST to PDB. Nonetheless, this is a not so good result as in the previous section, where only subject S3 had this decrease.

For aBV a similar behaviour as CBF takes place, since the Vascular mask applies a threshold in this parameter (as described in section 2.2.3). Hence, for aBV an increase in the mean values is also observed, using this mask. There is also an improvement in this mask since now only subjects S7 and S9 showed an increase from REST to PDB, which are fewer subjects than the results from the previous section.

With these Tissue and Vascular masks, the most important aspect that changes relative to the results from the previous section is the fact that now all three parameters are significantly different between REST and PDB. Therefore, these results are, in theory, better than the previous ones. Yet, it is important to realize that using these Tissue and Vascular ROI masks, a certain bias is potentially being introduced in the results as not all the GM voxels are being considered but instead only the ones with the greatest CBF values during REST.

Like, in the previous section the CBF, BAT and aBV maps for subject S2 in both REST and PDB condition, using the Tissue/Vascular ROI masks, are presented in the Figure 3.16.

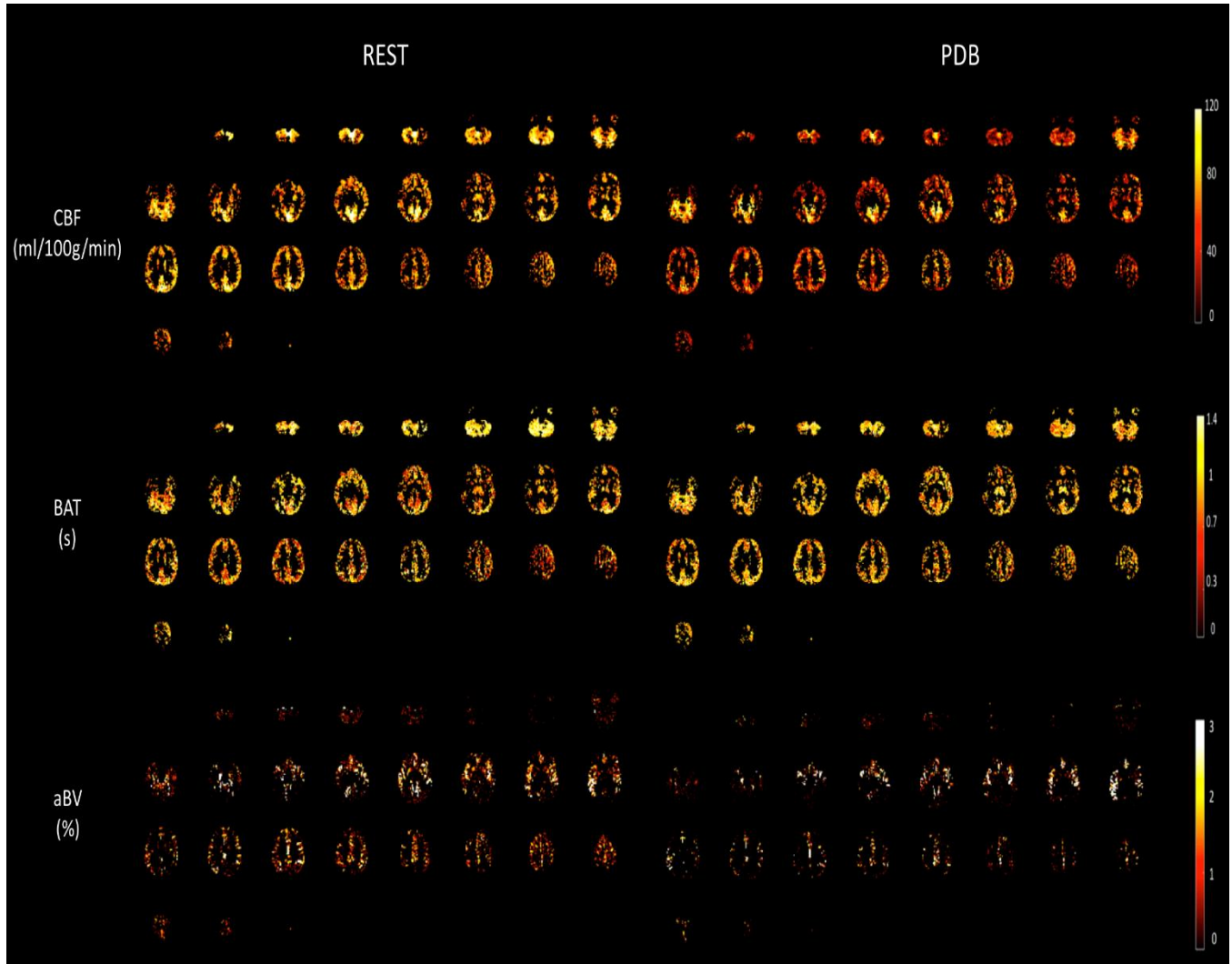


Figure 3.16 – CBF, BAT and aBV maps for subjects S2, in Tissue and Vascular ROI masks.

The parameters' maps for all the other subjects are presented in the Appendix section, as well as the histograms of these maps, i.e., a graphic showing the values the voxels in each parameter's map take. Hence, helping to better understand the changes in the parameters' maps.

The same aspects verified in the previous section maps are still present in the ones from Figure 3.16 and the figures from the Appendix section (Appendix 14-17), i.e., the occipital lobe still has an enhanced brain perfusion and the aBV signal is still present, almost exclusively, in the MCA area. The explanation for these is the same given in the previous section.

When comparing the maps in Tissue and Vascular ROI masks with the ones from the previous section it is possible to see some differences. For subjects S2, S6, S7 and S8 the same changes from REST to PDB are verified, i.e., the decrease of CBF and aBV and the increase of BAT, but with more significance, which is confirmed by the results from Table 3.8. Subjects S1 and S9 remain, more or less, the same in terms of changes from REST to PDB. As for subjects S4 and S5 there are clear improvements, since now it is difficult to see a certain change in the

parameters maps of the two conditions, in contrast with the clear opposite effects verified in the previous section. Finally, subject S3 still has the opposite effects (increase of CBF and aBV and decrease of BAT), which may confirm that this subject did not perform hypcapnia, despite the $P_{ET}CO_2$ results obtained.

In general, the results obtained with Tissue and Vascular ROI masks are better than the ones with GM ROI mask, so for the next analysis the first masks will be used.

3.4.2.3 MNI Atlas ROIs

As mentioned in section 2.2.3, an Atlas mask with nine anatomical cortical regions was used as basis for the GM mask and consequently for the Tissue and Vascular masks. Following the previous section, it was decided to separate these nine regions and perform the parameter's estimation for each region. This was done in the functional space and using the Tissue and Vascular masks. Like before, the mean values for each parameter map, for each subject and in both REST and PDB condition, were calculated. Then, these values were averaged within each anatomical region and condition and are now presented in Figure 3.17 that displays these results in the form of bar charts. For each region, a simple paired t-test with equal variances ($p < 0.05$) was done between the two conditions, REST and PDB. These nine anatomical cortical regions are: caudate nucleus (Atlas 1), cerebellum (Atlas 2), frontal cortex (Atlas 3), insula (Atlas 4), occipital cortex (Atlas 5), parietal cortex (Atlas 6), putamen (Atlas 7), temporal cortex (Atlas 8) and thalamus (Atlas 9).

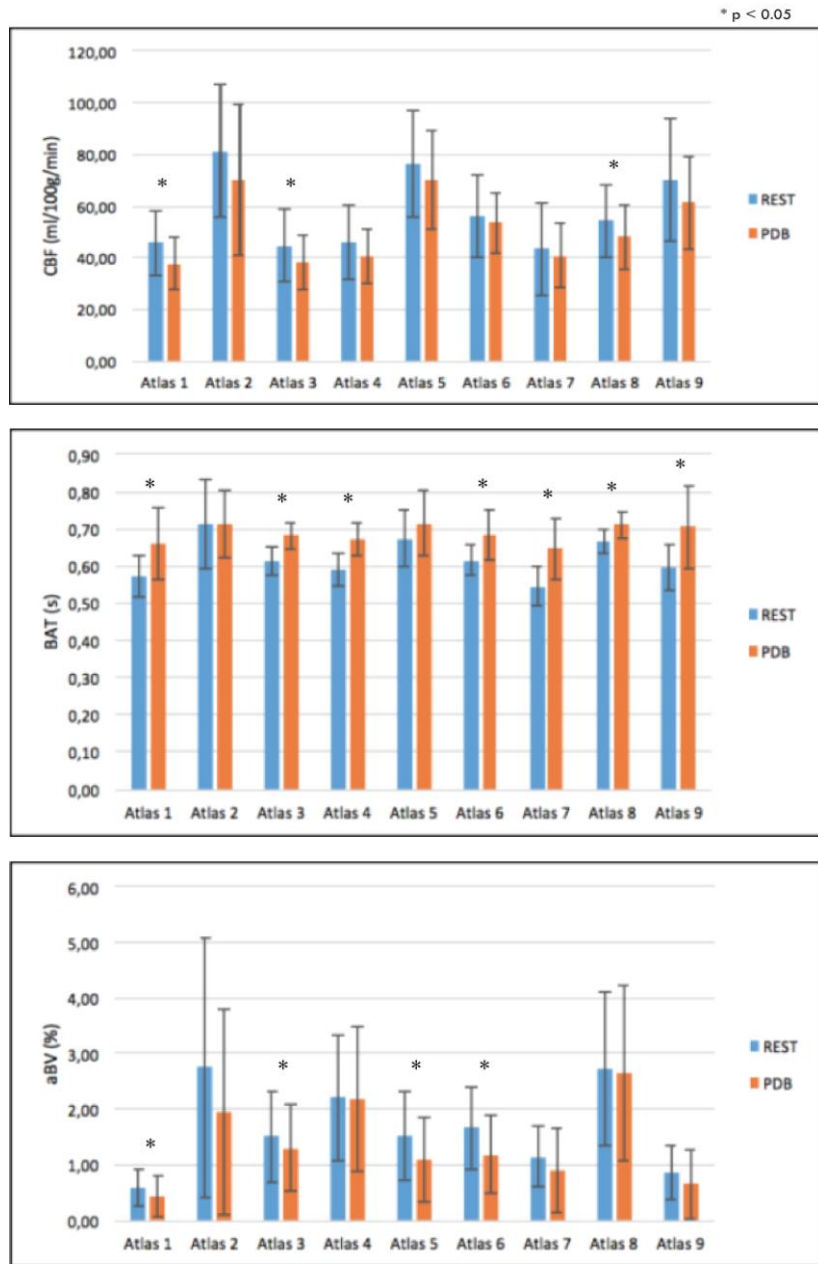


Figure 3.17 – Bar charts of mean values obtained for each anatomical region in both REST and PDB, after averaging all subjects in each region and condition. Error bars represent the standard deviation of the mean values and * denotes significant differences ($p<0.05$).

Some aspects can be discussed with these results. First, for all three parameters there are very different results across the 9 regions, which can be expected as the level of brain perfusion is not the same throughout the brain. Consequently there are regions that have more brain perfusion than others, like, for example, the regions from Atlas 2 (cerebellum) or Atlas 5 (occipital cortex) that have more perfusion, which is expected due to the visual activation and the regions from Atlas 1 (caudate nucleus) and Atlas 7 (putamen) that have less brain perfusion.

Another aspect worth mention is that for all anatomical regions the behaviours of the parameters in both conditions are kept the same, like in the previous sections, i.e., CBF and aBV decrease from REST to PDB and BAT increases. This is important because it shows that the results are in agreement with the theory, which suggests that the changes in the brain perfusion are global.

As for the significant differences between REST and PDB, the results are described now. For CBF only three anatomical regions had significant differences (Atlas 1, 3 and 8). For BAT, significant differences were found in six regions (Atlas 1, 3, 4, 6, 7 and 8). The aBV parameter reached significant differences in four regions (Atlas 1, 3, 5 and 6). These results show what was just now discussed, that the brain perfusion is not the same across the brain but the responses to hypcapnia are global.

3.4.2.4 Voxelwise whole-brain comparison

The goal of the statistical analysis present in this section was to assess if the parameters maps estimated in REST and PDB were significantly different between these two conditions. The FSL Randomise tool was used to do this and allowed to choose the technique wanted for this assessment. This FSL tool outputs corrected and uncorrected results. The goal was to obtain the significantly different ($p < 0.05$) voxels for each parameter's map.

Threshold-Free Cluster Enhancement

The results presented in this section were obtained using the Threshold-Free Cluster Enhancement (TFCE) technique, described in section 2.3.2. The parameters' maps used for this analysis were both the maps obtained with the GM ROI mask and the ones with the Tissue and Vascular ROI masks. The results were overlapped with the MNI152 T_1 -weighted image in the standard space in order to better visualize which brain regions had significant differences. Figures 3.18 and 3.19 presents the CBF and aBV uncorrected results in GM and Tissue/Vascular masks.

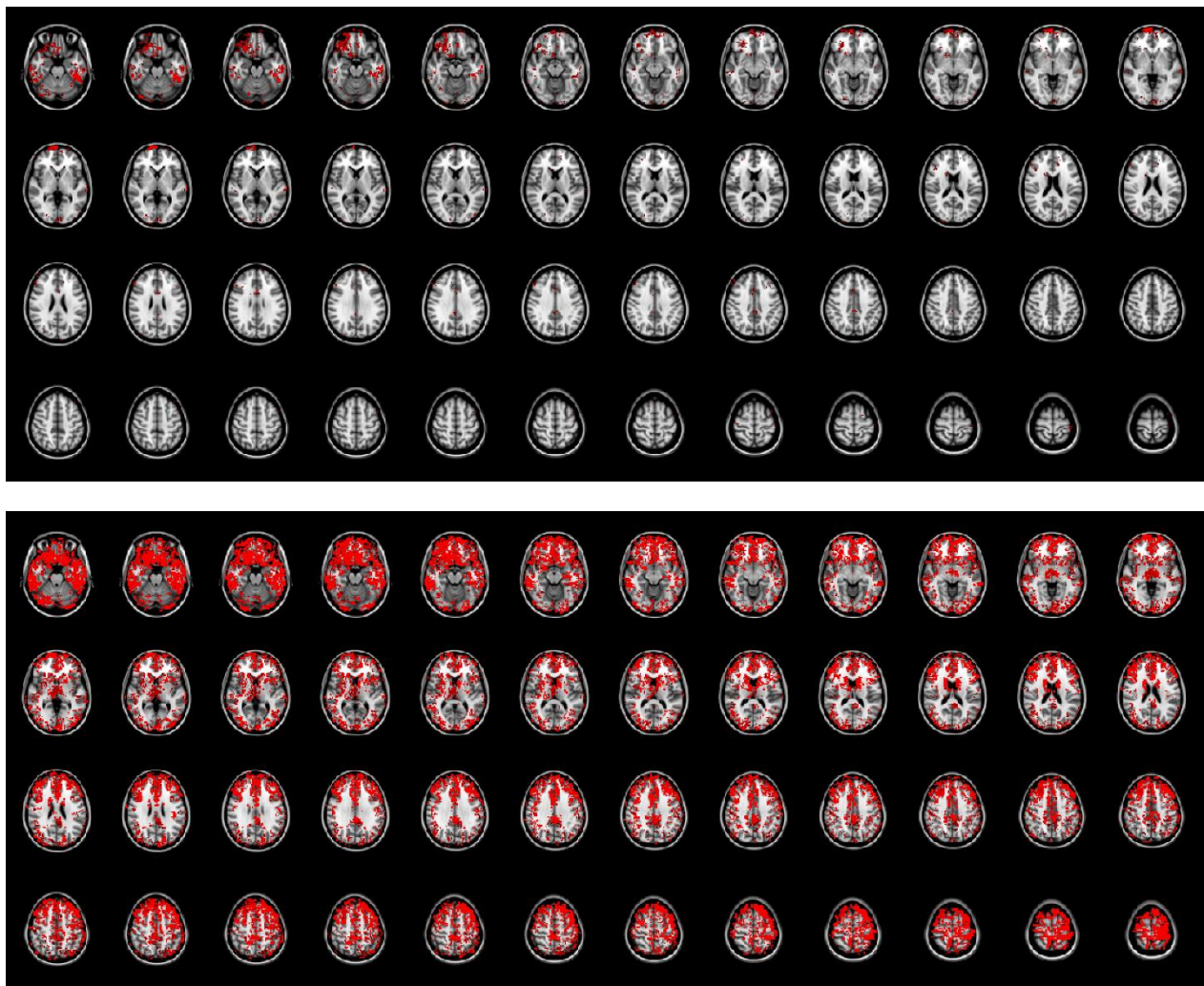


Figure 3.18 – CBF uncorrected results using TFCE. (Top) CBF with GM ROI mask and (bottom) with Tissue ROI mask.

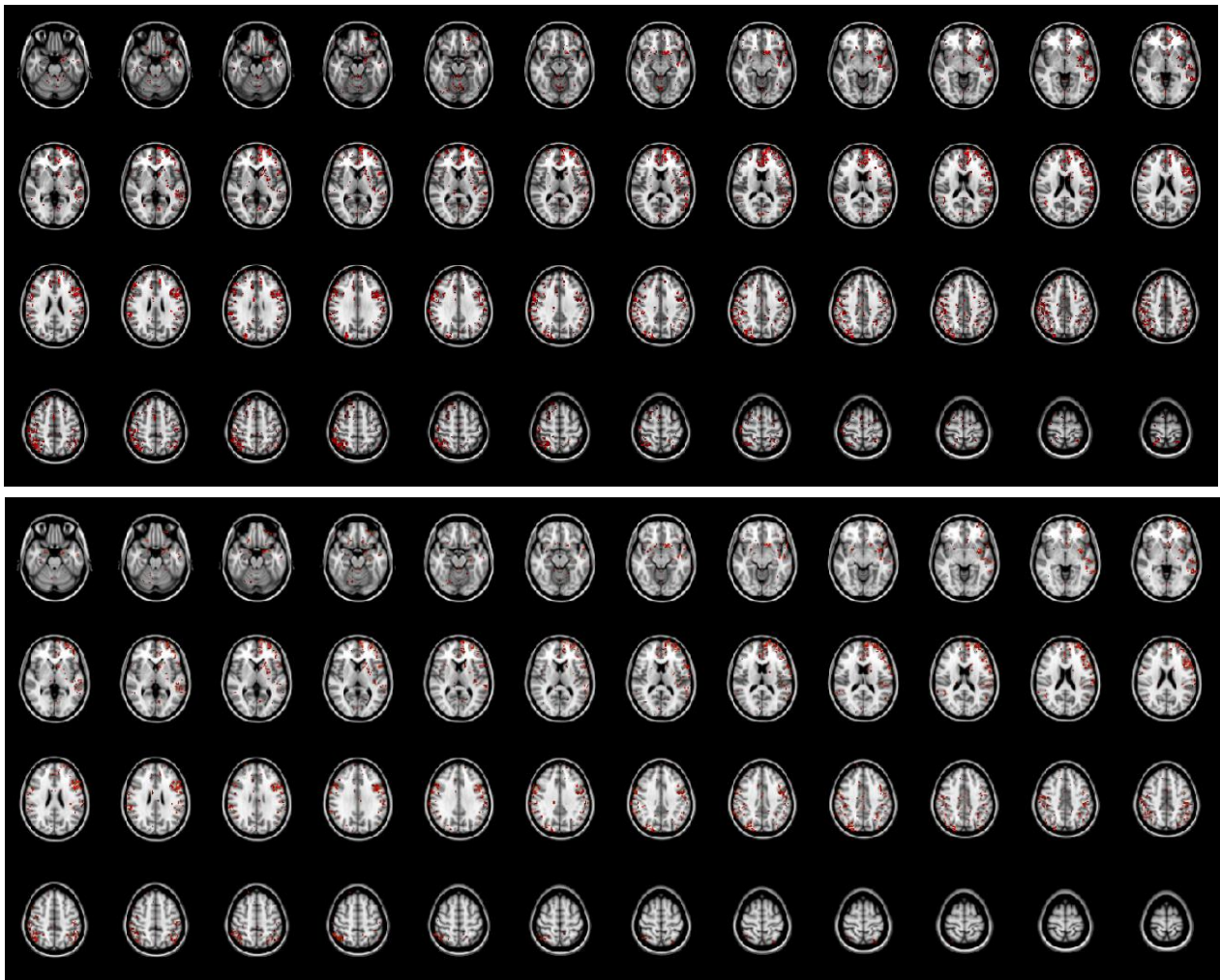


Figure 3.19 – aBV uncorrected results using TFCE. (Top) aBV with GM ROI mask and (bottom) with Vascular ROI mask.

Only the uncorrected results are presented because the maps from the corrected ones were totally empty. The results for BAT are also not displayed for the same reason. This suggests that for BAT the maps from REST and PDB were not that different.

For CBF, Figure 3.18 shows that the results with Tissue ROI mask are better than the ones with GM ROI mask, which is expected due to the threshold applied in the first mask. It is also possible to see that for the results with Tissue ROI mask the more inferior and superior regions of the brain have plenty of voxels significantly different, which is related with the subjects that had 28 slices acquired, in contrast with the ones with 9 slices. The frontal cortical regions also have more voxels significantly different, which is curious since, in theory, changes in brain perfusion are a global effect.

The aBV results with Vascular ROI mask are more or less equal to the ones with GM ROI mask. This suggests that for this parameter, the Vascular ROI mask does not have a stronger influence on the parameter map than the GM ROI mask.

Voxel-wise thresholding

In this section, the results presented were obtained using the Voxel-wise technique, described in section 2.3.2. The condition for this analysis was the same as previously, the parameters' maps used for this analysis were again the maps obtained with the GM ROI mask and the Tissue and Vascular ROI masks and the results were also overlapped with MNI152 T_1 -weighted image in the standard space. Figures 3.20 and 3.21 presents the CBF and aBV uncorrected results in GM and Tissue/Vascular masks.

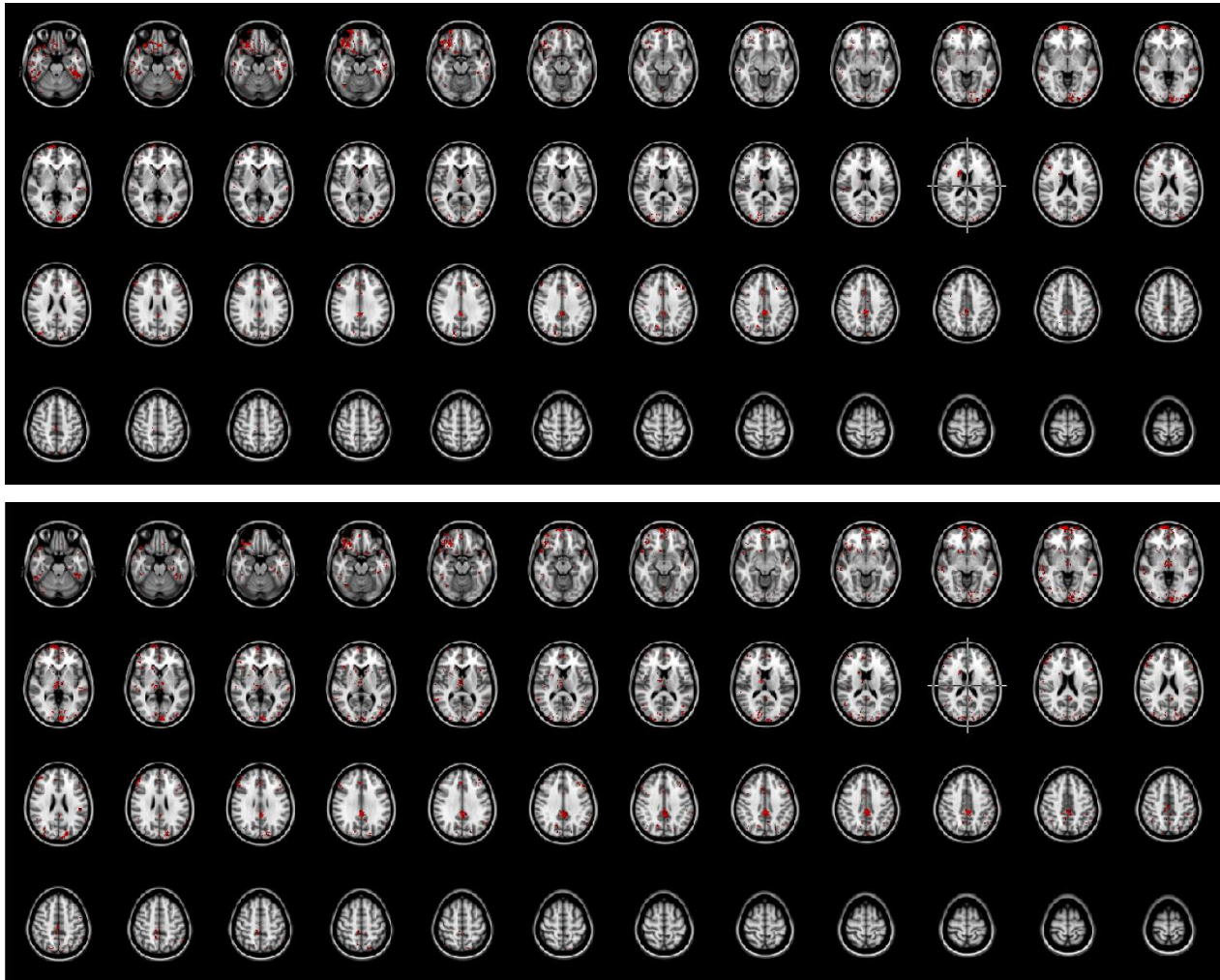


Figure 3.20 – CBF uncorrected results using Voxel-wise. (Top) CBF with GM ROI mask and (bottom) with Tissue ROI mask.

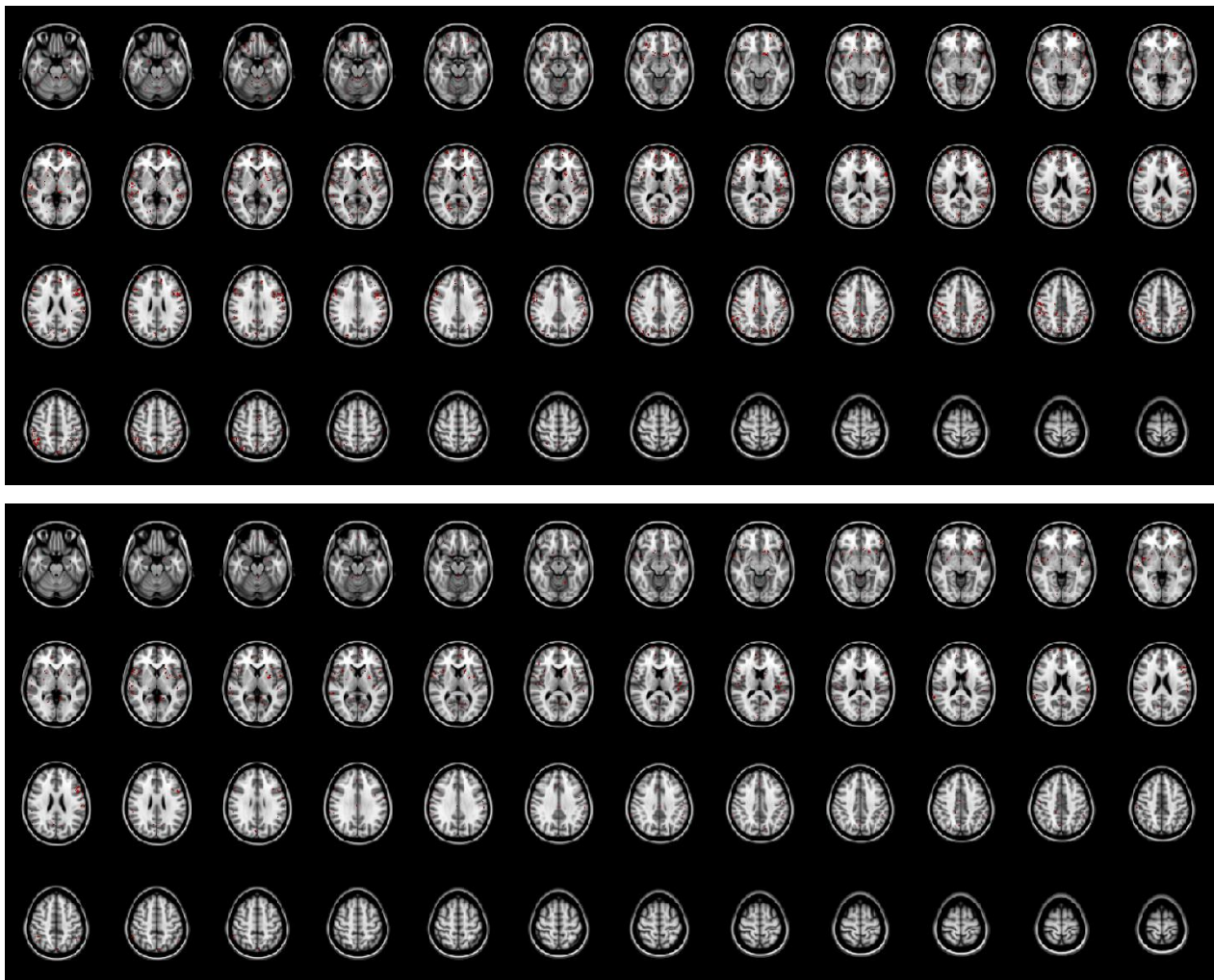


Figure 3.21 – aBV uncorrected results using Voxel-wise. (Top) aBV with GM ROI mask and (bottom) with Vascular ROI mask.

For the same reasons as in the previous sections, both the corrected results for CBF and aBV and the results for BAT are not presented.

The Figures above show that using the Voxel-wise, technique there are almost no significant different voxels in CBF and aBV, for both GM ROI mask and Tissue/Vascular masks. This suggests that for the results obtained in this work this technique is not very suitable. Therefore, the previous technique, TFCE, is more adequate.

3.4.3 Correlation with $P_{ET}CO_2$

With the group analysis complete it was then possible to perform the statistical analysis on those results. In this section, the results of the correlation between the parameters and the $P_{ET}CO_2$ in both REST and PDB conditions are presented. More precisely, the parameters' maps mean values of PDB were subtracted to these values of REST for each subject, yielding ΔCBF ,

ΔBAT and ΔaBV . Then these differenced values were correlated with the differenced $P_{\text{ET}}\text{CO}_2$ (REST – PDB), $\Delta P_{\text{ET}}\text{CO}_2$, again for each subject. This process was done for both GM ROI mask and Tissue and Vascular ROI masks. The correlation coefficients and respective p-value (paired t-test, $p < 0.05$) for each parameter are presented in Table 3.5 and in Figures 3.22 and 3.23.

Table 3.5 – Correlation coefficients and p-values for each parameter and in both GM mask and Tissue/Vascular masks.

Parameters	GM ROI Mask		Tissue/Vascular ROI Masks	
	Correlation coefficient	p-value	Correlation coefficient	p-value
CBF	0.033	0.932	-0.270	0.482
BAT	-0.314	0.410	-0.388	0.302
aBV	0.509	0.161	0.545	0.129

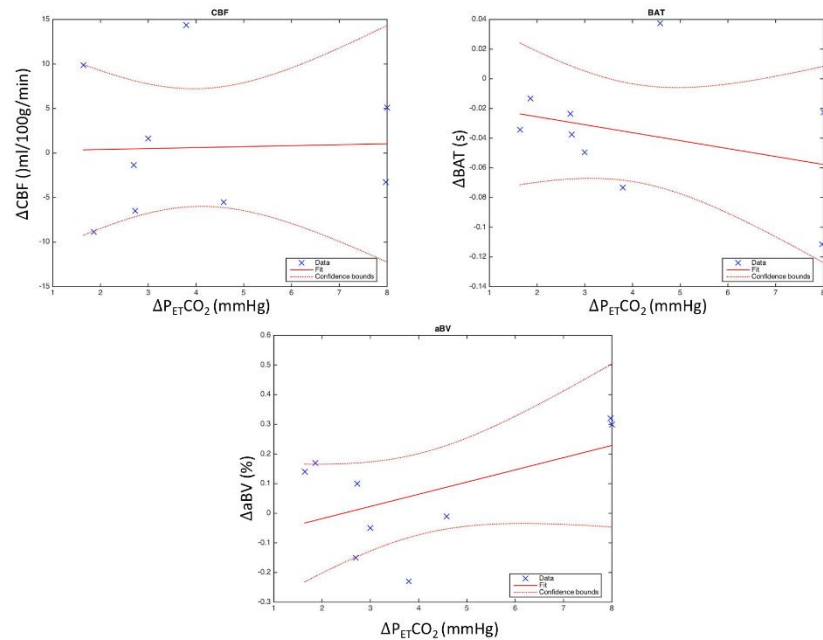


Figure 3.22 – Correlation results for CBF, BAT and aBV with GM ROI mask.

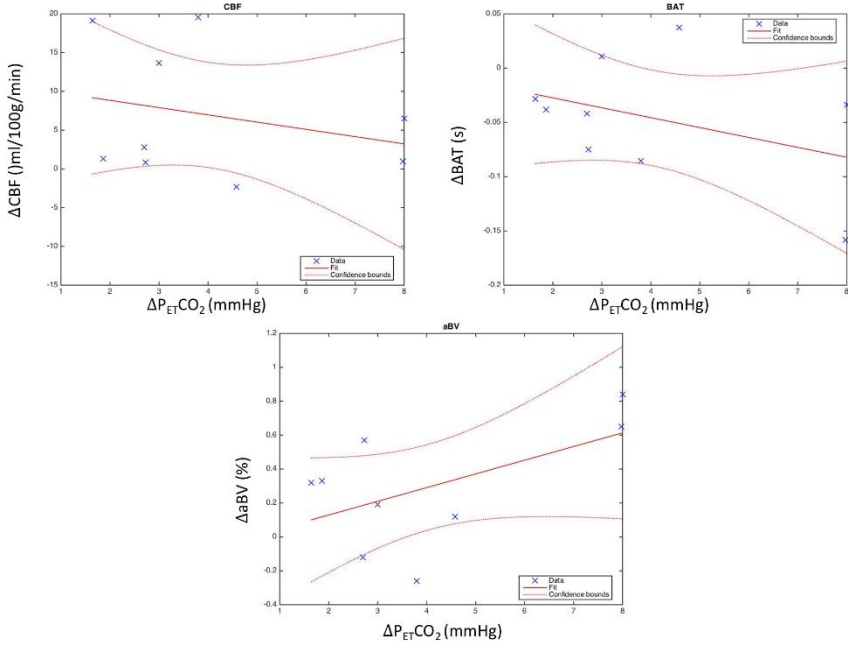


Figure 3.23 – Correlation results for CBF, BAT and aBV with Tissue and Vascular ROI mask.

Theoretically, the greater the $\Delta P_{ET}CO_2$ the greater the ΔCBF and ΔaBV should be, because the more hypocapnia the subject experiences, the less brain perfusion and more vasoconstriction happens in the brain, leading to a decrease in both CBF and aBV. For ΔBAT this relationship is inverted, i.e., the more hypocapnia, the greater the time it takes for the labelled blood to reach the imaging region, consequence of the vasoconstriction and less brain perfusion. Therefore, in theory, for CBF and aBV there should be a positive correlation with $P_{ET}CO_2$ and for BAT a negative one.

The results obtained (Table 3.10, Figures 3.22 and 3.23) show that for GM ROI mask all three parameters are in agreement with the theory, yet the CBF correlation coefficient is very small, exhibiting that the correlation is not very strong. For the Tissue and Vascular ROI masks CBF loses the little correlation that the previous mask had but BAT and aBV show an improvement in the correlation observed when compared with the GM ROI mask. For neither of the masks used significant differences were reached between the differenced parameters values and $\Delta P_{ET}CO_2$.

There are several possibilities to explain these results obtained. The main reason is that the quantitative values of $\Delta P_{ET}CO_2$ are not completely accurate due to poor calibration in the PetCO₂ measurements. Another possible reason is the head movement that the subjects had, that could have biased the model fitting and consequently the parameters' estimations.

4 Conclusions

In summary, this work explored the behaviour of the brain perfusion when subjected to a hypocapnia task, investigating the best ways to estimate the perfusion and arterial parameters and examining the masks to be used for the estimations, as well as the study of the statistical analysis. Therefore, an appropriate kinetic modelling approach for the quantitative mapping of brain perfusion, bolus arrival time and blood volume was developed, using multi-TI ASL MRI acquisitions during baseline and hypocapnia conditions.

An important effect of the distribution of the BAT prior on the variability of the BAT estimates was found, and it was concluded that a relatively larger prior should be used if significant changes in the BAT parameter are to be found. This is particularly critical in hypocapnia, since the decreased blood flow in this case is expected to prolong the arterial transit time and hence increase BAT.

Overall, the model fitting developed was adequate and with the macro-vascular component, it was possible to isolate the intra-vascular signal (aBV), yielding a brain perfusion signal more or less free of contamination from large blood vessels. This extra component creates an alternative for the flow-suppression techniques which may limit the already very low SNR of the data. In general the Bayesian model fitting method used here seems to provide a good alternative to standard least squares methods, provided that care is taken in the definition of the parameters priors according to the study of interest.

The group analysis results obtained in this work showed a characteristic behaviour of brain perfusion while the subject is experiencing hypocapnia, when compared with the baseline condition. In general, when in hypocapnia, CBF and aBV suffer a decrease and BAT an increase. This was expected, as hypocapnia leads to vasoconstriction causing a decrease in blood perfusion, which in turn lengthens the time it takes for the labelled blood to reach the imaging region (hence increasing BAT) and the decreases the arterial blood volume (hence decreasing aBV).

These changes were significant within the Tissue and Vascular ROIs defined based on the CBF and aBV results at rest, respectively. The CBF decrease was however not significant in an anatomically defined GM ROI, which probably reflects a poor SNR and consequently poor model fitting, leading to limited sensitivity. Such limited sensitivity of our data may also explain the lack of significant differences over the whole brain in our voxelwise comparison between hypocapnia and rest conditions. Nevertheless, some brain regions did show significant effects, if uncorrected for multiple comparisons..

In order to improve the study's sensitivity, more subjects should be used. Moreover, because the $P_{ET}CO_2$ results excluded some subjects that did not show hypocapnia despite performing the task, perhaps some modifications should be made to the paced deep breathing paradigm so that it could be guaranteed that the subject is achieving hypocapnia. It also became

clear that in hypocapnia there is a greater amount of head movement, which damps the ASL MRI signal. This was verified through the head mean displacement results, as well as the number of bad fitting voxels, which reflected the difficulty of the model fitting in correctly estimating the parameters when the subject is performing hypocapnia.

Future Work

In spite of the non-invasive nature of ASL MRI, which is the reason for this technique being thoroughly studied in the recent years, one very important problem remains, the low SNR. Even with methods like averaging, this problem continues to be present in the data and further research should be made to attenuate its relevance.

The paced deep breathing task itself should be improved in order to guarantee that the subjects are performing hypocapnia and not moving at all (so that there is no head motion). Also, so as to reduce the inter-subject variability of the $P_{ET}CO_2$ results, a more careful regulation of the rate and depth of the subjects breathing should be done. Another important aspect is that for this task the instructions are given as visual cues, therefore, some unwanted visual (occipital) activation could be present and yielding misleading results, as there is no guarantee that the subject had his/her eyes open in both REST and PDB conditions. This could be assessed with a control experiment with auditory cues instead.

Further research about the masks and thresholds to be used should be made as the results obtained with these are far from optimal and there are several different possibilities. Likewise, for the several options that the FSL BASIL toolbox offers. It is also essential to increase the number of subjects in the study in order to have a more representative group analysis.

5 References

- Alsop, D. C., Detre, J. a., Golay, X., Günther, M., Hendrikse, J., Hernandez-Garcia, L., & Zaharchuk, G. (2014). Recommended implementation of arterial spin-labeled perfusion MRI for clinical applications: A consensus of the ISMRM perfusion study group and the european consortium for ASL in dementia. *Magnetic Resonance in Medicine*, 00(October 2013).
- AnaesthesiaUK. (2007). Cerebral Blood Flow. Retrieved July 30, 2015, from <http://www.anaesthesiauk.com/article.aspx?articleid=100754>
- Attias, H. (1999). A variational Bayesian framework for graphical models. In *Advances in Neural Information Processing Systems (NIPS)* (pp. 209–215).
- Attwell, D., & Iadecola, C. (2002). The neural basis of functional brain imaging signals. *Trends in Neurosciences*.
- Bloch, F. (1946). Nuclear Induction. *Physical Review*, 70(7-8), 460–474.
- Bor-Seng-Shu, E., Kita, W. S., Figueiredo, E. G., Paiva, W. S., Fonoff, E. T., Teixeira, M. J., & Panerai, R. B. (2012). Cerebral hemodynamics: concepts of clinical importance. *Arquivos de Neuro-Psiquiatria*, 70(5), 352–356.
- Bright, M. G., Bulte, D. P., Jezzard, P., & Duyn, J. H. (2009). Characterization of regional heterogeneity in cerebrovascular reactivity dynamics using novel hypoxia task and BOLD fMRI. *NeuroImage*, 48(1), 166–175.
- Buxton, R. B. (2002). Introduction to Functional Magnetic Resonance Imaging: Principles and Techniques. *Energy*, 24(2), xi, 523 p.
- Buxton, R. B. (2005). Quantifying CBF with arterial spin labeling. *Journal of Magnetic Resonance Imaging*, 22(6), 723–726.
- Buxton, R. B., Frank, L. R., Wong, E. C., Siewert, B., Warach, S., & Edelman, R. R. (1998). A general kinetic model for quantitative perfusion imaging with arterial spin labeling. *Magnetic Resonance in Medicine : Official Journal of the Society of Magnetic Resonance in Medicine*, 40(3), 383–396.
- Çavuşoğlu, M., Pfeuffer, J., Uğurbil, K., & Uludağ, K. (2009). Comparison of pulsed arterial spin labeling encoding schemes and absolute perfusion quantification. *Magnetic Resonance Imaging*, 27(8), 1039–1045.

- Chappell, M. a., Groves, a. R., Whitcher, B., & Woolrich, M. W. (2009). Variational Bayesian Inference for a Nonlinear Forward Model. *IEEE Transactions on Signal Processing*, 57(1), 223–236.
- Chappell, M. a., MacIntosh, B. J., Donahue, M. J., Günther, M., Jezzard, P., & Woolrich, M. W. (2010). Separation of macrovascular signal in multi-inversion time arterial spin labelling MRI. *Magnetic Resonance in Medicine*, 63(5), 1357–1365.
- Chappell, M. a., Woolrich, M. W., Petersen, E. T., Golay, X., & Payne, S. J. (2013). Comparing model-based and model-free analysis methods for QUASAR arterial spin labeling perfusion quantification. *Magnetic Resonance in Medicine*, 69(5), 1466–1475.
- Chen, J. J., & Pike, G. B. (2010). MRI measurement of the BOLD-specific flow-volume relationship during hypercapnia and hypocapnia in humans. *NeuroImage*, 53(2), 383–391.
- Chen, J. J., Wieckowska, M., Meyer, E., & Pike, G. B. (2008). Cerebral blood flow measurement using fMRI and PET: A cross-validation study. *International Journal of Biomedical Imaging*, 2008(1).
- Cipolla, M. J. (2009). The Cerebral Circulation. *Colloquium Series on Integrated Systems Physiology: From Molecule to Function*.
- Collins, D., Holmes, C., Peters, T., & Evans, A. (1995). Automatic 3-D model-based neuroanatomical segmentation. *Hum. Brain Mapp.*, 208(1995), 190–208.
- Dai, W., Garcia, D., De Bazelaire, C., & Alsop, D. C. (2008). Continuous flow-driven inversion for arterial spin labeling using pulsed radio frequency and gradient fields. *Magnetic Resonance in Medicine*, 60(6), 1488–1497.
- Donahue, M. J., Faraco, C. C., Strother, M. K., Chappell, M. a, Rane, S., Dethrage, L. M., & Siero, J. C. W. (2014). Bolus arrival time and cerebral blood flow responses to hypercarbia. *Journal of Cerebral Blood Flow and Metabolism: Official Journal of the International Society of Cerebral Blood Flow and Metabolism*, 34(7), 1243–52.
- Figueiredo, P. M., Clare, S., & Jezzard, P. (2005). Quantitative perfusion measurements using pulsed arterial spin labeling: Effects of large region-of-interest analysis. *Journal of Magnetic Resonance Imaging*, 21(6), 676–682.
- Golay, X., & Petersen, E. (2007). Arterial spin labeling: a one-stop-shop for measurement of brain perfusion in the clinical settings. *Engineering in Medicine*, 2007, 4320–4323.

- Greve, D. N., & Fischl, B. (2009). Accurate and robust brain image alignment using boundary-based registration. *NeuroImage*, 48(1), 63–72.
- Groves, A. R., Chappell, M. A., & Woolrich, M. W. (2009). Combined spatial and non-spatial prior for inference on MRI time-series. *NeuroImage*, 45(3), 795–809.
- Günther, M. (2013). Perfusion Imaging. *Journal of Magnetic Resonance Imaging: JMRI*, 279, 269–279.
- Haddad, S. H., & Arabi, Y. M. (2012). Critical care management of severe traumatic brain injury in adults. *Scandinavian Journal of Trauma, Resuscitation and Emergency Medicine*, 20, 12.
- Henderson, K. K., & Byron, K. L. (2007). Vasopressin-induced vasoconstriction: two concentration-dependent signaling pathways. *Journal of Applied Physiolog*, 102(4), 1402–1409.
- Herscovitch, P., & Raichle, M. E. (1985). What is the correct value for the brain–blood partition coefficient for water? *Journal of Cerebral Blood Flow and Metabolism: Official Journal of the International Society of Cerebral Blood Flow and Metabolism*, 5(1), 65–69.
- Ho, Y.-C. L., Petersen, E. T., Zimine, I., & Golay, X. (2011). Similarities and differences in arterial responses to hypercapnia and visual stimulation. *Journal of Cerebral Blood Flow and Metabolism: Official Journal of the International Society of Cerebral Blood Flow and Metabolism*, 31(2), 560–571.
- Hutchinson, E. B., Stefanovic, B., Koretsky, A. P., & Silva, A. C. (2006). Spatial flow-volume dissociation of the cerebral microcirculatory response to mild hypercapnia. *NeuroImage*, 32(2), 520–530.
- Ibaraki, M., Shimosegawa, E., Miura, S., Takahashi, K., Ito, H., Kanno, I., & Hatazawa, J. (2004). PET measurements of CBF, OEF, and CMRO₂ without arterial sampling in hyperacute ischemic stroke: method and error analysis. *Annals of nuclear medicine* (Vol. 18).
- Ito, H., Kanno, I., Ibaraki, M., Hatazawa, J., & Miura, S. (2003). Changes in human cerebral blood flow and cerebral blood volume during hypercapnia and hypocapnia measured by positron emission tomography. *J Cereb Blood Flow Metab*, 23(6), 665–670.
- Ito, H., Kanno, I., Kato, C., Sasaki, T., Ishii, K., Ouchi, Y., & Senda, M. (2004). Database of normal human cerebral blood flow, cerebral blood volume, cerebral oxygen extraction fraction and cerebral metabolic rate of oxygen measured by positron emission tomography with ¹⁵O-labelled carbon dioxide or water, carbon monoxide and oxygen: *European Journal of Nuclear Medicine and Molecular Imaging*, 31(5), 635–643.

- Jenkinson, M., Bannister, P., Brady, M., & Smith, S. M. (2002). Improved optimisation for the robust and accurate linear registration and motion correction of brain images. *NeuroImage*, 17, 825–841.
- Jenkinson, M., Beckmann, C. F., Behrens, T. E. J., Woolrich, M. W., & Smith, S. M. (2012). FSL. *NeuroImage*.
- Jenkinson, M., & Smith, S. (2001). A global optimisation method for robust affine registration of brain images. *Medical Image Analysis*, 5(2), 143–156.
- Jezzard, P., Mathews, P., & Stephen Smith. (2001). *Functional MRI: An Introduction to Methods*. Oxford University Press.
- Kastrup, A., Li, T. Q., Glover, G. H., & Moseley, M. E. (1999). Cerebral blood flow-related signal changes during breath-holding. *American Journal of Neuroradiology*, 20(7), 1233–1238.
- Kelly, D. F., Martin, N. A., Kordestani, R., Counelis, G., Hovda, D. A., Bergsneider, M., & Becker, D. P. (1997). Cerebral blood flow as a predictor of outcome following traumatic brain injury. *Journal of Neurosurgery*, 86(4), 633–641.
- King, A., Serena, J., Bornstein, N. M., & Markus, H. S. (2011). Does impaired cerebrovascular reactivity predict stroke risk in asymptomatic carotid stenosis?: A prospective substudy of the asymptomatic carotid emboli study. *Stroke*, 42(6), 1550–1555.
- Leontiev, O., & Buxton, R. B. (2007). Reproducibility of BOLD, perfusion, and CMRO₂ measurements with calibrated-BOLD fMRI. *NeuroImage*, 35(1), 175–184.
- Liu, T. T., & Brown, G. G. (2007). Measurement of cerebral perfusion with arterial spin labeling: Part 1. Methods. *Journal of the International Neuropsychological Society : JINS*, 13(3), 517–525.
- Liu, T. T., & Wong, E. C. (2005). A signal processing model for arterial spin labeling functional MRI. *NeuroImage*, 24(1), 207–215.
- Luh, W., Luh, W., Wong, E. C., Wong, E. C., Bandettini, P. a., Bandettini, P. a., & Hyde, J. S. (1999). QUIPSS II With Thin-Slice TI 1 Periodic Saturation: A Method for Improving Accuracy of Quantitative Perfusion Imaging Using Pulsed Arterial Spin Labeling. *Magnetic Resonance in Medicine*, 1254, 1246–1254.
- Mazziotta, J., Toga, A., Evans, A., Fox, P., Lancaster, J., Zilles, K., & Mazoyer, B. (2001). A probabilistic atlas and reference system for the human brain: International Consortium for

Brain Mapping (ICBM). *Philosophical Transactions of the Royal Society of London. Series B, Biological Sciences*, 356(1412), 1293–1322.

Mielck, F., Wietasch, G., Weyland, A., Buhre, W., Meier-Theile, C., Hoeft, A., & Sonntag, H. (2001). Reliability of cerebral blood flow measurements by transcerebral double-indicator dilution technique. *European Journal of Anaesthesiology*, 18(10), 653–661.

Nichols, T. E., & Holmes, A. P. (2002). Nonparametric permutation tests for functional neuroimaging: A primer with examples. *Human Brain Mapping*, 15(1), 1–25.

Nunes, S. (2014). Characterization of physiological noise in resting-state fMRI data at 7T. Master Degree thesis in Biomedical Engineering, Instituto Superior Técnico, Universidade de Lisboa.

Paulson, O. B., Strandgaard, S., & Edvinsson, L. (1990). Cerebral autoregulation. *Cerebrovasc Brain Metab Rev*, 2, 161–192.

Pindzola, R. R., Balzer, J. R., Nemoto, E. M., Goldstein, S., & Yonas, H. (2001). Cerebrovascular reserve in patients with carotid occlusive disease assessed by stable xenon-enhanced ct cerebral blood flow and transcranial Doppler. *Stroke; a Journal of Cerebral Circulation*, 32(8), 1811–1817.

Pinto, J. (2012). *Spatiotemporal dynamics of CBF and BOLD fMRI responses to breath-hold challenges*. Master Degree thesis in Biomedical Engineering, Instituto Superior Técnico, Universidade de Lisboa.

Posse, S., Olthoff, U., Weckesser, M., Jäncke, L., Müller-Gärtner, H. W., & Dager, S. R. (1997). Regional dynamic signal changes during controlled hyperventilation assessed with blood oxygen level-dependent functional MR imaging. *American Journal of Neuroradiology*, 18(9), 1763–1770.

Purcell, E., Torrey, H., & Pound, R. (1946). Resonance Absorption by Nuclear Magnetic Moments in a Solid. *Physical Review*, 69(1-2), 37–38.

Rostrup, E., Knudsen, G. M., Law, I., Holm, S., Larsson, H. B. W., & Paulson, O. B. (2005). The relationship between cerebral blood flow and volume in humans. *NeuroImage*, 24(1), 1–11.

Rubin, G., Firlik, A. D., Levy, E. I., Pindzola, R. R., & Yonas, H. (2000). Relationship between cerebral blood flow and clinical outcome in acute stroke. *Cerebrovasc Dis*, 10(4), 298–306.

Shiino, A., Morita, Y., Tsuji, A., Maeda, K., Ito, R., Furukawa, A., & Inubushi, T. (2003). Estimation of cerebral perfusion reserve by blood oxygenation level-dependent imaging: comparison

with single-photon emission computed tomography. *Journal of Cerebral Blood Flow and Metabolism: Official Journal of the International Society of Cerebral Blood Flow and Metabolism*, 23(1), 121–135.

Smith, N., & Webb, A. (2011). *Introduction to medical imaging: Physics, engineering and clinical applications*. Cambridge University Press.

Smith, S. M. (2002). Fast robust automated brain extraction. *Human Brain Mapping*, 17(3), 143–155.

Smith, S. M., & Nichols, T. E. (2009). Threshold-free cluster enhancement: Addressing problems of smoothing, threshold dependence and localisation in cluster inference. *NeuroImage*, 44(1), 83–98.

Smith, S. M., Smith, S. M., Jenkinson, M., Jenkinson, M., Woolrich, M. W., Woolrich, M. W., & Matthews, P. M. (2004). Advances in functional and structural MR image analysis and implementation as FSL. *NeuroImage*, 23 Suppl 1, S208–19.

Sousa, I., Vilela, P., & Figueiredo, P. (2013). Reproducibility of the quantification of arterial and tissue contributions in multiple postlabeling delay arterial spin labeling. *Journal of Magnetic Resonance Imaging*, 1462, 1453–1462.

Sousa, I., Vilela, P., & Figueiredo, P. (2014). Reproducibility of hypocapnic cerebrovascular reactivity measurements using BOLD fMRI in combination with a paced deep breathing task. *NeuroImage*, 98, 31–41.

Thomason, M. E., & Glover, G. H. (2008). Controlled inspiration depth reduces variance in breath-holding-induced BOLD signal. *NeuroImage*, 39(1), 206–214.

Tofts, P. (2003). *Quantitative MRI of the Brain: Measuring Changes Caused by Disease*. *Quantitative MRI of the Brain Measuring Changes Caused by Disease*.

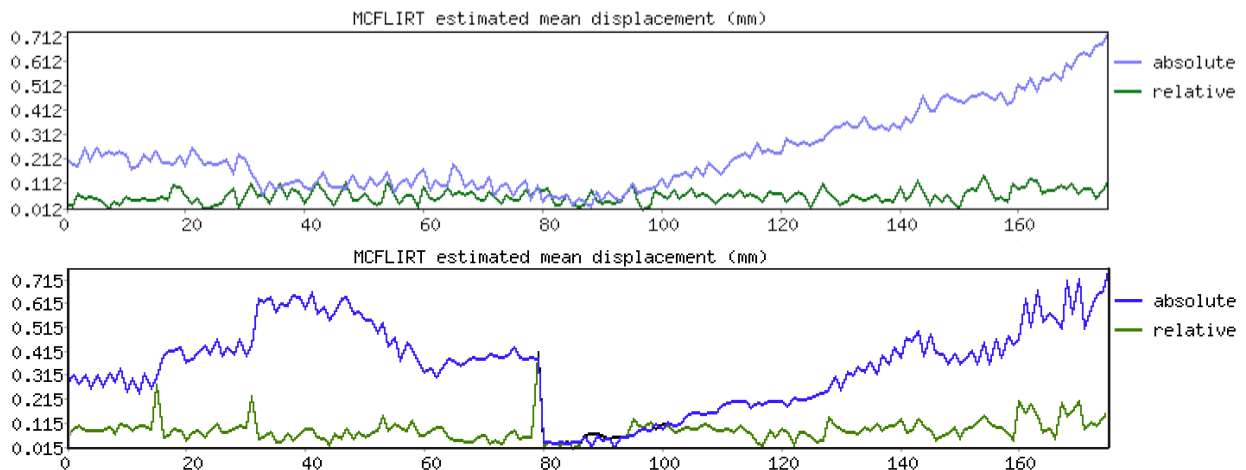
Topcuoglu, M. A. (2012). Transcranial Doppler ultrasound in neurovascular diseases: Diagnostic and therapeutic aspects. In *Journal of Neurochemistry* (Vol. 123, pp. 39–51).

Webb, A., & Kagadis, G. C. (2003). Introduction to Biomedical Imaging. *Medical Physics*.

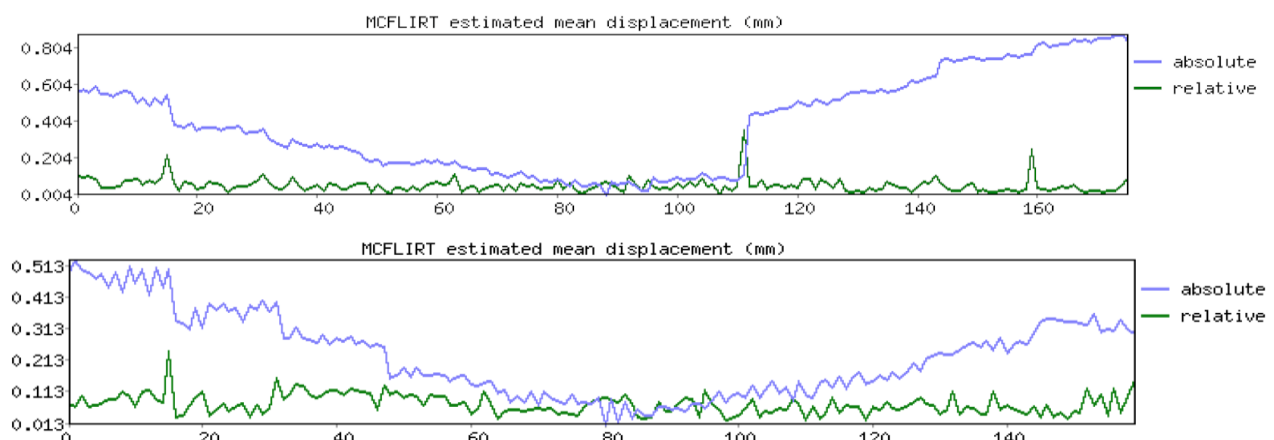
Wietasch, G. J., Mielck, F., Scholz, M., von Spiegel, T., Stephan, H., & Hoeft, A. (2000). *Bedside assessment of cerebral blood flow by double-indicator dilution technique*. *Anesthesiology* (Vol. 92).

- Williams, D. S., Detre, J. A., Leigh, J. S., & Koretsky, A. P. (1992). Magnetic resonance imaging of perfusion using spin inversion of arterial water. *Proceedings of the National Academy of Sciences of the United States of America*, 89(1), 212–216.
- Winkler, A. M., Ridgway, G. R., Webster, M. A., Smith, S. M., & Nichols, T. E. (2014). Permutation inference for the general linear model. *NeuroImage*, 92, 381–397.
- Wong, E. C., Buxton, R. B., & Frank, L. R. (1997). Implementation of quantitative perfusion imaging techniques for functional brain mapping using pulsed arterial spin labeling. *NMR in Biomedicine*, 10(4-5), 237–49.
- Wong, E. C., Buxton, R. B., & Frank, L. R. (1998). Quantitative imaging of perfusion using a single subtraction (QUIPSS and QUIPSS II). *Magnetic Resonance in Medicine*, 39(5), 702–708.
- Woolrich, M. W., Chiarelli, P., Gallichan, D., Perthen, J., & Liu, T. T. (2006). Bayesian inference of hemodynamic changes in functional arterial spin labeling data. *Magnetic Resonance in Medicine : Official Journal of the Society of Magnetic Resonance in Medicine / Society of Magnetic Resonance in Medicine*, 56(4), 891–906.
- Woolrich, M. W., Jbabdi, S., Patenaude, B., Chappell, M., Makni, S., Behrens, T., & Smith, S. M. (2009). Bayesian analysis of neuroimaging data in FSL. *NeuroImage*, 45, S173–186.
- Yonas, H., Darby, J. M., Marks, E. C., Durham, S. R., & Maxwell, C. (1991). CBF measured by Xe-CT: approach to analysis and normal values. *Journal of Cerebral Blood Flow and Metabolism : Official Journal of the International Society of Cerebral Blood Flow and Metabolism*, 11(5), 716–725.
- Zhang, Y., Brady, M., & Smith, S. (2001). Segmentation of brain MR images through a hidden Markov random field model and the expectation-maximization algorithm. *IEEE Transactions on Medical Imaging*, 20(1), 45–57.
- Zhao, P., Alsop, D. C., Abduljalil, A., Selim, M., Lipsitz, L., Novak, P., & Novak, V. (2009). Vasoreactivity and peri-infarct hyperintensities in stroke. *Neurology*, 72(7), 643–649.

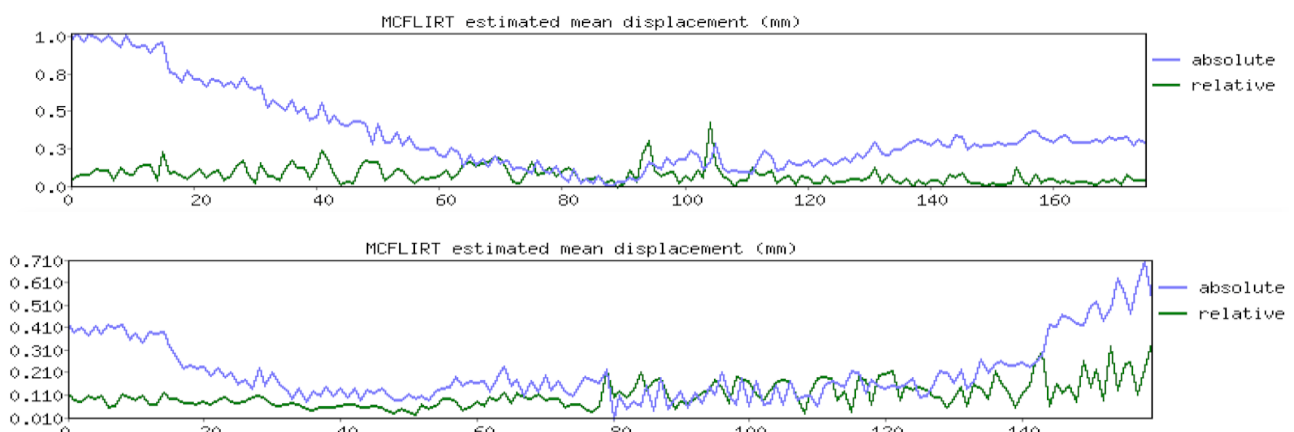
Appendices



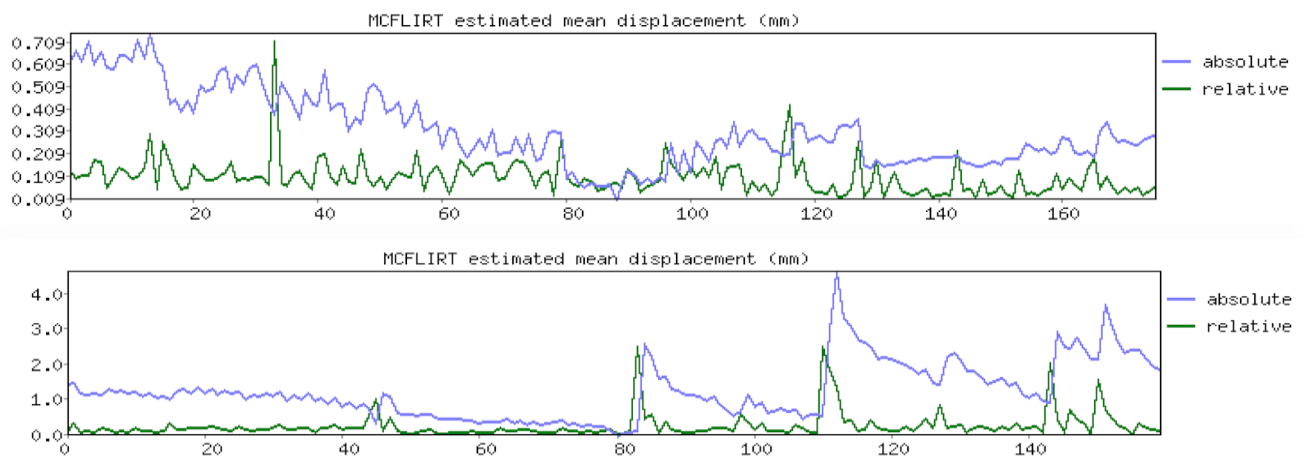
Appendix 1 – Estimated mean displacement for subject S1 with REST (top) and PDB (bottom).



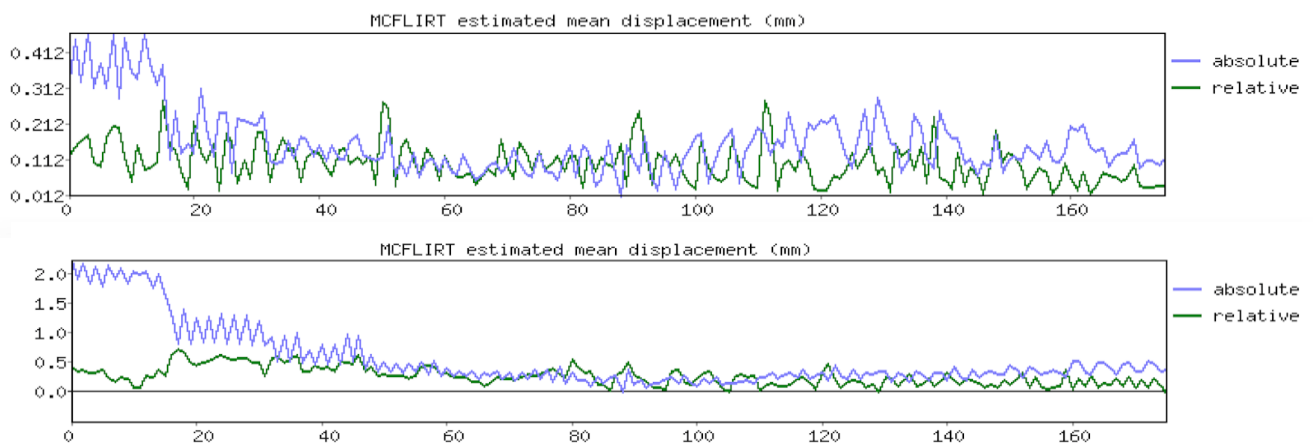
Appendix 2 – Estimated mean displacement for subject S2 with REST (top) and PDB (bottom).



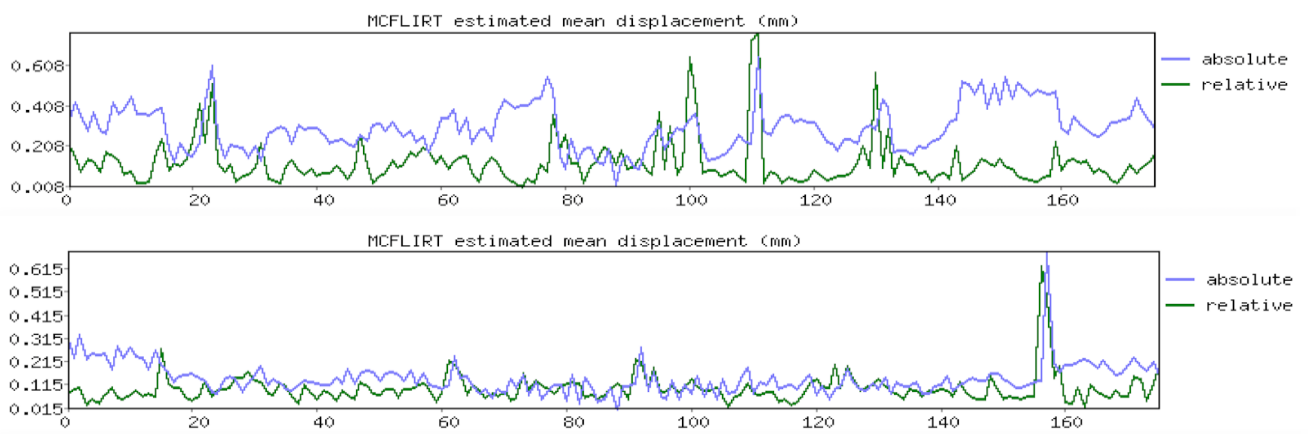
Appendix 3 – Estimated mean displacement for subject S3 with REST (top) and PDB (bottom).



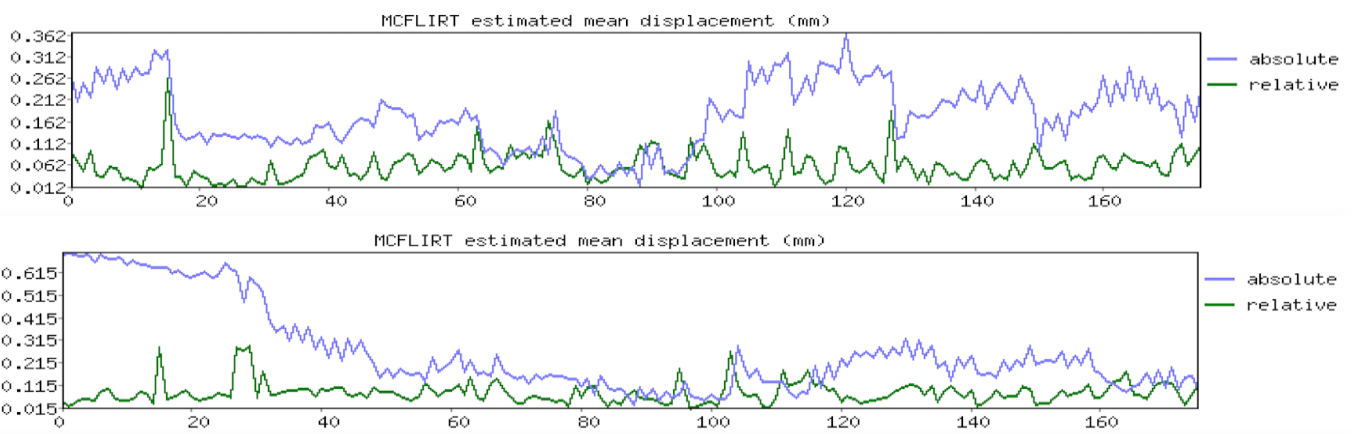
Appendix 4 – Estimated mean displacement for subject S4 with REST (top) and PDB (bottom).



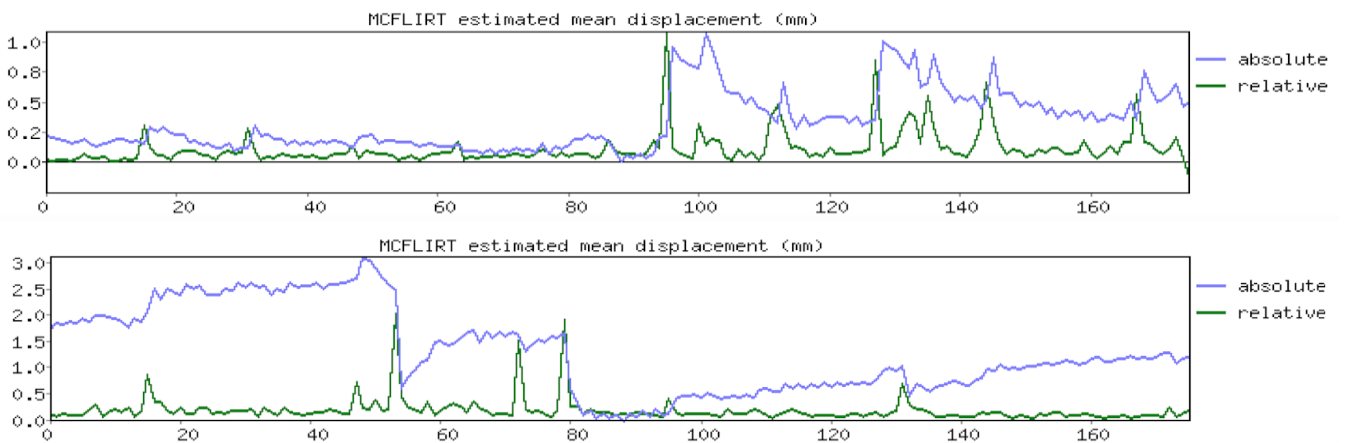
Appendix 5 – Estimated mean displacement for subject S5 with REST (top) and PDB (bottom).



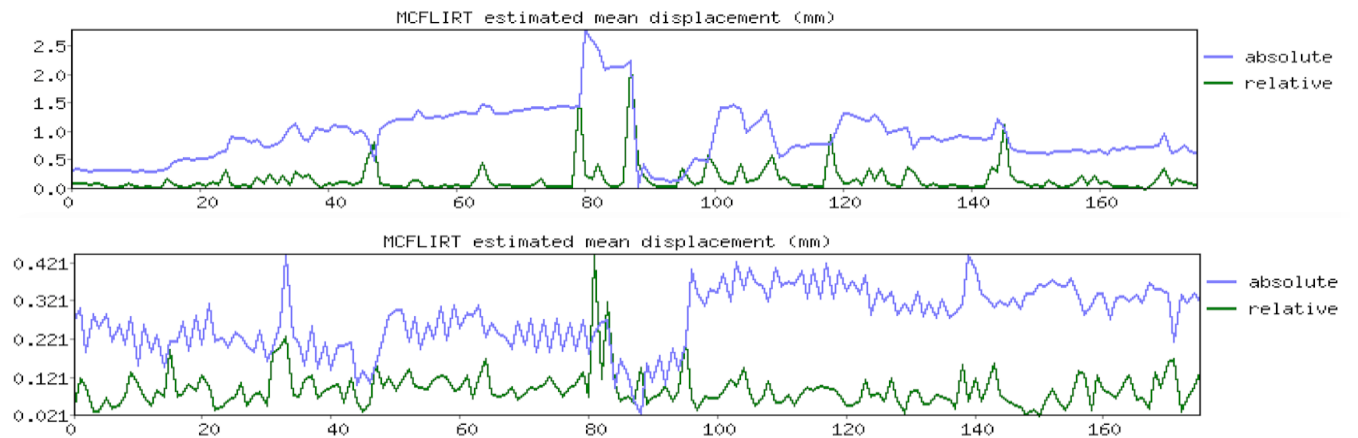
Appendix 6 – Estimated mean displacement for subject S6 with REST (top) and PDB (bottom).



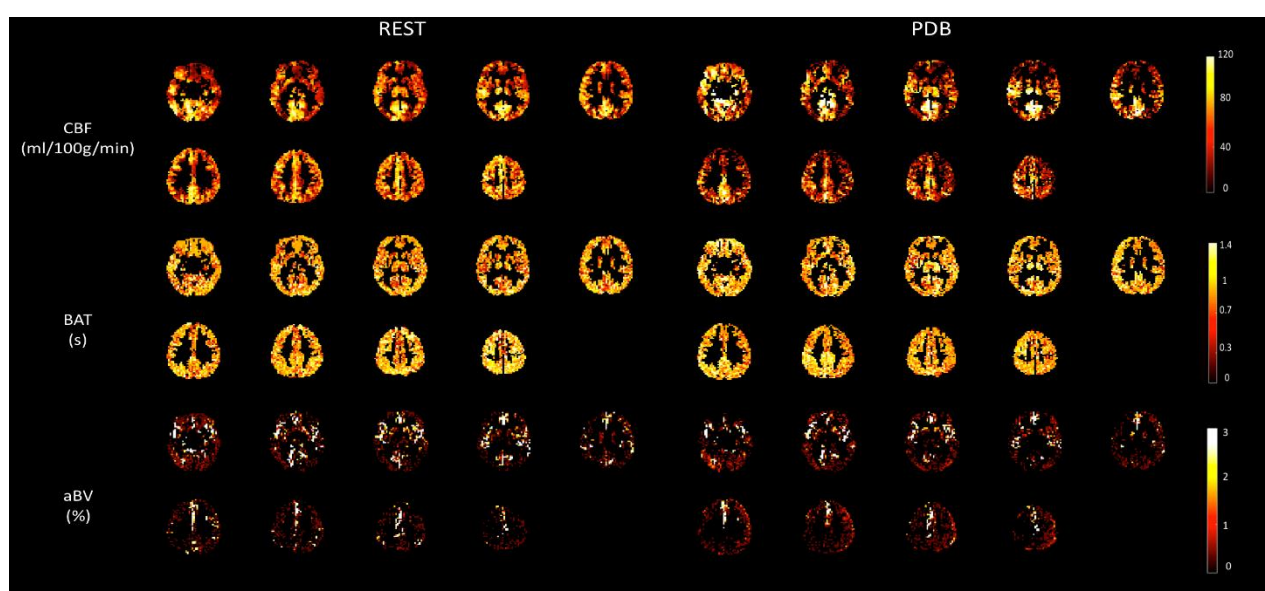
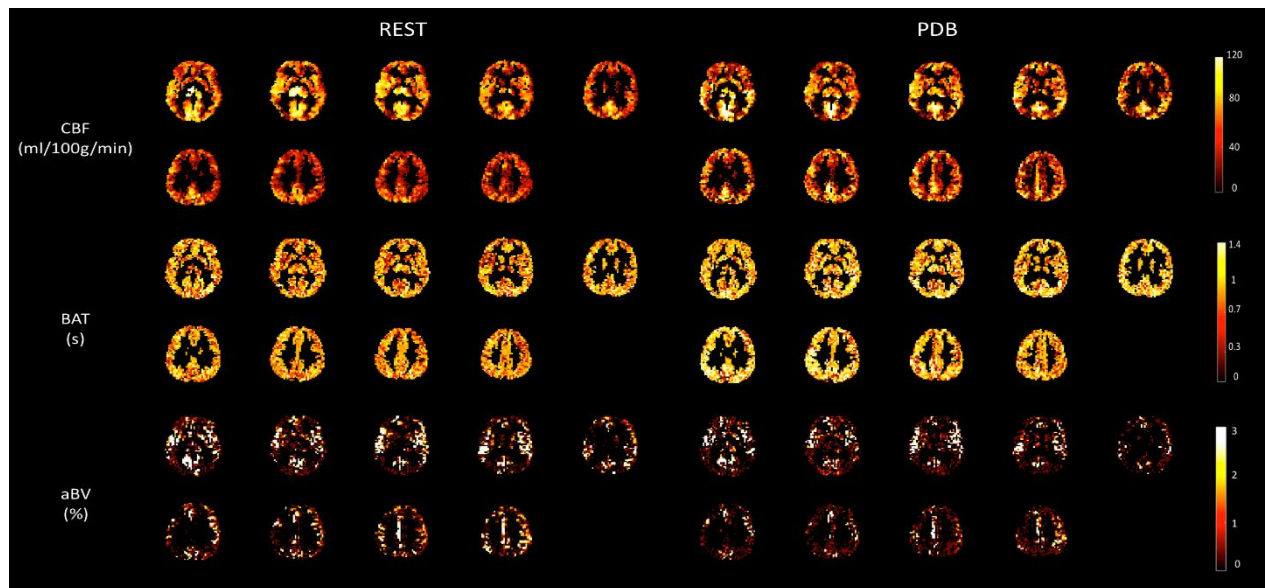
Appendix 7 – Estimated mean displacement for subject S7 with REST (top) and PDB (bottom).



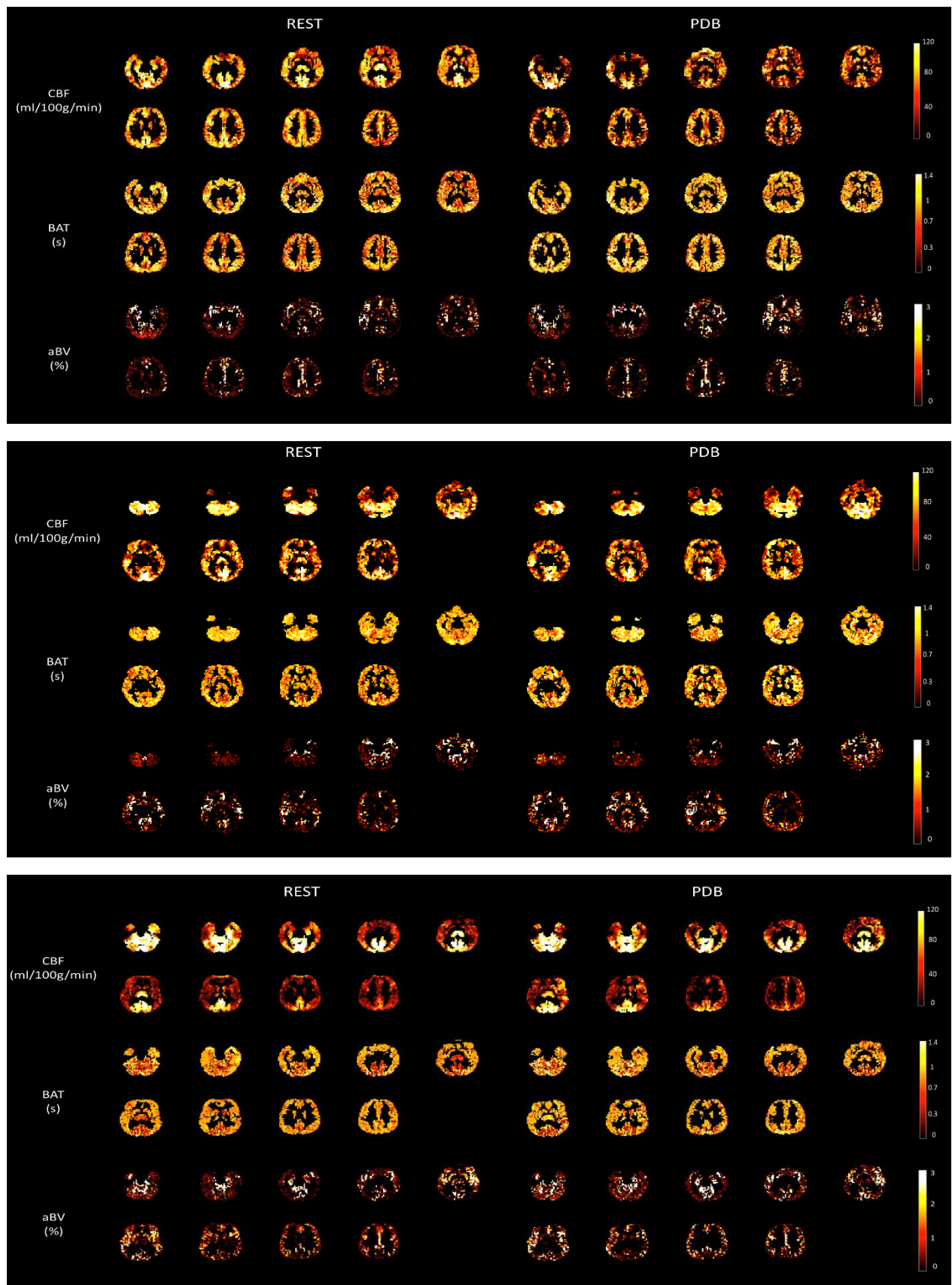
Appendix 8 – Estimated mean displacement for subject S8 with REST (top) and PDB (bottom).



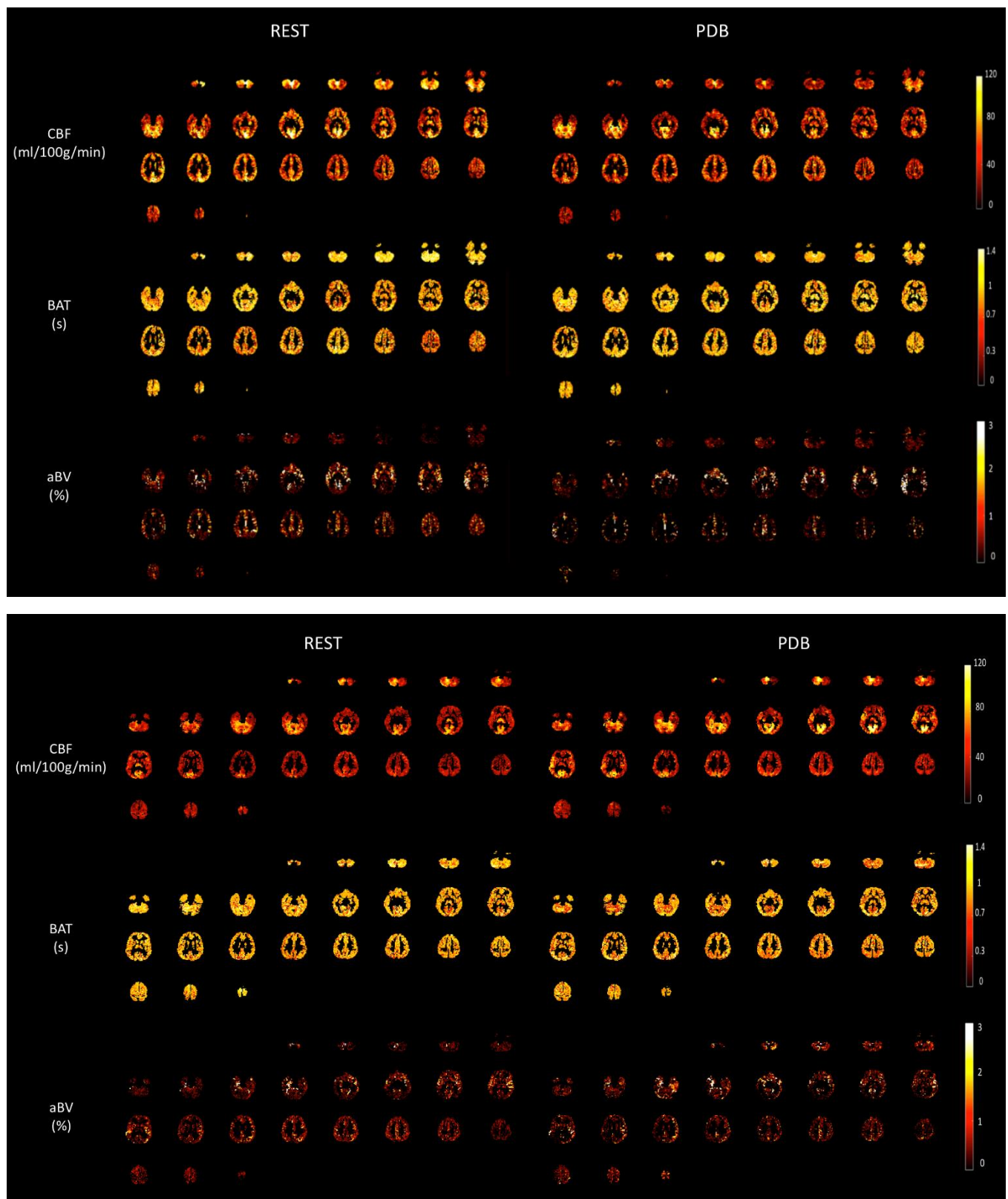
Appendix 9 – Estimated mean displacement for subject S9 with REST (top) and PDB (bottom).



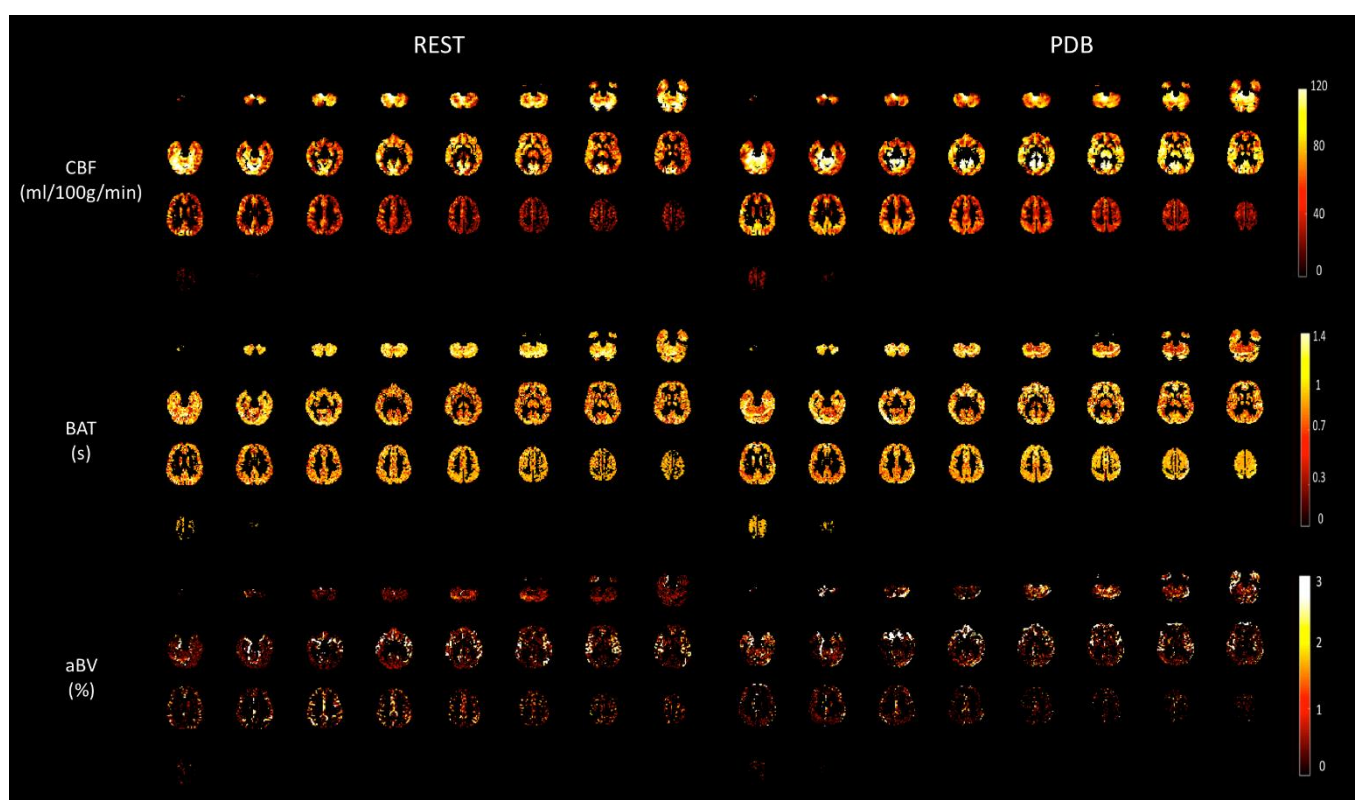
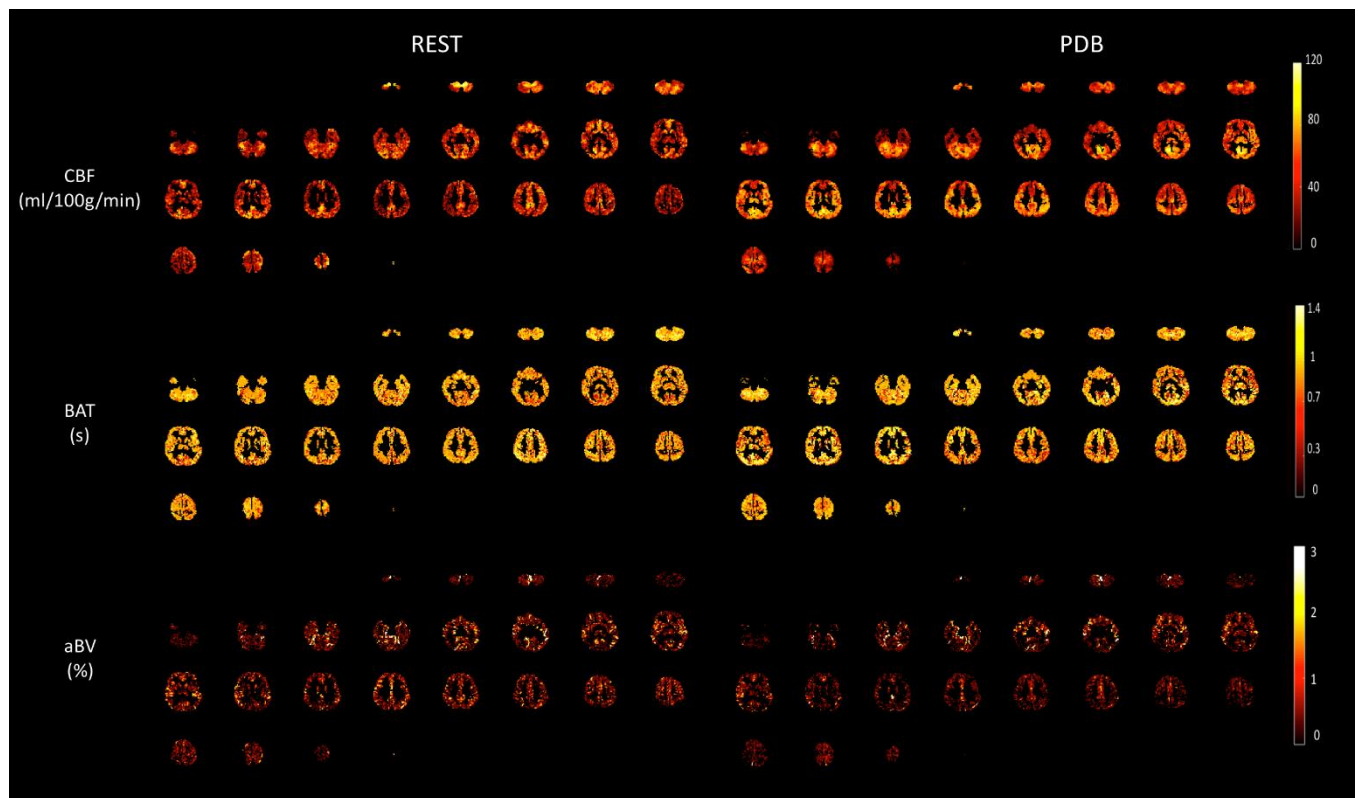
Appendix 10 – CBF, BAT and aBV maps for subjects S1 (top) and S6 (bottom), in GM ROI mask.



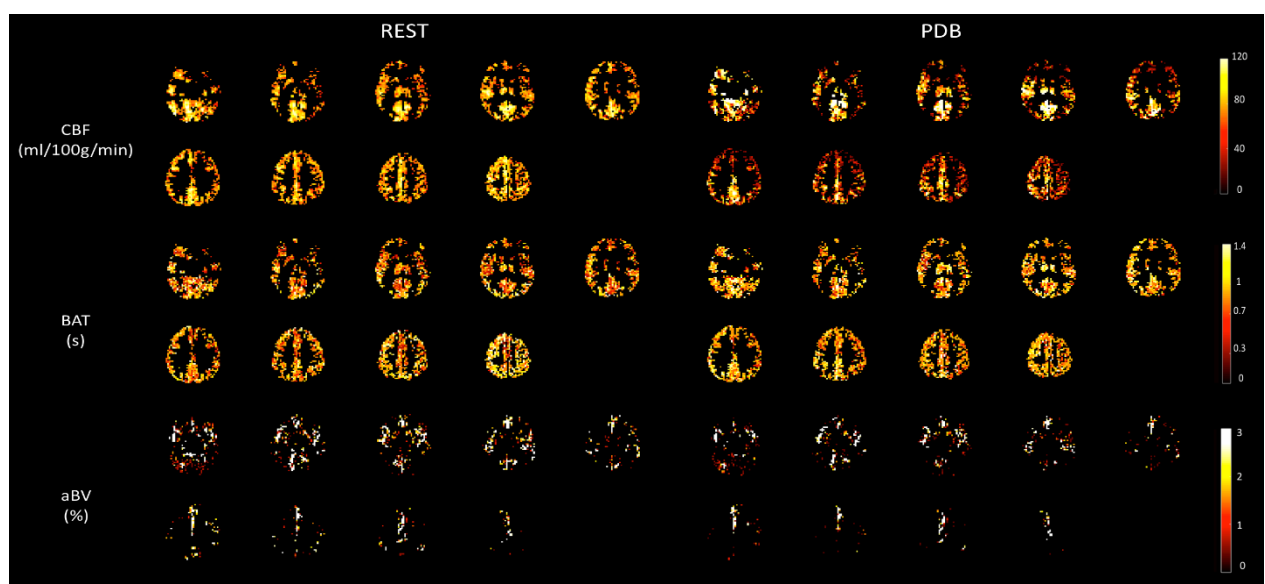
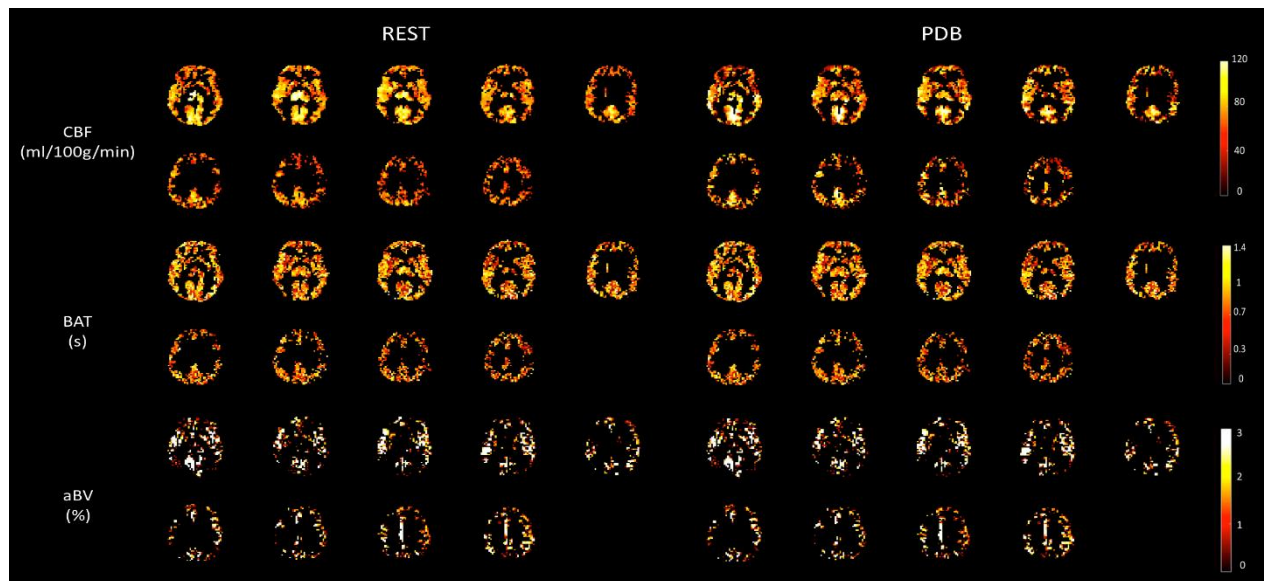
Appendix 11 – CBF, BAT and aBV maps for subjects S7 (top), S8 (middle) and S9 (bottom), in GM ROI mask.



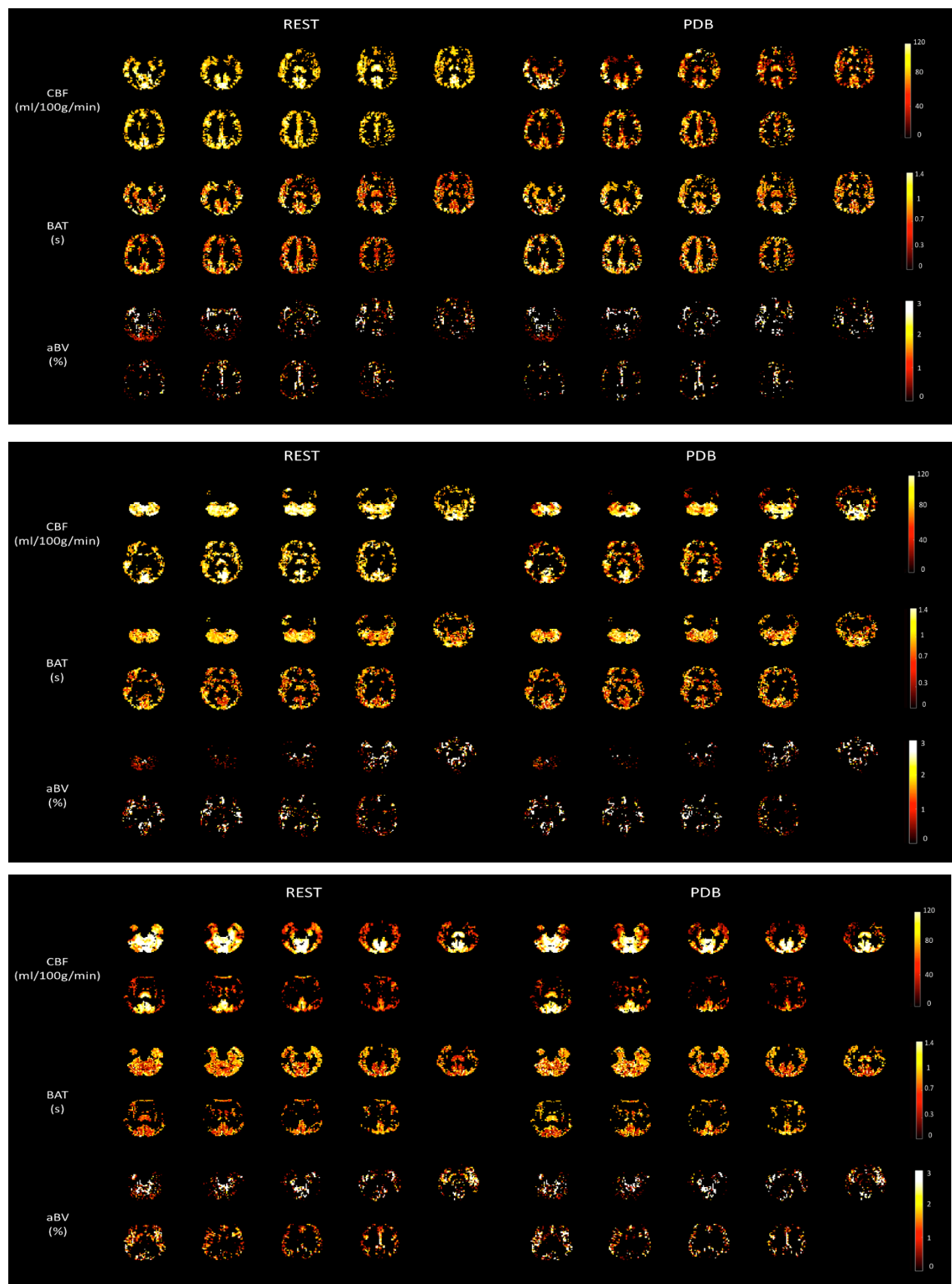
Appendix 12 – CBF, BAT and aBV maps for subjects S2 (top) and S3 (bottom), in GM ROI mask.



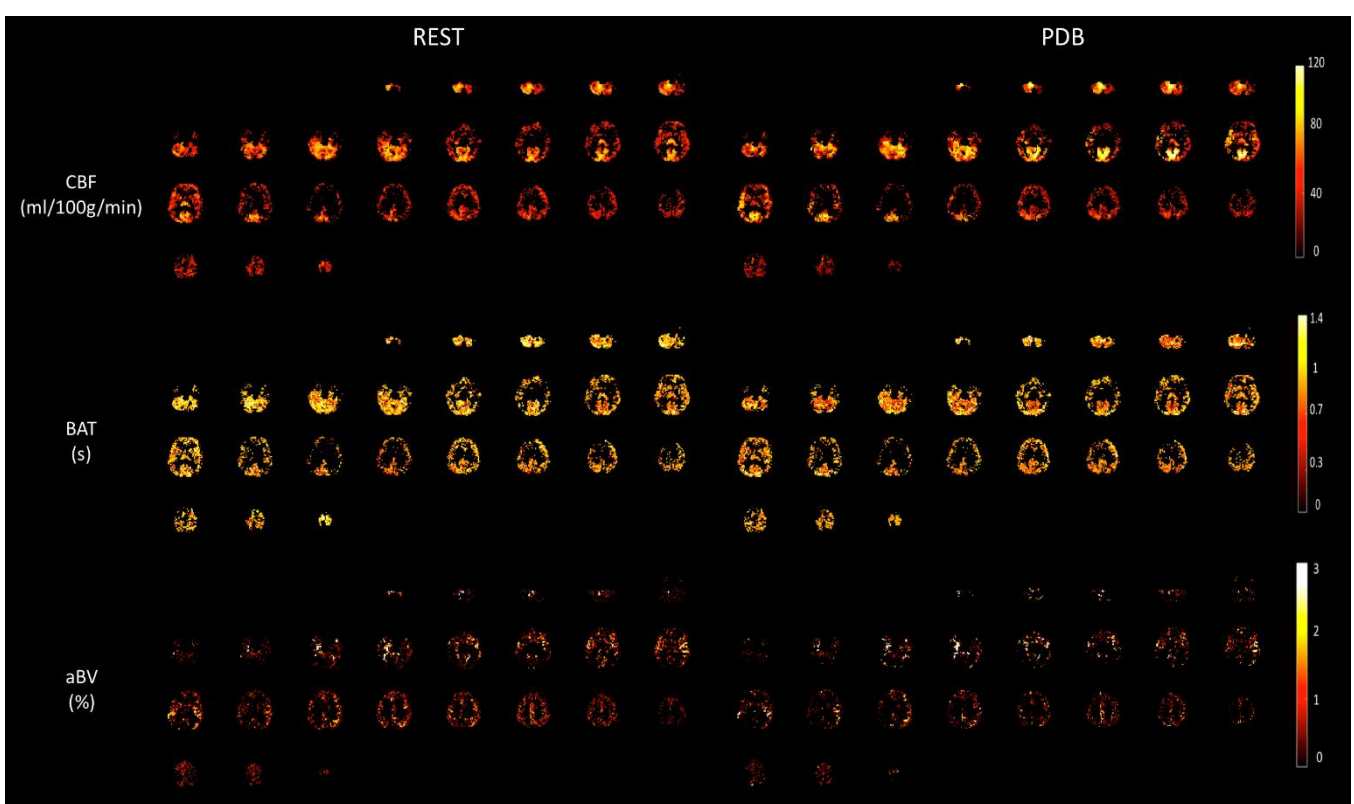
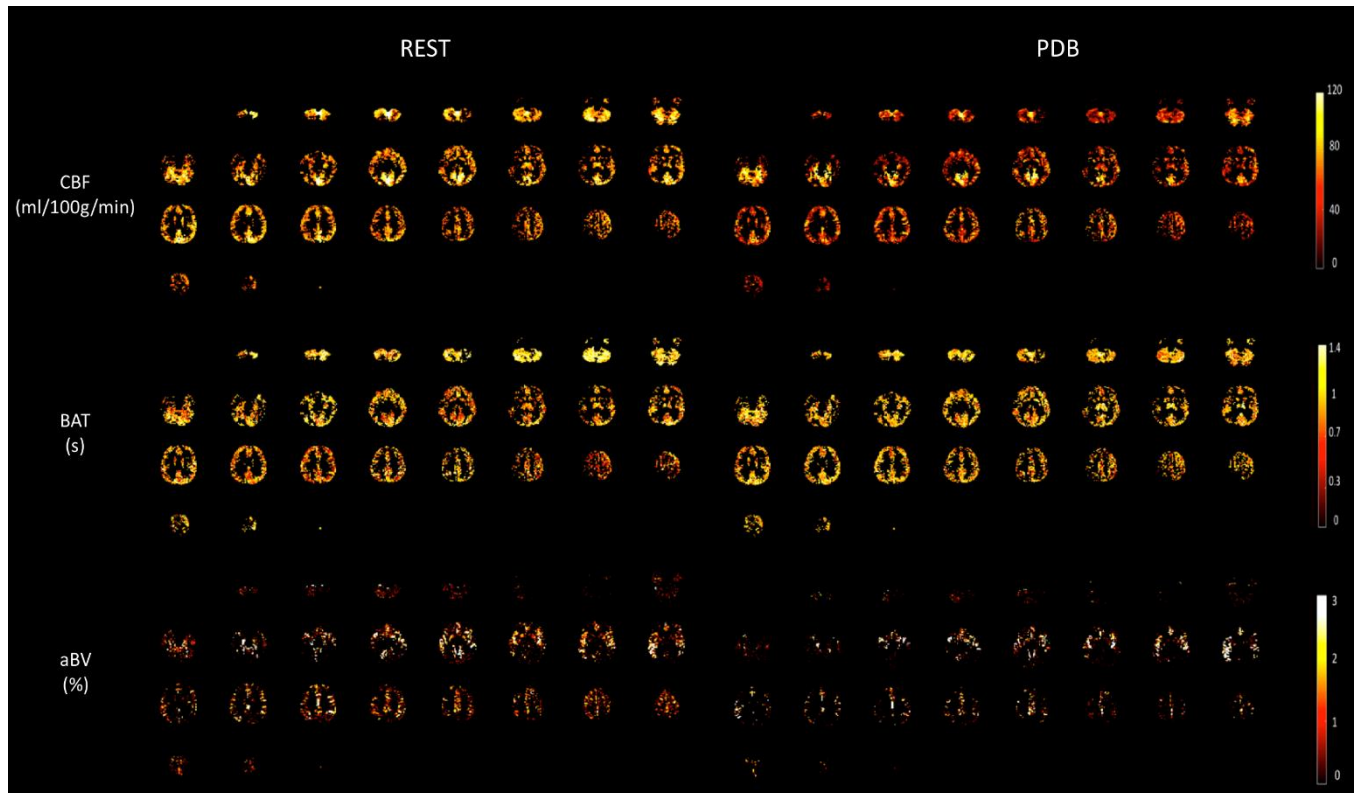
Appendix 13 – CBF, BAT and aBV maps for subjects S4 (top) and S5 (bottom), in GM ROI mask.



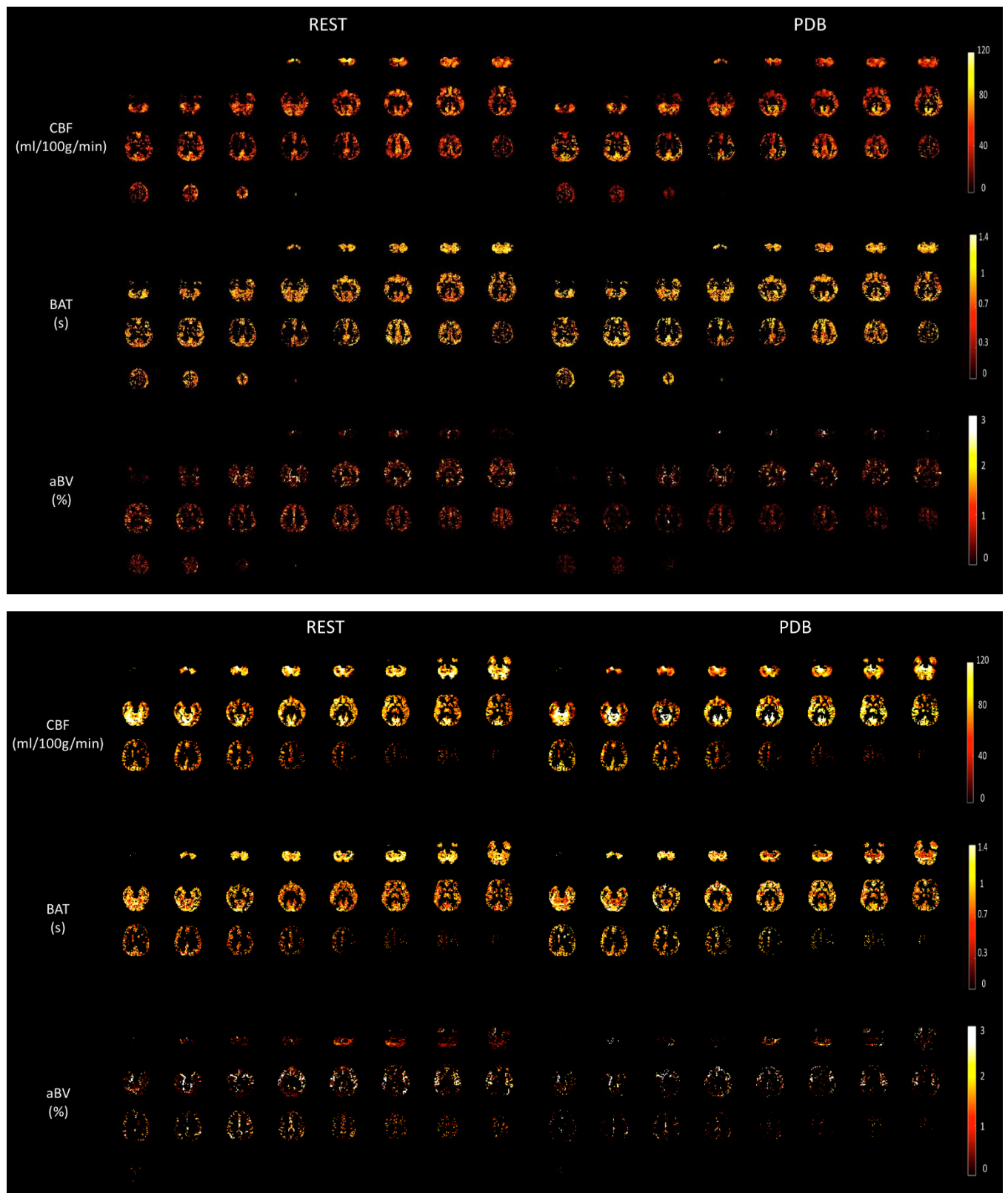
Appendix 14 – CBF, BAT and aBV maps for subjects S1 (top) and S6 (bottom), in Tissue and Vascular ROI masks.



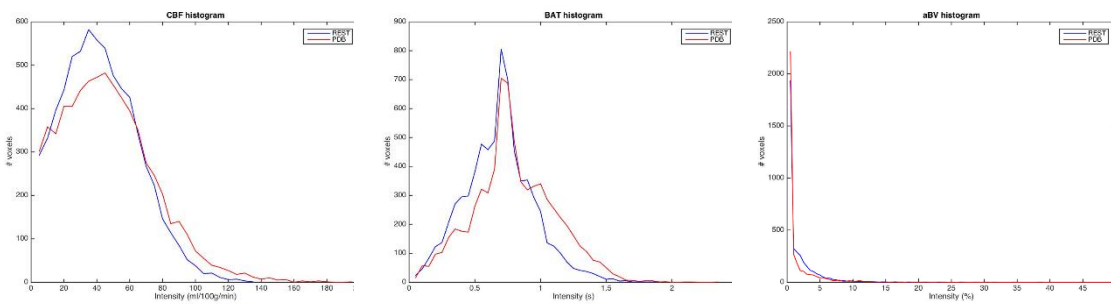
Appendix 15 – CBF, BAT and aBV maps for subjects S7 (top), S8 (middle) and S9 (bottom), in Tissue and Vascular ROI masks.



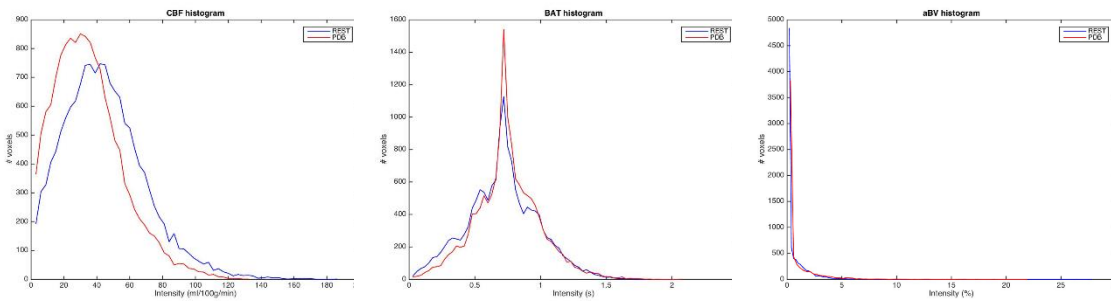
Appendix 16 – CBF, BAT and aBV maps for subjects S2 (top) and S3 (bottom), in Tissue and Vascular ROI masks.



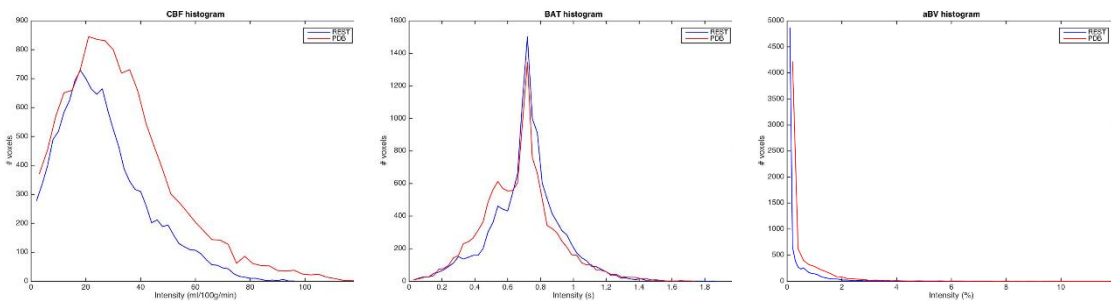
Appendix 17 – CBF, BAT and aBV maps for subjects S4 (top) and S5 (bottom), in Tissue and Vascular ROI masks.



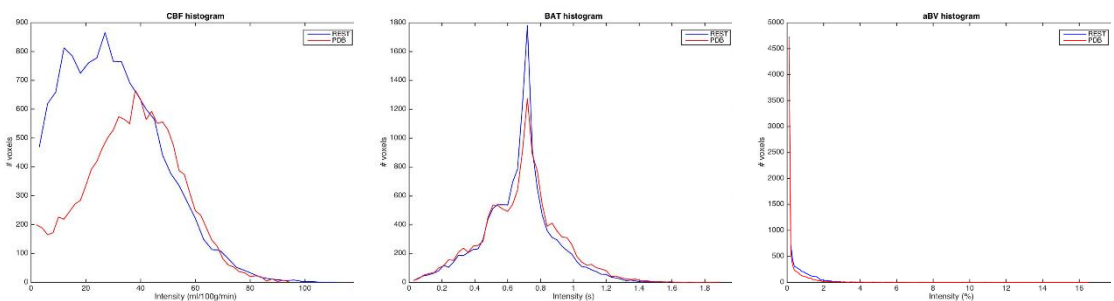
Appendix 18 – CBF, BAT and aBV histograms for subject S1 in the GM ROI mask, respectively.



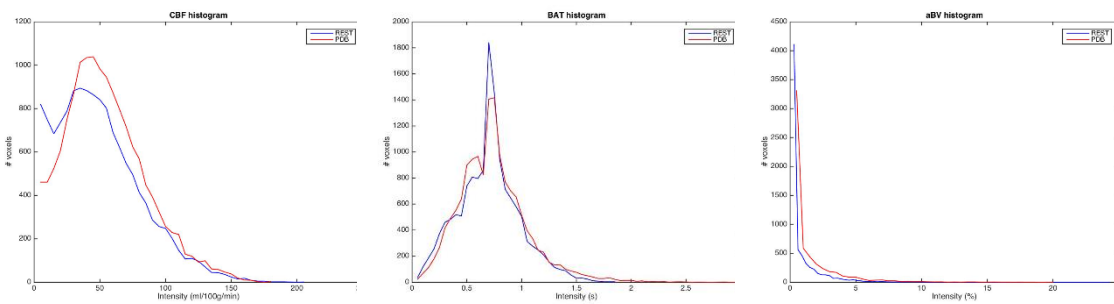
Appendix 19 – CBF, BAT and aBV histograms for subject S2 in the GM ROI mask, respectively.



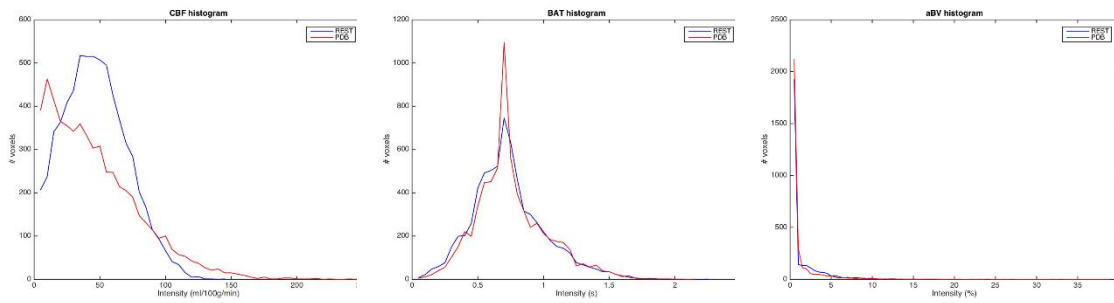
Appendix 20 – CBF, BAT and aBV histograms for subject S3 in the GM ROI mask, respectively.



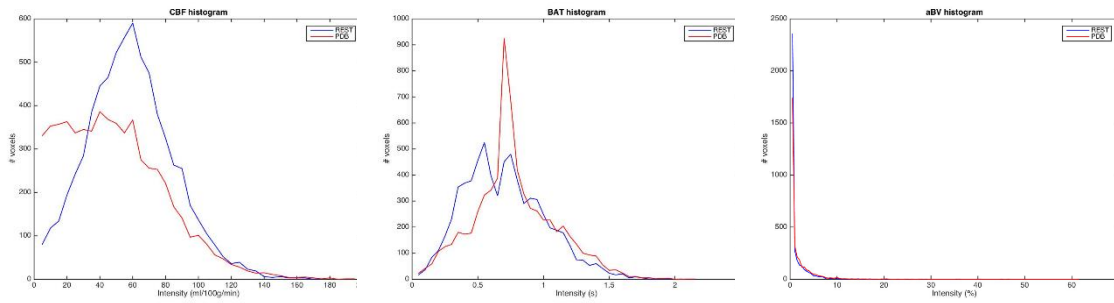
Appendix 21 – CBF, BAT and aBV histograms for subject S4 in the GM ROI mask, respectively.



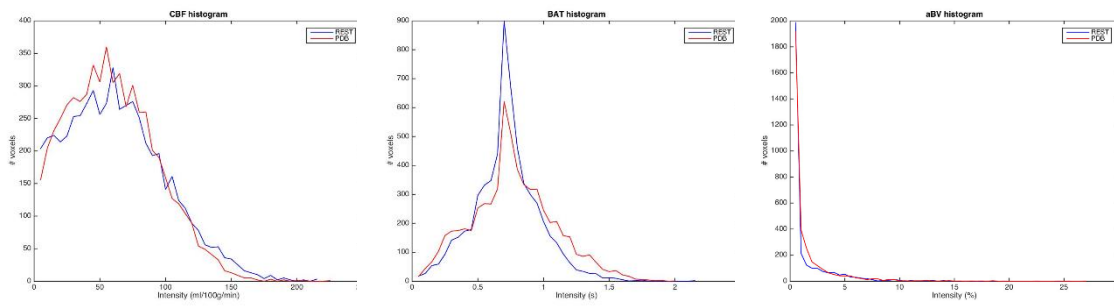
Appendix 22 – CBF, BAT and aBV histograms for subject S5 in the GM ROI mask, respectively.



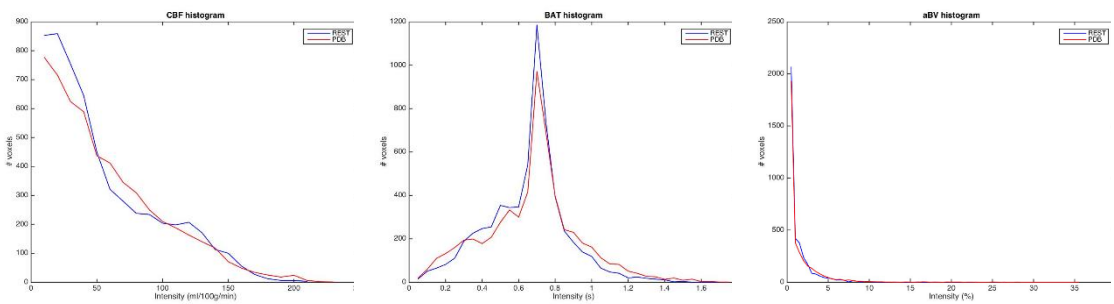
Appendix 23 – CBF, BAT and aBV histograms for subject S6 in the GM ROI mask, respectively.



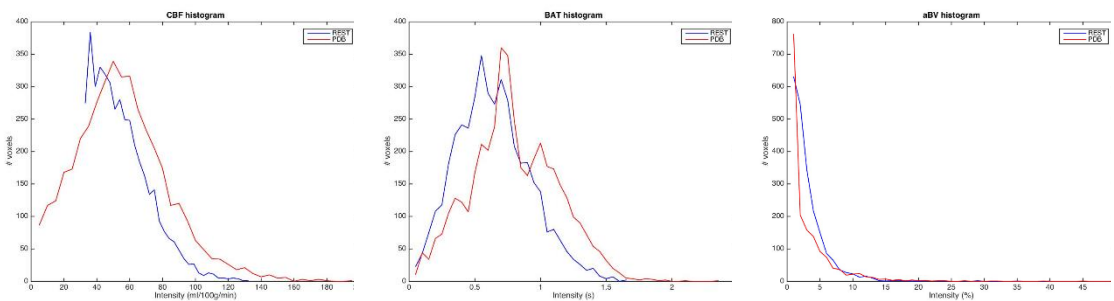
Appendix 24 – CBF, BAT and aBV histograms for subject S7 in the GM ROI mask, respectively.



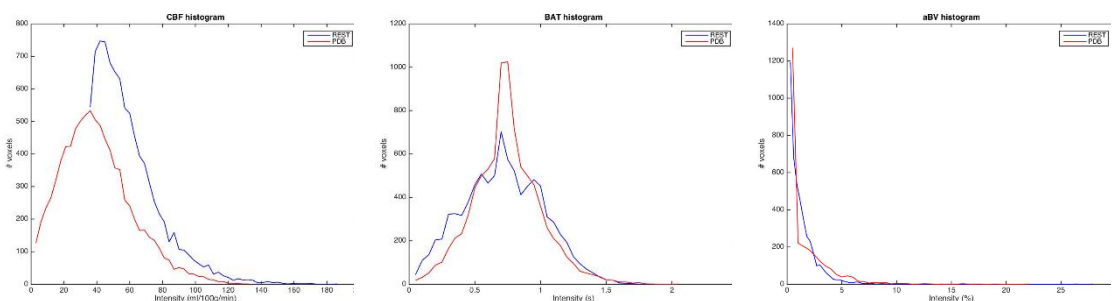
Appendix 25 – CBF, BAT and aBV histograms for subject S8 in the GM ROI mask, respectively.



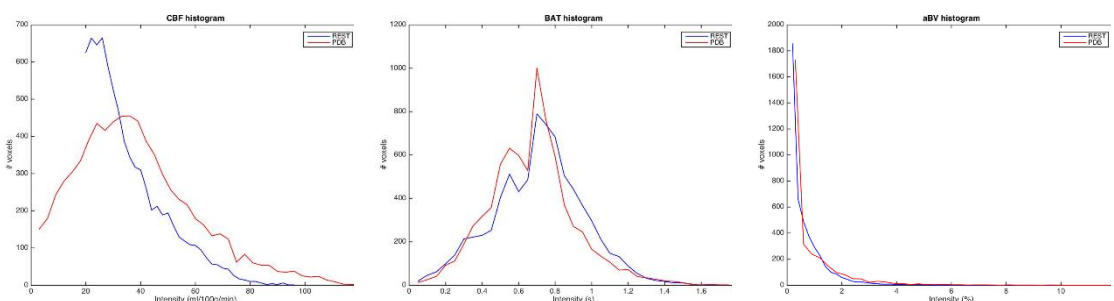
Appendix 26 – CBF, BAT and aBV histograms for subject S9 in the GM ROI mask, respectively.



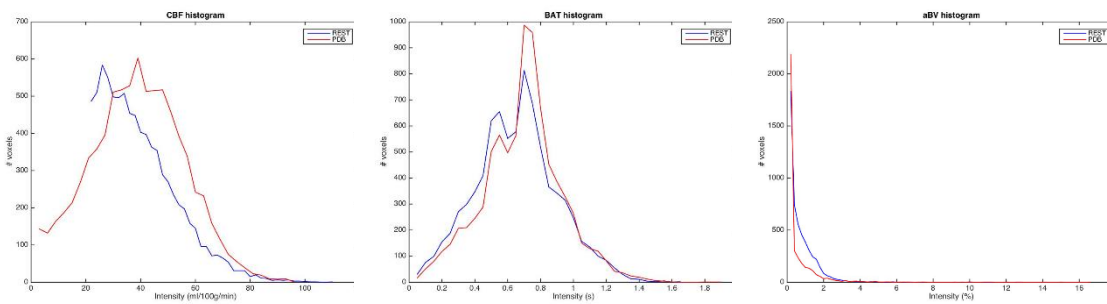
Appendix 27 – CBF, BAT and aBV histograms for subject S1 in the Tissue and Vascular ROI masks, respectively.



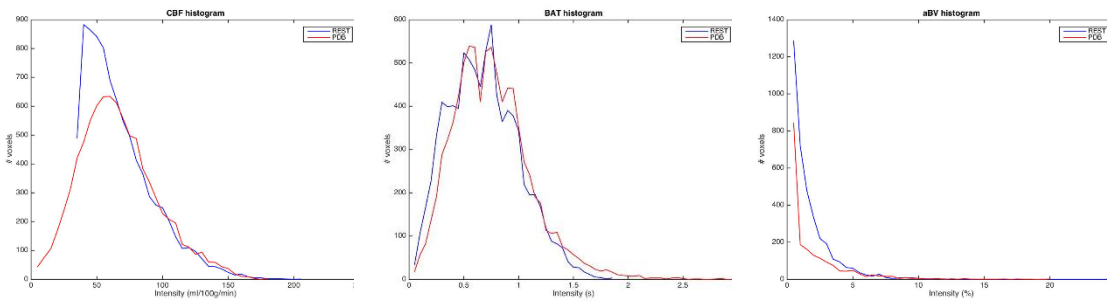
Appendix 28 – CBF, BAT and aBV histograms for subject S2 in the Tissue and Vascular ROI masks, respectively.



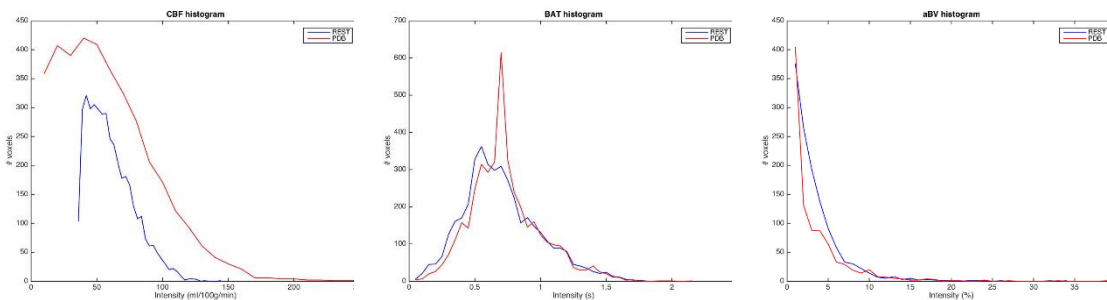
Appendix 29 – CBF, BAT and aBV histograms for subject S3 in the Tissue and Vascular ROI masks, respectively.



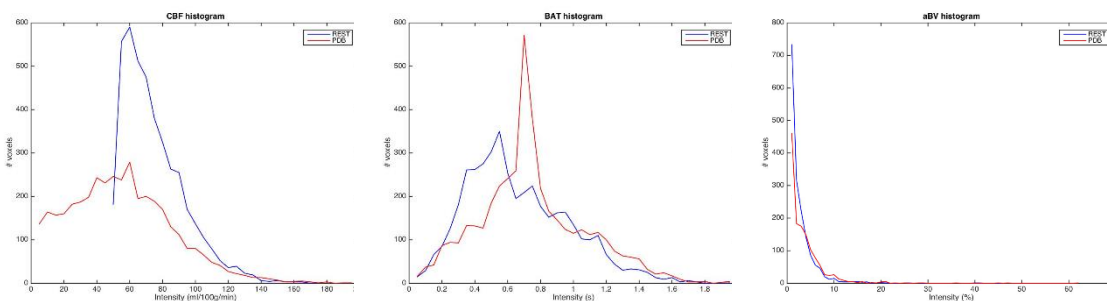
Appendix 30 – CBF, BAT and aBV histograms for subject S4 in the Tissue and Vascular ROI masks, respectively.



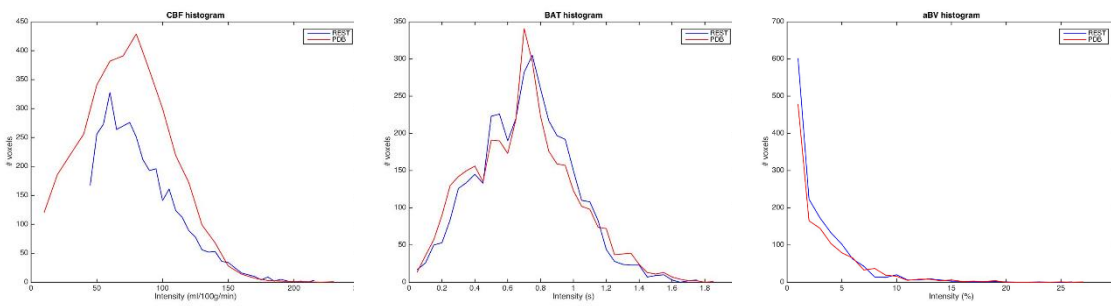
Appendix 31 – CBF, BAT and aBV histograms for subject S5 in the Tissue and Vascular ROI masks, respectively.



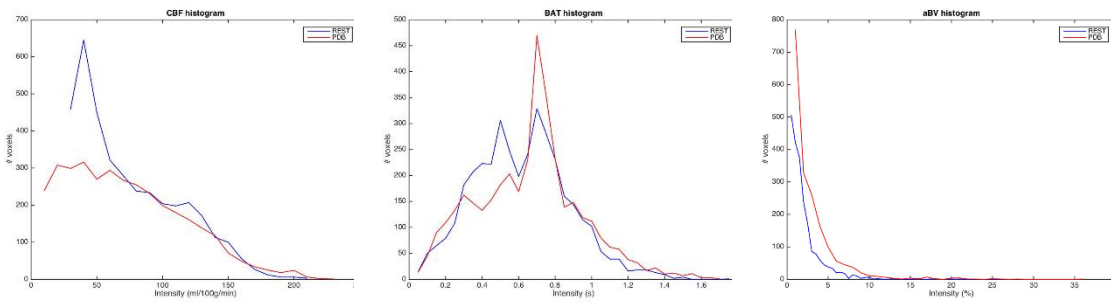
Appendix 32 – CBF, BAT and aBV histograms for subject S6 in the Tissue and Vascular ROI masks, respectively.



Appendix 33 – CBF, BAT and aBV histograms for subject S7 in the Tissue and Vascular ROI masks, respectively.



Appendix 34 – CBF, BAT and aBV histograms for subject S8 in the Tissue and Vascular ROI masks, respectively.



Appendix 35 – CBF, BAT and aBV histograms for subject S9 in the Tissue and Vascular ROI masks, respectively.